



1 **A Dissertation Submitted to**
2 **Shanghai Jiao Tong University for the degree of**
3 **Doctor of Philosophy in Physics**

4
5
6 Search for new phenomena in dijet events with
7 quark/gluon tagger using the ATLAS detector

8
9
10
11
12 Wanyun Su

13
14
15
16
17 Tsung-Dao Lee Institute
18 Shanghai Jiao Tong University
19 Shanghai, P.R.China
20 September 4, 2023

21

22



23

申请上海交通大学博士学位论文

24

25

26

在 ATLAS 双喷注末态中利用 夸克/胶子标定寻找新粒子

27

28

29

30

作者：苏琬云

31

导师：李数、Shih-Chieh Hsu (University of Washington,
Seattle)

32

33

李政道研究所
上海交通大学

34

35

36

37

2023 年 9 月 4 日

38

39

上海交通大学 学位论文原创性声明

40 本人郑重声明：所呈交的学位论文，是本人在导师的指导下，独立进行研究
41 工作所取得的成果。除文中已经注明引用的内容外，本论文不包含任何其他个人
42 或集体已经发表或撰写过的作品成果。对本文的研究做出重要贡献的个人和集体，
43 均已在文中以明确方式标明。本人完全知晓本声明的法律后果由本人承担。

44 学位论文作者签名：
日期： 年 月 日

45
46

47

48

上海交通大学 学位论文使用授权书

49 本人同意学校保留并向国家有关部门或机构送交论文的复印件和电子版，允
50 许论文被查阅和借阅。

51 本学位论文属于：

- 52 公开论文
53 内部论文，保密 1年 / 2年 / 3年，过保密期后适用本授权书。
54 秘密论文，保密 ____ 年（不超过 10 年），过保密期后适用本授权书。
55 机密论文，保密 ____ 年（不超过 20 年），过保密期后适用本授权书。
56 （请在以上方框内选择打“√”）

57

58 学位论文作者签名： 指导教师签名：
日期： 年 月 日 日期： 年 月 日

摘要

这篇论文中所呈现的物理分析旨在寻找标准模型之外的新物理现象，使用积分亮度为 140 fb^{-1} ，中心质心能量为 13 TeV ，由 ATLAS 探测器记录的质子-质子碰撞数据。该分析在三个不同的谱中寻找超越标准模型的新共振体证据：未标记双喷注不变质量、一个胶子标记和两个胶子标记信道。为了增加观察新共振体的灵敏度，该分析采用了一种基于关联粒子轨迹数量的胶子标记方法，以优先地寻找一个或多个胶子衰变的共振体迹象。由于来自夸克和胶子的喷注可以使用夸克/胶子标记器进行识别，因此本研究调查了两种标记器：一种基于与喷注关联的带电轨迹数目，而另一种则采用增强决策树来结合各种喷注次级结构可观测量，同时提供了标记效率的数据与蒙特卡洛模拟之间的差异。在数据上执行矩阵方法，从夸克/胶子丰富子样本中获取夸克/胶子分数，该样本由喷注的赝快度定义。在分析中，利用了将量子色动力学背景估计为参数化双喷注质量谱的统计框架。然后在 95% 的置信水平上，针对多种超越标准模型物理理论以及一个独立于模型的通用高斯形状信号，设置了上限。

73

74 **关键词：**标准模型，ATLAS 探测器，喷注标定

ABSTRACT

75

ABSTRACT

76

77 The physics analyses presented in this PhD dissertation search for new physics be-
78 yond the Standard Model (BSM) in the dijet mass distribution using an integrated lumi-
79 nosity of 140 fb^{-1} of proton-proton collisions with a centre-of-mass energy at 13 TeV
80 recorded by the ATLAS detector. This analysis aims at searching for the evidence of the
81 BSM resonances that decay into two jets. Jets originating from quarks and gluons can be
82 identified using quark/gluon tagger. Two taggers are investigated: one tagger based on
83 the number of charged tracks associated with the jets, while the other employs a boosted
84 decision tree to combine various jet substructure observables. Differences between data
85 and Monte Carlo simulation of tagging efficiency are provided. A matrix method is
86 performed on data to retrieve the quark/gluon fraction from quark/gluon-enriched sub-
87 samples, defined by the pseudorapidity of the jet. In the analysis, the quantum chromo-
88 dynamics (QCD) background is estimated by the statistical framework which parame-
89 terised the dijet mass spectrum. Upper limits then are set at the 95% confidence level on
90 a variety of theories of BSM physics and a model-independent generic Gaussian shape
91 signal.

92

93 **KEY WORDS:** Standard Model, ATLAS, calibration, jet tagging

94 **Contents**

95	1 Introduction	1
96	2 The theory framework	3
97	2.1 The Standard Model	3
98	2.1.1 Quantum chromodynamics	5
99	2.2 Physics beyond the Standard Model	7
100	2.2.1 String	7
101	2.2.2 Kaluza-Klein Graviton	8
102	2.2.3 Quantum Black Hole	9
103	3 The ATLAS Experiment	10
104	3.1 The Large Hadron Collider	10
105	3.2 The ATLAS detector	12
106	3.2.1 Inner detector	12
107	3.2.2 Calorimeters	15
108	3.2.3 Muon spectrometer	19
109	3.2.4 Trigger and data acquisition	19
110	4 Jets in ATLAS	22
111	4.1 Jet reconstruction	22
112	4.2 Jet calibration and cleaning	25
113	4.2.1 Pile-up corrections	25
114	4.2.2 Jet energy scale and η calibration	26
115	4.2.3 Global sequential calibration	27
116	4.2.4 Residual <i>in situ</i> calibration	28
117	5 The calibration of quark/gluon jets taggers	29
118	5.1 Data and Monte Carlo samples	29
119	5.1.1 Data	29
120	5.1.2 Monte Carlo simulation	30
121	5.2 Object and Event selection	31
122	5.2.1 Physics object definition	32
123	5.2.2 Event Selection and definition of quark and gluon-enriched samples	33
124	5.3 Quark/gluon tagging variables	33

Contents

125	5.3.1	The BDT tagger	35
126	5.3.1.1	Feature selections	36
127	5.3.1.2	Training weights	37
128	5.3.1.3	Training Configuration	40
129	5.4	Matrix Method	43
130	5.5	MC non-closure	48
131	5.5.1	Closure test for BDT tagger	51
132	5.5.2	Summary for the MC Closure test	54
133	5.6	Scale factor	54
134	5.7	Systematic uncertainties	62
135	5.7.1	Parton shower modelling uncertainty	62
136	5.7.2	Hadronisation modelling uncertainty	63
137	5.7.3	Matrix element uncertainty	64
138	5.7.4	PDF uncertainty	64
139	5.7.5	Scale variation uncertainty	64
140	5.7.6	Splitting-Kernel variation uncertainty	65
141	5.7.7	Tracking uncertainty	65
142	5.7.8	JES /JER uncertainty	66
143	5.7.9	N_{trk} / BDT re-weighting	66
144	5.7.10	The MC non-closure	70
145	5.7.11	Statistical uncertainty	70
146	5.8	Results	71
147	6	Search for new phenomena in dijet events	89
148	6.1	Monte Carlo models	90
149	6.1.1	QCD background	90
150	6.1.2	String	90
151	6.1.3	Kaluza-Klein Graviton	93
152	6.1.4	Quantum Black Hole	94
153	6.1.5	Gaussian resonances	94
154	6.2	Events selections	96
155	6.2.1	Observables and Kinematic Variables	96
156	6.2.2	Baseline selection	97
157	6.3	Quark-Gluon Sample Selection	98

Contents

158	6.3.1 Selection Criteria	99
159	6.4 Signal Optimisation	105
160	6.4.1 y^* Cut Optimisation	105
161	6.4.2 Dijet Mass Turn-on	109
162	6.4.3 Optimised Selection	112
163	6.4.4 Selected Kinematic Plots	113
164	6.5 Statistical Framework	115
165	6.5.1 Fitting Framework	115
166	6.5.2 Statistical Method	116
167	6.5.2.1 Parametric background models	116
168	6.5.2.2 Uncertainties	117
169	6.5.2.3 Likelihood function definition	117
170	6.5.2.4 Statistical Method	118
171	6.5.2.5 Test statistic and p-value definitions	119
172	6.5.2.6 Generation of pseudo-data	120
173	6.5.2.7 Definition of exclusion limit	120
174	6.5.2.8 Implementation	121
175	6.5.3 Background Estimation	121
176	6.5.4 Analysis Strategy	121
177	6.5.5 Spurious Signal Tests	122
178	6.5.6 Fit Stability Tests	126
179	6.6 Systematic uncertainties	128
180	6.6.1 String resonance systematic uncertainties	128
181	6.6.2 q/g tagging Systematics	130
182	6.6.2.1 Pure MC Systematics	130
183	6.7 Results	132
184	7 Conclusions	136
185	8 Acknowledgements	150

186

1 Introduction

187 Over the past seventy years, the theories and discoveries of thousands of physi-
188 cists have developed a notable insight into the fundamental structure of matters, called
189 fundamental particles, which are governed by four fundamental forces. One of the best
190 understandings of how these particles and three of the forces interact with each other
191 is encapsulated in the Standard Model (SM) [1, 2] of particle physics. Developed in the
192 early 1970s, it has been successfully proved by almost all experimental results. The huge
193 success of the discovery of Higgs Boson in 2012 predicted by the SM was awarded the
194 Nobel Prize in Physics in 2013. The SM has become established as a well-tested physics
195 theory.

196 Although the SM accurately describes the phenomena within its domain, there are
197 still theoretical flaws that prevent some fundamental physical phenomena from being
198 fully explained by the SM. First of all, the model contains many parameters that cannot
199 be derived from calculations alone but must be determined by experiment. In 1998, the
200 Japanese Super Kamioka neutrino detector published results on neutrino oscillations that
201 suggested the neutrinos have a non-zero rest mass, which did not match the prediction
202 made by the SM. Besides, the existence of gravity and dark matter has not yet been
203 described by the SM theory.

204 Many models of physics beyond the Standard Model (BSM) [3] predict the presence
205 of new particles that couple to quarks and/or gluons. Such particles could be produced
206 in proton-proton collisions at the Large Hadron Collider (LHC) [4] and then decay into
207 quarks and gluons, during this process two hadronic jets are created, which then can be
208 seen by the detector. The new energy regime ($\sqrt{s} = 13$ TeV) with an integrated luminosity
209 of 140 fb^{-1} provided by the LHC opens a window to search for BSM particles.

210 In the SM, these dijet events are generated mainly by quantum chromodynamic
211 (QCD) processes and appeared to be a smoothly decreasing invariant mass (m_{jj}) dis-
212 tribution, however, a new particle that decays into quarks or gluons could appear as a
213 resonance in the m_{jj} spectrum. If the resonant samples can be classified based on the
214 type of parton that initiated the jets, the sensitivity of the search for such resonances
215 could be largely increased. Hence, classifying jets as initiated from a quark or a gluon
216 can be effective for improving SM measurements and searches for BSM physics.

217 Recent developments [5, 6, 7, 8, 9, 10, 11, 12, 13, 14, 15, 16, 17, 18, 19, 20, 21]

Introduction

in quark/gluon (q/g) tagging have resulted from advances in the theoretical [22], phenomenological [23, 24, 25, 26] and experimental understanding of q/g tagging as well as the development of powerful machine learning techniques that can utilize the entire jet internal radiation pattern. The calibration of q/g taggers is performed to account for the systematics of searching results.

This thesis is structured as follows. Chapter 2. describes the theoretical framework of the SM, its limitations and various potential extensions beyond it. An introduction to the LHC and the ATLAS detector is given in Chapter 3. Jet reconstructions and calibrations are briefly described in Chapter 4. The quark/gluon tagger definitions and the selection criteria used to generate the various event samples employed in the discriminant extraction, the method and the scale factor results are presented in Chapter 5. The details of the search for new resonances in the dijet spectrum and the limit setting results are shown in Chapter 6. In the end, the conclusion and outlook of the research are presented in Chapter 7.

232

2 The theory framework

233 2.1 The Standard Model

234 The SM of particle physics, which describes the three fundamental interactions -
 235 strong, weak and electromagnetic interactions, alongside the elemental constituents that
 236 constitute all forms of matter, stands as the most triumphant theory within the realm of
 237 particle physics. The SM divides particles into two categories, fermions and bosons,
 238 based on the values of their spin: fermions are the particles that makeup matter, such as
 239 electrons in leptons, quarks and neutrinos, which have half-integer spin; bosons are the
 240 particles that transmit forces, such as photons and mesons that transmit electromagnetic
 241 forces, gluons that transmit strong nuclear forces, W and Z that transmit weak nuclear
 242 forces, have integer spin. Different properties shown in fermions and bosons are due to
 243 the difference in spin. According to the spin-statistics theorem, fermions obey the Pauli
 244 exclusion principle, whereas bosons do not, thus bosons do not have a theoretical limit
 245 on their spatial density. All particles and forces with their masses, charges and spines are
 246 summarised in Figure 2.1.

247 The SM serves as an exemplar of a quantum field theory, offering the mathematical
 248 underpinning for such a framework. The Lagrangian controlled the dynamics and kine-
 249 matics of the system satisfies the $SU(3) \times SU(2)_L \times U(1)_Y$ gauge symmetry, in which
 250 $U(1)_Y$ corresponds to a particle B with weak hypercharge Y . $SU(2)_L$ corresponds to
 251 particles W_α ($\alpha = 1, 2, 3$) with weak isospin T and only left-handed chiral particles.
 252 The electroweak force which unifies the electromagnetism and the weak interaction as a
 253 Yang-Mills field is represented by the group $SU(2)_L \times U(1)_Y$, mathematically. In SM,
 254 the Z^0 boson and the photon (γ) are given by:

$$\begin{pmatrix} \gamma \\ Z^0 \end{pmatrix} = \begin{pmatrix} \cos \theta_W & \sin \theta_W \\ -\sin \theta_W & \cos \theta_W \end{pmatrix} \begin{pmatrix} B \\ W_3 \end{pmatrix} \quad (2.1)$$

255 where θ_W is the weak mixing angle.

256 The charged massive bosons W^\pm are given by W_1 and W_2 :

$$W^\pm = \frac{1}{\sqrt{2}} (W_1 \mp iW_2) \quad (2.2)$$

257 $SU(3)$ corresponds to eight vector fields A^α ($\alpha = 1, 2, \dots, 8$) representing gluon fields,

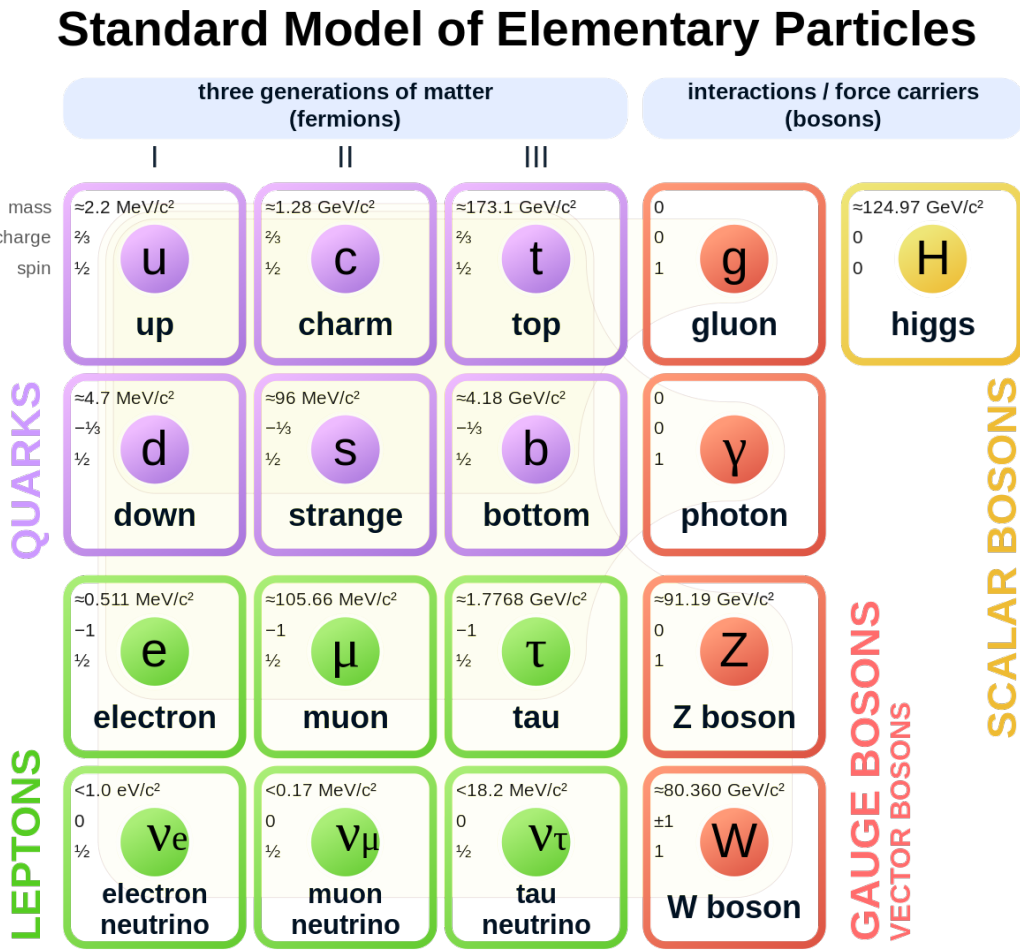


Figure 2.1 The Standard Model of particle physics

which are vector gauge bosons that carry the colour charge of the strong interaction and mediate between quarks in QCD. The Higgs boson, unlike all other known bosons such as the photon, is a scalar boson and has a non-zero average value in vacuum. It resulted from the process of spontaneous symmetry breaking. The Higgs mechanism explains the generation of the property "mass" for gauge bosons. At a critical temperature, the Higgs field introduces a vacuum expectation value that causes spontaneous symmetry breaking during interactions, leads the bosons it interacts with acquire masses. A Yukawa coupling is used in the SM to describe the interaction between the Higgs field and fundamental fermions, explain the generation of the masses of fermions.

This chapter therefore focuses on the present SM, various extensions and variants of the SM that have been proposed by theoretical physicists are explored in Section 2.2.

269 **2.1.1 Quantum chromodynamics**

270 QCD is the theory of the strong interaction between quarks and gluons, and it is a
 271 fundamental component of the SM of particle physics. Satisfying the $SU(3)$ symmetry
 272 group invariant, QCD is a non-abelian gauge theory, over the years, QCD has collected
 273 a huge body of experimental evidence, proved that it has been a successful application
 274 from a quantum field theory.

275 The Lagrangian of QCD can be expressed as:

$$\mathcal{L}_{\text{QCD}} = \bar{\psi}_i \left(i\gamma^\mu (D_\mu)_{ij} - m\delta_{ij} \right) \psi_j - \frac{1}{4} G_{\mu\nu}^a G_a^{\mu\nu} \quad (2.3)$$

276 where ψ_i is the quark field in the fundamental representation of the $SU(3)$ gauge group,
 277 indexed by i and j running from 1 to 3; m corresponds to the quark mass; the γ^μ are Dirac
 278 matrices relating the spinor representation to the vector representation of the Lorentz
 279 group.

280 D_μ is defined as the gauge covariant derivative:

$$(D_\mu)_{ij} = \partial_\mu \delta_{ij} - ig_s (T_a)_{ij} \mathcal{A}_\mu^a \quad (2.4)$$

281 which couples the quark field with a coupling strength g_s to the gluon fields via the
 282 infinitesimal $SU(3)$ generators T_a . By including the Gell-Mann matrices λ_a ($a=1\dots 8$), an
 283 explicit representation of T_a is defined by $T_a = \lambda_a/2$.

284 The gauge invariant gluon field strength tensor $G_{\mu\nu}^a$ is given by:

$$G_{\mu\nu}^a = \partial_\mu \mathcal{A}_\nu^a - \partial_\nu \mathcal{A}_\mu^a + g_s f^{abc} \mathcal{A}_\mu^b \mathcal{A}_\nu^c \quad (2.5)$$

285 where \mathcal{A}_μ^a are the gluon fields, indexed by a, b and c running from 1 to 8; f^{abc}
 286 are the structure constants of $SU(3)$. The coupling strength g_s can be referred to strong
 287 coupling constant α_s :

$$\alpha_s = \frac{g_s^2}{4\pi} \quad (2.6)$$

288 There are some salient properties that QCD exhibits:

289 **Colour confinement**

290 This is a consequence of the force between two colour-charged particles that can

291 not be isolated in a condition that below the Hagedorn temperature of approxi-
 292 mately 2 terakelvin. To separate two quarks in a hadron, extremely high energy
 293 is required, leading to the creation of a quark-antiquark pair that formed a pair of
 294 hadrons rather than a single hadron. In addition, glueballs which are formed only
 295 of gluons are colourless and also consistent with confinement, causing difficulty
 296 in identification in experiments.

297 **Asymptotic freedom and the running coupling**

298 This is a feature of QCD that demonstrates the strong interactions between quarks
 299 and gluons become asymptotically weaker as the energy scale of them increases
 300 and the corresponding length scale decreases. This is opposite to the behaviour of
 301 colour-charged particles at low energies where the confinement of quarks and glu-
 302 ons exhibits. At high energy, the coupling decreases logarithmically as a function
 303 of momentum transfer Q :

$$\alpha_s(Q^2) \stackrel{\text{def}}{=} \frac{g_s^2(Q^2)}{4\pi} \approx \frac{1}{\beta_0 \ln(Q^2/\Lambda^2)} \quad (2.7)$$

304 where β_0 is a one-loop beta function in QCD and has the dependence of the cou-
 305 pling parameter g_s . The quantity Λ is referred to QCD scale that is measured
 306 in processes where the strong coupling constant and other measurables vary with
 307 momentum transfer Q . However, this is only effective at leading order (LO). By
 308 including higher order terms, the calculation expanded in order of α_s resulted in
 309 more complexity and less significance as the scale of Q increases. On the other
 310 hand, as Q tends to be infinite large, the coupling strength becomes zero thus the
 311 behaviors of quarks are asymptotically free. These variation of coupling α_s under
 312 the different scales of energy in QCD is described as the running coupling.

313 The calculation of matrix element in QCD can be rather complex as more and more
 314 perturbative contributions are considered, which requires the application of complicated
 315 integrals over a large number of variables. A Feynman diagram is used as a representa-
 316 tion of the expressions of these integrals pictorially and an improvement of undertaking
 317 the critical calculations.

318 With more interactions points involved in, more complicated the calculations be-
 319 come. The effects of self-interactions between particles themselves can happen by pro-
 320 ducing a virtual particle which is restricted by the uncertainty principle, represented as a

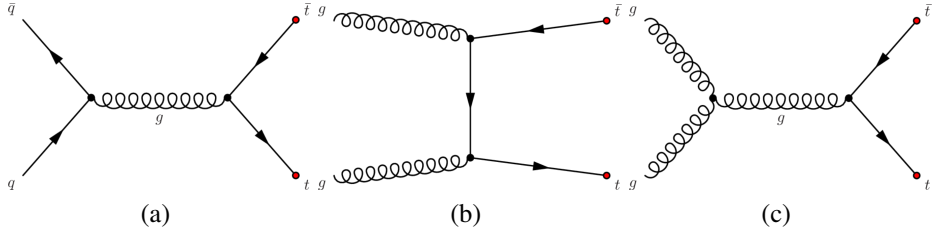


Figure 2.2 Feynman diagrams of strong interaction in top-antitop quarks production via (a) one gluon exchange in quark-antiquark annihilation, gluon-gluon fusion in (b) t-channel and (c) s-channel.

321 loop in a Feynman diagram. The accuracy of the calculation has dependency on the cou-
 322 pling α_s and is contributed to a fraction at each order. By including an infinite number
 323 of virtual particles, the calculations are led to divergent and infinite. A set of techniques
 324 named renormalization are employed in solving the infinities showed up in the calcu-
 325 lations, by which the infinite self-interactions are parameterised by re-scaling them as
 326 finite values to compensate the effects. The ultraviolet divergence that occurs from inte-
 327 grating the contributions at extreme high energy is represented by renormalization scale
 328 μ_R , on the contrast, μ_F represents the condition of an integral diverges at infinitesimal
 329 energy.

330 2.2 Physics beyond the Standard Model

331 2.2.1 String

332 A mathematical framework named string theory has contributed to a variety of prob-
 333 lems in the SM such as the existence of gravity, it offers a unified description of particle
 334 physics and gravity. String theory handles point-like particles as one-dimensional objects
 335 called strings and demonstrates the behaviours of these strings propagating through time
 336 and space. By regarding particles as infinitesimal vibrating strings, the charge, mass,
 337 and other properties of them are determined by the vibration or twist of the strings. A
 338 dynamical object called brane is employed to generalize the representation of a point
 339 particle to higher dimensions such that a string can be regarded as a brane of dimension
 340 one and can propagate through time and space under the principles of quantum mech-
 341 anics. Among them, a so-called Dirichlet membrane (D-brane) is widely used as the open
 342 strings satisfy the Dirichlet boundary conditions [27, 28, 29].

343 In this analysis, we consider type-II string theory [30] which includes a D-brane

344 localized in $p + 3$ partial dimension: D p -brane, compactified on a six-dimensional torus.
345 The choice of the string mass scale M_s is to be smaller than the 4-dimensional Planck
346 scale to keep the coupling small, at the expense of introducing $9 - p$ large transverse
347 dimensions felt only by gravity. Only the fundamental string scale in the TeV range is
348 what this analysis is interested in [31].

349 By considering the main subprocesses in dijet production that are independent of
350 the details of the compactification. Amplitudes, which include $2 \rightarrow 2$ scattering processes
351 involving two gluons and two quarks, or four gluons, are independent of the details of
352 the compactification such as the configuration of branes [32]. This model independence
353 makes it possible to compute the string corrections to QCD dijet processes.

354 **2.2.2 Kaluza-Klein Graviton**

355 In particle physics, Kaluza–Klein theory (KK theory) [33] is a significant concept
356 in physics. It's a classical unified field theory that attempts to unify gravitation and elec-
357 tromagnetism by introducing the notion of a fifth dimension beyond the four dimensions
358 of space and time that we commonly encounter. This theory is regarded as an important
359 precursor to more modern theories like string theory, which also incorporates the con-
360 cept of extra dimensions. KK theory's exploration of additional dimensions has played
361 a crucial role in advancing our understanding of fundamental forces and particles in the
362 universe.

363 in the context of the KK theory, the Randall-Sundrum (RS) [34] model is distin-
364 guished by its introduction of an extra dimension, which is constrained within finite
365 bounds by two distinct three-dimensional branes situated at either end. These branes
366 essentially represent the four-dimensional spacetime familiar to us, while the additional
367 spatial dimension is localized and limited within this confined region. This theoretical
368 framework was formulated as a potential solution to the hierarchy problem of the SM,
369 and it offers a unique perspective on the behaviour of gravity and fundamental forces
370 within our universe. In this model, there exist KK towers of massive spin-2 gravitons
371 that can interact with the SM fields. The graviton sector within the RS1 model is fully
372 determined by two key parameters: m_{KK} and k/\bar{M}_{Pl} , where m_{KK} is the mass of KK gravi-
373 ton, k is a scale of order the Planck scale, M_{Pl} is effective four-dimensional (reduced)
374 Planck scale.

375 **2.2.3 Quantum Black Hole**

376 Quantum Black Hole (QBH), also called micro black holes, is regarded as hypothet-
377 ical mini (less than a solar mass unit) black hole that dominated by quantum mechanical
378 effects [35]. Some hypotheses predict that QBH could be produced at energies as low as
379 the TeV range, which can be generated in particle accelerators such as the LHC and can
380 be observed through the particles that are emitted by the process of Hawking radiation.
381 Theoretical calculations indicate that as black holes decrease in size, their rate of evap-
382 oration accelerates. This phenomenon leads to an abrupt release of particles, akin to a
383 sudden eruption, when a micro black hole approaches its final stages of evaporation.

384 In the simplest scenario, the decay of QBH via Hawking radiation [36] can be ap-
385 proximately described as isotropic decay to a many-particle final state. The threshold
386 of quantum-gravity energy scale M_D is set to be well below the the actual thermal black
387 hole production threshold for gravitational interactions so that two-body states in final
388 states are the dominant, a resonance-like result is expected in predominantly two-body
389 final states as jets near M_D . Such isotropic final states is aimed as probes of quantum
390 gravitational effects in this dijet analysis.

391

3 The ATLAS Experiment

392

3.1 The Large Hadron Collider

393

The LHC, built by European Organization for Nuclear Research (CERN) located in Geneva, Switzerland, is the largest circular particle accelerator in the world. The goal of it is to probe the various theoretical predictions made by physicists.

396

It consists superconducting magnets that construct a 27-kilometer ring lying in the tunnel under the ground. Inside the LHC, two beams made of protons or ions are accelerated to extreme high speed in opposite direction in individual vacuum pipes then made into collision by a strong magnetic field within the structures.

400

The LHC is the last section of the CERN accelerator complex where a series of machines accelerates the particles to increasingly higher and higher energies. The highest energies of beams are reached at the LHC.

403

Seven detectors are placed around four collision points in the collider. Different types of particles are accelerated according to the research, the main beams are protons, but the LHC also run beams of heavy ions as lead–lead collision or proton–lead collisions.

406

The energy of particles is increased by a series of processes before being injected into the main accelerator. For a proton-proton collision, negative hydrogen ions are generated by the linear particle accelerator Linac4 at 160 MeV then injected into the Proton Synchrotron Booster, where protons are obtained by stripping electrons away from the atom and accelerated to 2 GeV. After entered the Proton Synchrotron the energy of the protons is 26 GeV, and then their energies are increased in Super Proton Synchrotron to 450 GeV before they are finally injected into the main ring.

413

One of the characteristics that defines the power of an accelerator is the centre-of-mass energy, which represents the total momentum of the system and thus indicates the total mass of potential new particles as well as probes the internal structure of known particles under the law of energy invariant within the system. In 2010, the first collisions were made at an energy of 3.5 TeV each beam, later in 2018, an energy of 6.5 TeV per beam was achieved, resulted in the centre-of-mass energy of 13 TeV where the protons moved at a 99.9% speed of light. It took less than 90 μ s for photons to go through the whole LHC ring.

421

Other quantities such as luminosity, denoted as \mathcal{L} , also represents the performance

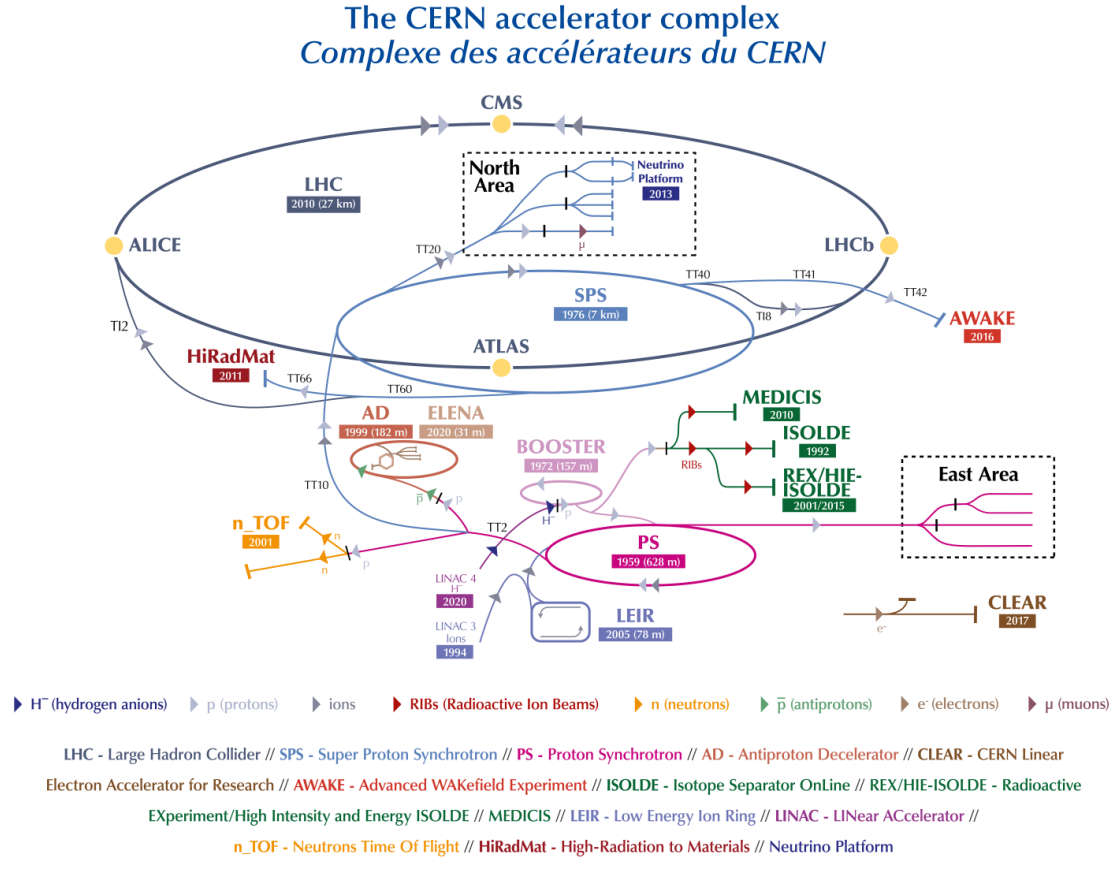


Figure 3.3 The CERN accelerator complex

of an accelerator. It is the rate of interactions during a certain period of time and can be expressed as:

$$\mathcal{L} = \frac{N^2 f_{rev}}{4\pi\sigma_x\sigma_y} \quad (3.1)$$

where N is the number of particles in a bunch, in the case that a beam has Gaussian distribution and has bunches crossing frequency f_{rev} . σ_x and σ_y denote as transverse beam widths in the x- and y-plane. The luminosity takes the units of $\text{cm}^{-2} \cdot \text{s}^{-1}$.

The total number of physics events detected can be express as:

$$N_{\text{event}} = \sigma_{\text{event}} \cdot \int \mathcal{L} dt \equiv \sigma_{\text{event}} \cdot L \quad (3.2)$$

where L is the integrated luminosity with respect to time, σ_{event} is referred to the cross section of a specific physics process. The integrated luminosity takes the units of

430 cm^{-2} which equals to the unit femtobarn (fb).

431 At the LHC, thousands of magnets around the accelerator are operated at a very
432 low temperature of 271.3°C to maintain its superconducting state which allow them to
433 conduct electricity without loss of energy. Hence, a system of liquid helium is used for
434 cooling the accelerator and supply services.

435 Besides, superconducting radio frequency cavities which resonate electromagnetic
436 fields are employed to accelerate the protons. Instead of having continuous beams, the
437 protons are made into bunches, so that the collisions are taken place at discrete intervals
438 between two beams with 115 billion protons per bunch at the frequency of 25 ns.

439 **3.2 The ATLAS detector**

440 The ATLAS detector [37] is the largest volume detector ever constructed for general-
441 purpose particle research at the LHC. It has the shape of a cylinder with 44 meters long,
442 7000 tonnes in weight and 25 meters in diameter, sitting in a cavern underground. It
443 is designed to collect evidence of the properties of SM and search for new predictions
444 made by particle physics beyond the SM.

445 To record the energy, momentum and trajectory of particles after collisions, the
446 detector consisting of 6 different detecting subsystems placed in layers surrounding the
447 interaction point to measure them individually and effectively.

448 An overall layout of the ATLAS detector is shown in Figure 3.4.

449 **3.2.1 Inner detector**

450 Charged particles above a certain p_T threshold are detected by the ATLAS Inner
451 Detector (ID) which immersed in a 2 T solenoidal field, covered the pseudorapidity range
452 $|\eta| < 2.5$. Appearing as tracks in the ID, an excellent momentum resolution as well as
453 both primary and secondary vertex of them are provided by the ID. Within the range
454 $|\eta| < 2.0$, electron identification is also provided.

455 The layout of the ID is shown in Figure 3.5 in cylindrical coordinate: $r = \sqrt{x^2 + y^2}$,
456 where x -axis alongside the LHC ring and y -axis is perpendicular to the x -axis.

457 A cylindrical container around the ID has a length of 3512 mm each way and a
458 radius of 1150 mm, tracks of 10 GeV traverse the sensors and structural elements in the
459 barrel and end-cap regions, respectively.

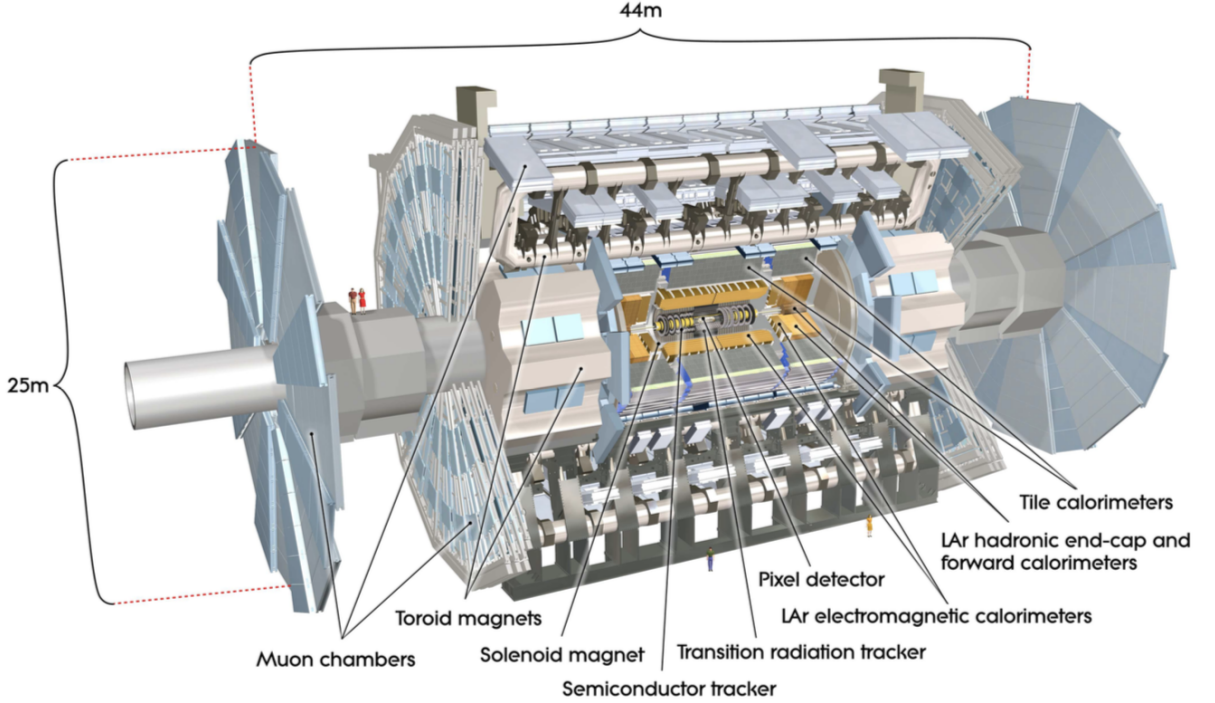


Figure 3.4 Cut-away view of the ATLAS detector

460 Within the inner region, a series of discrete space points provided by the silicon
 461 pixel detector and stereo pairs of silicon microstrip semiconductor tracking (SCT) lay-
 462 ers gives high-resolution pattern recognition abilities. By increasing radial distances,
 463 the transition radiation tracker (TRT) provides extra pattern recognition and momentum
 464 resolution capabilities.

465 **The pixel detector**

466 A series of high-granularity measurements is provided by the pixel detector [38]
 467 which is composed of the innermost sub-detector of the ID, it is designed as close
 468 to the interaction point as possible. Three sub-sections: two end-cap perpendicular
 469 to the beam axis and a barrel alongside the beam axis as a concentric cylinder with
 470 four layers (average radii of 33.25, 50.5, 88.5 and 122.5 mm, respectively) in it.

471 The innermost pixel layer (or B-layer, IBL) is essential to b-tagging performance
 472 and supersymmetry searches as it cover the full acceptance of short-lived parti-
 473 cles such as B hadrons and τ leptons from the beginning of Run-2 to enhance the
 474 measurement of the secondary vertex. Besides, a new readout sensor and chip
 475 responsible for higher radiation damage and higher hit rate, respectively, is em-

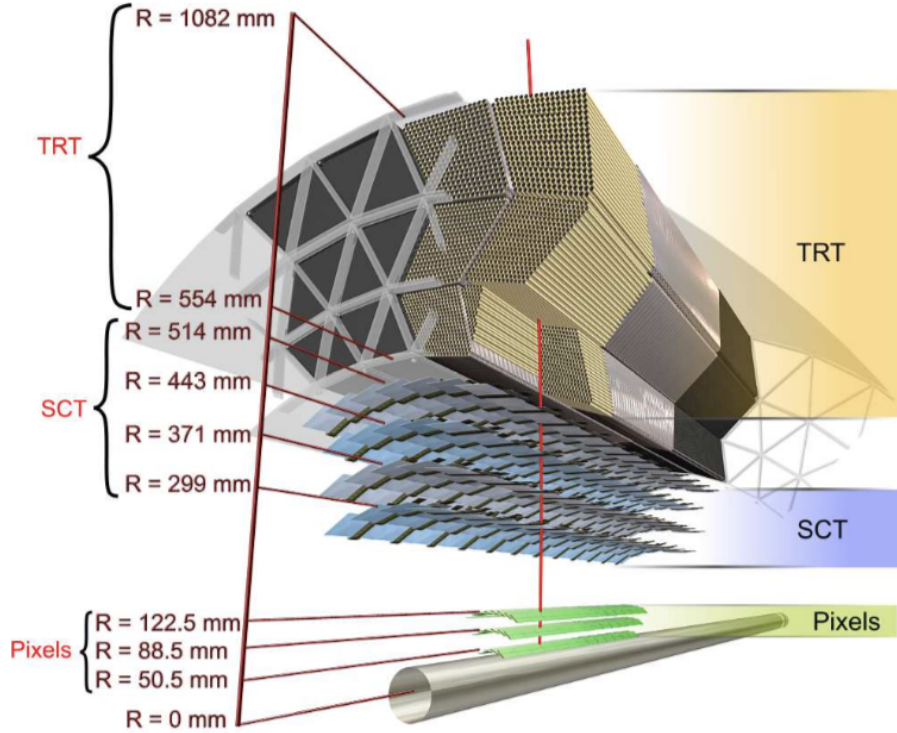


Figure 3.5 Cut-away view of the ATLAS ID. Sensors and structural elements traversed by a charged track of 10 GeV p_T in the barrel inner detector along with their envelopes in r .

476 employed in the IBL compared to the other three layers in the barrel region. A new
 477 n-in-n planar and 3D silicon sensors with hit efficiency of greater than 97% is de-
 478 veloped as well. The better impact parameter resolution is achieved by reducing
 479 the pixel size of the chip down to $50 \times 250 \mu\text{m}^2$. Around 80 million readout sec-
 480 tions counting them all provide the great hit resolution of $10 \mu\text{m}$ in radius plane
 481 and $115 \mu\text{m}$ alongside the z-axis in the pixel detector.

482 **The semiconductor tracker**

483 Surrounding the pixel detector is the SCT which encompasses silicon based semi-
 484 conductor sensing components in barrel and end-cap geometries. Four silicon mi-
 485 crostrip layers, located at radii of 300, 373, 447 and 520 mm, in the barrel region
 486 of the SCT provide high granularity points. The mean size of each strip pitch is
 487 $80 \mu\text{m}$ for the rectangular barrel sensors as daisy-chained with 6 cm-long. For
 488 the end-cap sensors, nine disks cover $|\eta| < 2.5$ are chosen. As a results, there are
 489 thus 768 readout strips with $6.36 \times 6.40 \text{ cm}^2$ in size in total, with additional two

490 strips at the edge of the sensor. 6.1 m² of silicon detectors with 6.2 million readout
491 channels as a whole intergrated the SCT.

492 **The transition radiation tracker**

493 The outermost layer of the ID is the TRT which encompasses polyimide drift(straw)
494 tubes that designed to enable as much less wall thickness and material as possible
495 while maintaining the good experimental properties. With 4 mm in diameter and
496 150 cm in length, 73 layers of 144 cm alongside the beam with 50 thousands tubes
497 and 37 cm tubes consisting 160 tubes planes in the end-cap with 320 thousands
498 radial tubes.

499 The xenon-based gas filled up in a given tube provides the track hit of a particle as
500 it ionized as the emitting electrons drifting to the center wire of the tube volume.
501 An average of 36 hits per charged-particle track is given by the TRT, The result-
502 ing electrical signals are obtained by converting the drifting charge currents. In
503 total 420 thousands of electronics channels in which a good spatial resolution and
504 drift-time measurement are provided by the TRT, enhancing the precision mea-
505 surements of momentum in the ID.

506 **3.2.2 Calorimeters**

507 Outside of the ID lies the ATLAS calorimeters system which is designed to obtain
508 the energy lost of the particles that travel through the detector components. Multiple
509 layers of high-density material are placed to consume the energy of the incoming par-
510 ticles inside the materials and stop them from further moving. An “active” medium
511 is left inside the layers that allows experimental physicists measure the energy of those
512 particles.

513 Two types of calorimeters are employed in the ATLAS calorimeters system: the en-
514 ergy of electrons and photons are measured by the electromagnetic calorimeters as they
515 create reaction with matter. Hadronic showers that created by the interaction between
516 hadrons and atomic nuclei, are sampled by the hadronic calorimeters. Muons and neutri-
517 nos can not be stopped by the calorimeters as they interact only weak force but the track
518 footprints could be seem in the calorimeters. The layout of the calorimeters is shown in
519 Figure 3.6.

520 The electromagnetic (EM) calorimeter covers a range of $|\eta| < 3.2$ by combining
521 the one barrel and two end-cap modules as cylindrical cryostat, with an outer radius of

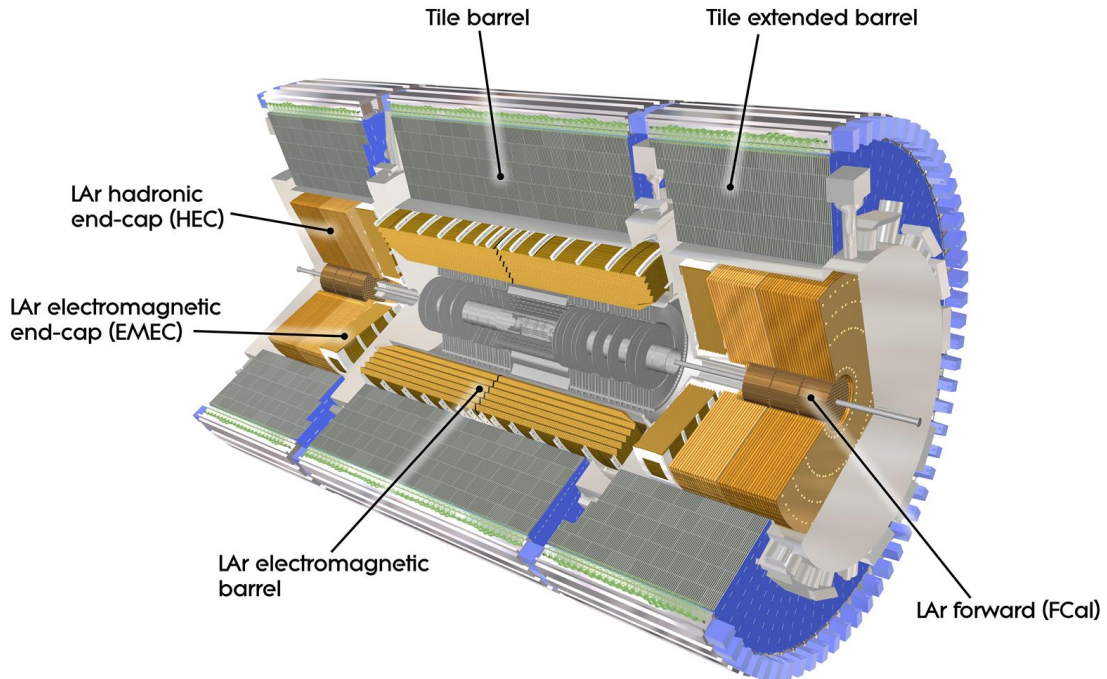


Figure 3.6 Outline of the ATLAS Run 2 trigger and data-acquisition system.

522 2.25 m, an end-cap thickness of 0.632 m and a length of 3.17 m. The hadronic calorimeter
 523 covers the central barrel region of $|\eta| < 1.0$ and two extended barrels in a region of
 524 $0.8 < |\eta| < 1.7$, with a radius of 2.28 m at the inside and 4.25 m at the outside. Figure
 525 3.7 demonstrates the positions of the end-cap of the calorimeters including the EM
 526 and Hadronic calorimeters.

527 **The electromagnetic calorimeter**

528 The EM calorimeter that surrounds the ATLAS ID is designed for the high-
 529 granularity measurements of the energy of photons, electrons and hadrons with
 530 Liquid Argon (LAr) sandwiched between the multiple layers ionised. It converts
 531 the incoming particles into electric currents by absorbing the energy of these par-
 532 ticles as they interact with the metal with the bremsstrahlung phenomenon. A pair
 533 of electron-positron produced by an electron radiation in the EM calorimeter can
 534 initiate further electron-positron pairs (as showers) until the energy of the parti-
 535 cles fall below the certain threshold, the dominate process thus become ionisation
 536 in the LAr where drifting electrons are produced. Furthermore, the missing trans-
 537 verse energy can be obtained by subtracting the total energy of the known particles,

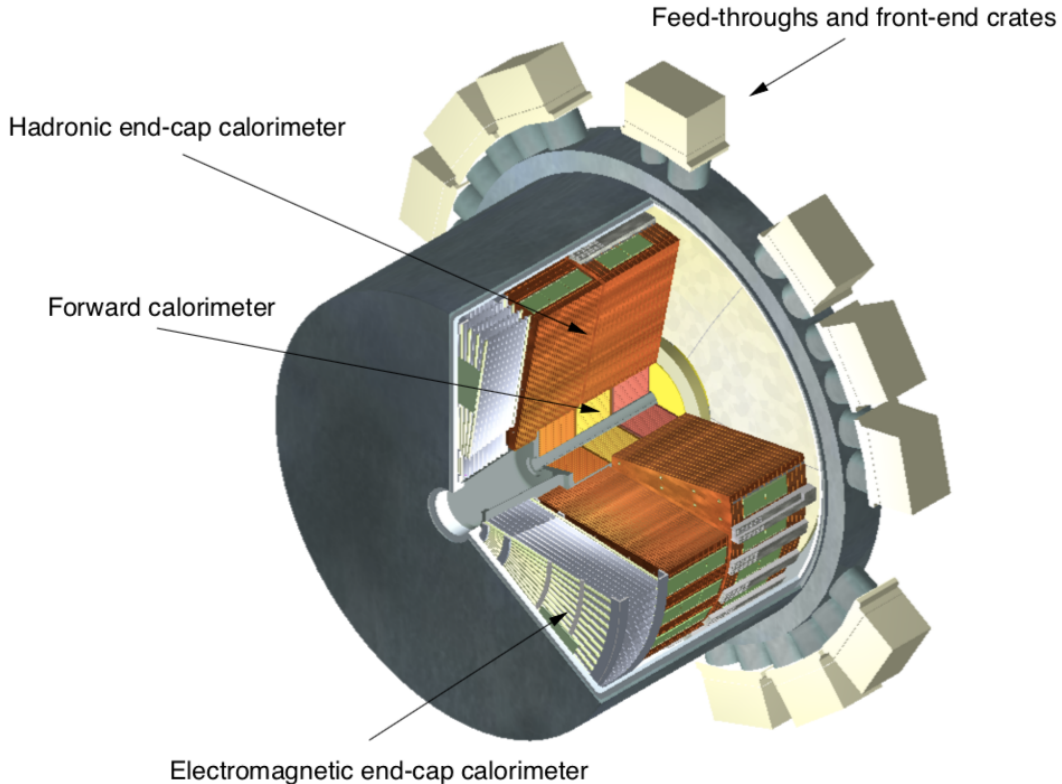


Figure 3.7 Cut-away view of an end-cap cryostat of the ATLAS calorimeter system.

538 which contributes to the analysis of neutrinos and new particles.

539 At -184 °C where the argon exists in liquid form, the calorimeter is kept as the
 540 cables that transverse electronic signals are sealed in vacuum and connected to the
 541 warmer area where located the readout system.

542 **The hadronic calorimeter**

543 Surrounded the EM calorimeter, lies the tile hadronic calorimeter where hadrons
 544 that contain strong force thus could not fully deposit their relatively large energy in
 545 the EM calorimeter are absorbed by the tile calorimeter. Steel and plastic scintillat-
 546 ing tiles are placed in layers in order to record the trajectories of incoming particles
 547 as hadronic showers are formed by the interactions of the particles with the ma-
 548 terials and emitting particles continue interacting with materials in the hadronic
 549 calorimeter and more particles are produced in steel layers. On the other hand,
 550 photons are produced by the plastic scintillators where electric currents are gained
 551 according to the energy of the particle.

552 By enveloping the EM calorimeter, a hadronic shower that contained EM showers
 553 can be fully absorbed by the great thickness in the hadronic calorimeter. Around
 554 420 thousands of plastic scintillator tiles are placed in sync, leading a weight of
 555 2.9 thousands tonne in total.

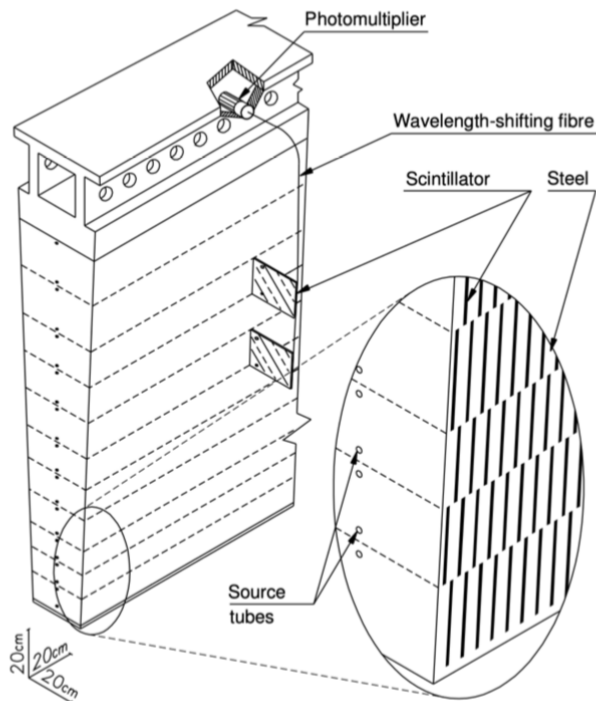


Figure 3.8 A schematic view of a tile calorimeter components of optical readout tiles and scintillating tiles.

556 As illustrated in Figure 3.8, photomultiplier tubes (PMT) are placed around the
 557 outer radii of the tile calorimeter and connected with wavelength-shifting fibres
 558 by which scintillation light is transferred. Projective geometry is designed for
 559 the whole readout system as the energy of most hadronic showers is deposited in
 560 the first or last two layers. Though the coarser granularity of the readout cells
 561 of hadronic calorimeter has been compared to the EM calorimeter, the hadronic
 562 calorimeter is qualified for the measurement of transverse momentum and jet re-
 563 construction.

564 In the forward regions, the hadronic calorimeters are integrated with LAr calorime-
 565 ters due to higher radiation exposition compared to the barrel regions. There are
 566 two calorimeters that were developed to tackle such issue: the hadronic end-cap

567 calorimeter (HEC) that covers $1.5 < |\eta| < 3.2$ and the forward calorimeter (FCal)
568 that covers $3.1 < |\eta| < 4.9$.

569 The HEC located further beside the EM end-cap calorimeter has two wheels in
570 each end-cap. LAr is used for filling up 8.5 mm between copper layers in the HEC,
571 by which the active medium is provided. The readout electrodes are provided in
572 separate drift zones in order to secure the stability of the whole system. The FCal
573 has three wheels placed alongside the z-direction: one electromagnetic layer (FCal
574 1) and two hadronic layers (FCal 2 and FCal 3). LAr is also used as an active
575 medium in all of the layers. As for the absorber, copper is employed in FCal 1 as
576 it has heat removal properties. Tungsten is used in both FCal 2 and FCal 3 in order
577 to constrain the lateral spread of hadronic showers.

578 **3.2.3 Muon spectrometer**

579 The muon spectrometer (MS), specially designed for the muon detection is located
580 in the outermost section of the ATLAS in order to provide sufficient measurement of
581 high-momentum muons which are almost "invisible" to the ID and calorimeters due to
582 little energy deposit when traveled through them. By deflecting the trajectories of
583 muons, the MS employs the magnetic field by a barrel toroid magnet system in $|\eta| < 1.4$
584 and end-cap toriod systems in $1.6 < |\eta| < 2.7$.

585 Four subsections of the MS: add up to 4000 separate muon chambers. Thin Gap
586 Chambers (TGC) and Resistive Plate Chambers (RPC) account for triggering and the
587 second coordinate measurement of muons. TGC is set at the end of the detector whereas
588 RPC which provides 5,000 V/mm electric field is placed in the central region. Monitored
589 Drift Tubes (MDT) is designed for the curve of muon tracks measurement with fine tube
590 resolution of 80 μm . Cathode Strip Chambers (CSC) accounts for measuring coordi-
591 nates precisely located at ends of detector with a fine resolution of 60 μm . Figure 3.9
592 demonstrates the MS with all four subsections. In total three separate points within the
593 muon trajectory are measured to reconstruct the momentum of the muon.

594 **3.2.4 Trigger and data acquisition**

595 At the LHC, approximately 1.7 billion proton-proton collisions occur per second at
596 an integrated luminosity of 140 fb^{-1} . However, many of these collisions are unlikely to
597 produce characteristics of interest. As a result, large numbers of events can be discarded

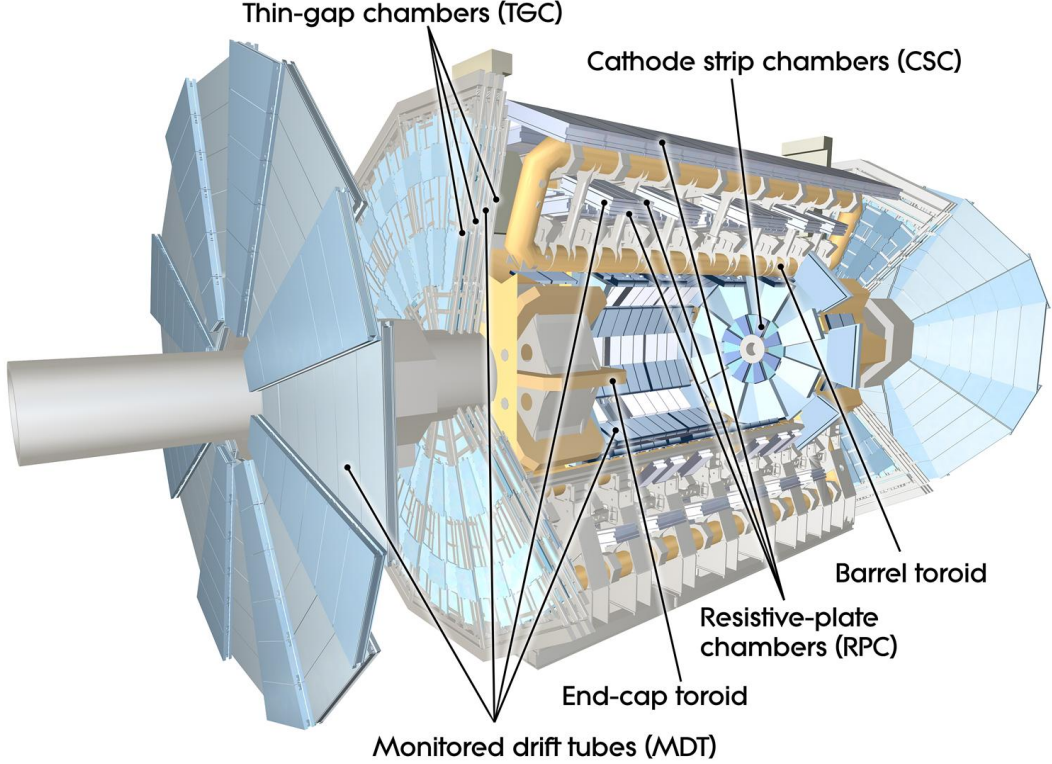


Figure 3.9 Cut-away view of the ATLAS Muons Spectrometer with subsections labeled.

598 without affecting the search for new physics. The trigger and data acquisition systems
 599 are introduced to eliminate the irrelevant data so that only events of suitable quality and
 600 quantity are recorded.

601 During the year of 2015-2018, the trigger system in ATLAS selected significant
 602 events in a two staged process, as illustrated in Figure 3.10: The first-level (L1) trigger is
 603 implemented on hardware, and reduced event rates from 40 MHz to 100 kHz in less than
 604 2.5 μ s right after the data happened. Working with the electrical information provided
 605 by the calorimeters and the MS, the L1 trigger employs custom-made electronics to filter
 606 and store the events in the readout sections as buffers before passing them to the High-
 607 Level trigger (HLT) [39]. Certain physics objects such as photons, jets and leptons are
 608 identified in the L1 trigger, in which energy depositions of electrons and photons in the
 609 EM calorimeter and jets in the hadronic calorimeter are provided. Information of tracks
 610 in high-momentum muons is recorded in the layers of the MS and forwarded to the L1
 611 trigger.

612 The events are further reduced from 100 kHz to 1 kHz in merely 250 microseconds

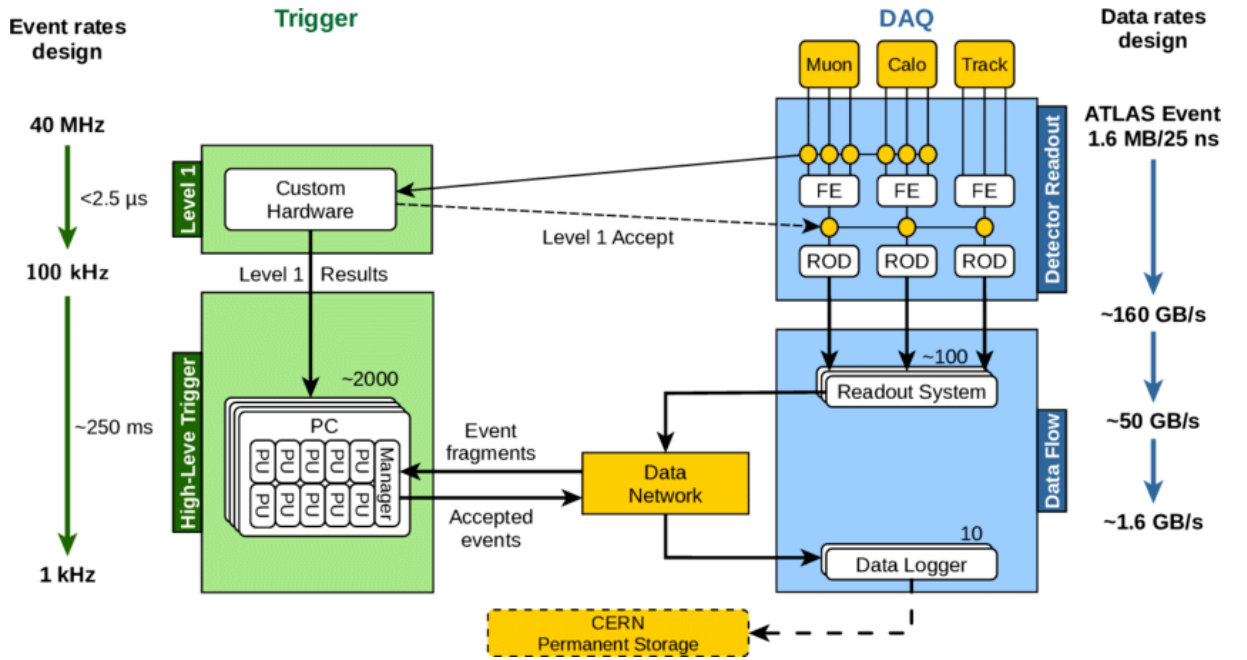


Figure 3.10 illustration of the ATLAS Run 2 trigger and data acquisition system.

613 by the second level trigger: HLT. Based on the offline software, the HLT utilize fast
 614 selection algorithms to analyse and reject events in the early stage, resulting in better
 615 precision and intense CPU usage of about 1.6 GB per second. The accepted data from
 616 the HLT will be passed to permanent storage at CERN via Data Logger [40].

617

4 Jets in ATLAS

618 In the LHC, a large number of quarks and gluons are produced during the inelastic
 619 proton-proton collisions, resulting in jets. These collimated outcome particles are hadro-
 620 nised because of colour confinement in the QCD process. As a result of this, only colour-
 621 neutral jets clustered by particles can be seen in the detector.

622 The information of jets is crucial to most of the analysis such as the measurements
 623 of the SM particles and searches for the BSM phenomena. Good qualities of jets, for
 624 example the high efficiency of jet reconstruction, jet energy calibration including energy
 625 scale and energy resolution, are thus important to the analysis.

626 **4.1 Jet reconstruction**

627 Jets are defined in two way: Monte Carlo (MC) simulated jets at particle level and
 628 detector level jets with the information from the ID and calorimeters. The production
 629 and hadronisation processes of jets are illustrated in Figure 4.11.

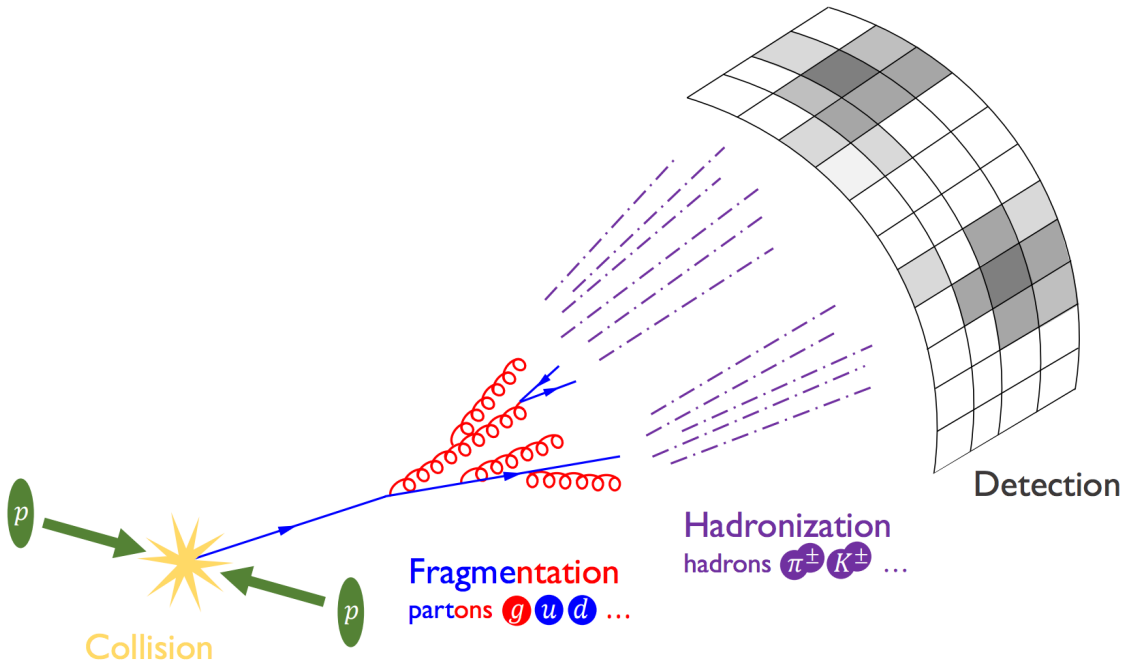


Figure 4.11 illustration of jets produced by pp collision and hadronised before seen by the detector.

630 Jets from the MC simulation are defined as truth-particle jets which have lifetimes

longer than 10 ps as stable particles. Truth-particles indicate the ideal measurement from a detector under perfect-condition and high resolution without defects or the effects from pile-up (background interactions per bunch-crossing in the LHC). Whereas track jets are constructed with the use of charged information in the ID, and calorimeter jets with the use of energy information in the calorimeters.

There are several types of jets aim for different analysis depended on the constituents and algorithm used for reconstructing the jets. ATLAS previously used topo-cluster jets, which is a group of topological related cells in calorimeter with significantly high energy deposits. A pile-up suppressed algorithm is applied to select certain cells with low noise. Cell above certain signal-to-noise (S/N) threshold (usually by four times its standard deviation) are used to seed the algorithm. By neighbouring the seed a topo-cluster is defined. In the hard-scatter process, jets of interest are expected to produced from the primary interaction point (known as vertex). The primary vertex is defined if there are at least two tracks with the highest sum of squared track momentum associated to it.

Jets are constructed from any set of four-vectors. EMTopo jets are the jets that use topo-cluster initially calibrated to electromagnetic (EM) scale in the calorimeters. A local cluster weighting (LCW) scale is also used for calibrating hadronic clusters by applying weights for low hadronic interaction response. Besides, particle flow (PFlow) [41] jets are built by combining the information from both the ID and the calorimeter, where the energy deposited from the calorimeter are removed by the momentum in the ID by a cell-based energy subtraction algorithm. The inputs to the particle flow algorithm are the separate topo-clusters with local energy maxima, respectively.

A recombination algorithm called anti- k_t algorithm is employed to build the jets with a radius parameter R in rapidity-azimuth ($y - \phi$) plane around a cluster. The algorithms are defined as follows:

$$d_{ij} = \min \left(k_{ti}^{2p}, k_{tj}^{2p} \right) \frac{\Delta_{ij}^2}{R^2} \quad (4.1)$$

$$\Delta_{ij}^2 = (y_i - y_j)^2 + (\phi_i - \phi_j)^2 \quad (4.2)$$

$$d_{iB} = k_{ti}^{2p} \quad (4.3)$$

where the distance d_{ij} between any pair of particles i and j is given by the minimum transverse momenta k_t of the two particles. The geometrical distance Δ_{ij} represents the separation of a pair of particles in $(y - \phi)$ plane. Radius parameter R indicates the size of the final jets. The distance d_{iB} between any detected particle i and the beam B is also given. Parameter p indicates the relative power of energy with respect to geometrical scales and is used to distinguish the different types of algorithms.

When p is set to 0, the Cambridge-Aachen (CA) algorithm is given as the distance d_{ij} and d_{iB} only based on spatial separation and are independent of the transverse momenta. This algorithm is usually used for large-radius jets and jet substructure performance study.

For the k_t algorithm, p is set to 1 so that the distance d_{ij} is dominated by the minimum k_t . This algorithm is preferred for clusters that are soft and collinear splits are merged first, resulted in irregular footprint with the most interesting splits.

The algorithm [42] on the other hand set $p = -1$, leaving the distance $d_{ij} \propto \min\left(\frac{1}{k_{ti}^2}, \frac{1}{k_{tj}^2}\right)$ shorten as the transverse momenta of two particles increase. This is widely used in the LHC for hard clustering as it is less vulnerable to the effects from the pile-up and resulted in circular footprint as shown in Figure 4.12 for $R = 1.0$.

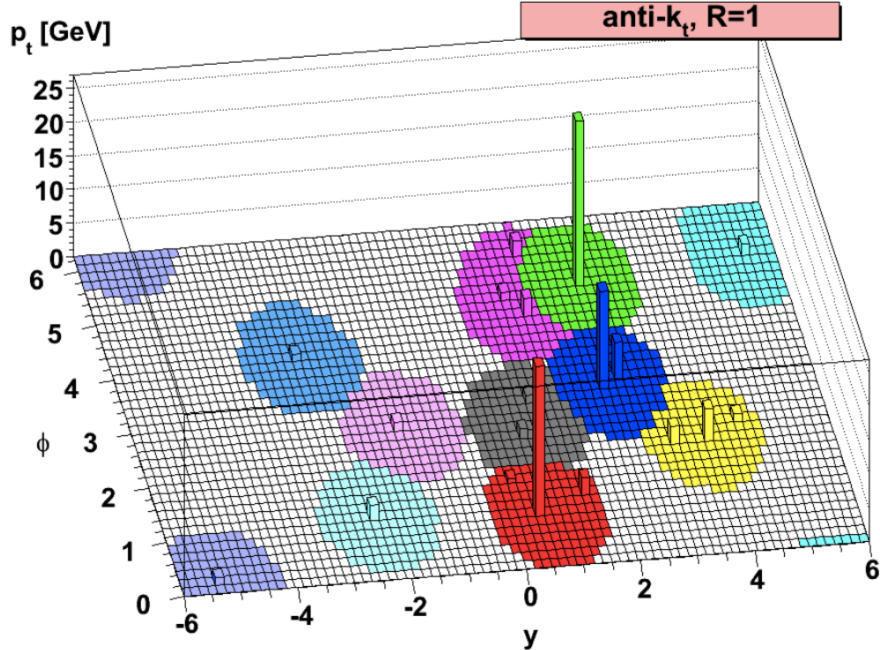


Figure 4.12 Plot of parton-level jets clustered using algorithms with radius parameter set to 1.

For most of ATLAS analysis, jets with $R = 0.4$ are used for quarks and gluons

analysis. Other ones such as $R = 1.0$ are also widely used to study energetic particles like W and Z bosons. $R = 0.2, 0.6, 1.2, 1.5$ and variable radii are also analysed.

The $R = 0.4$ PLow jets are used in the quark/gluon taggers calibration described in this thesis.

4.2 Jet calibration and cleaning

The motivation of jet calibration [43, 44] is to correct the translation from received signals to initial partons for several detector effects, including energy deposited in dead or beyond areas in the detectors, low response to hadronic reactions, pile-up, radiations that outside jet cone, etc. The calibration process is thus needed to account for the energy of jets to that of MC simulated jets at particle-level.

Calibration is performed to topological clusters at the EM scale where the sum of the energies in all constituent cell are taken, or at the LCW scale where low hadronic response in the ATLAS calorimeters is taken into account. The diagrams 4.13 shows the calibration scheme for small- R jets.

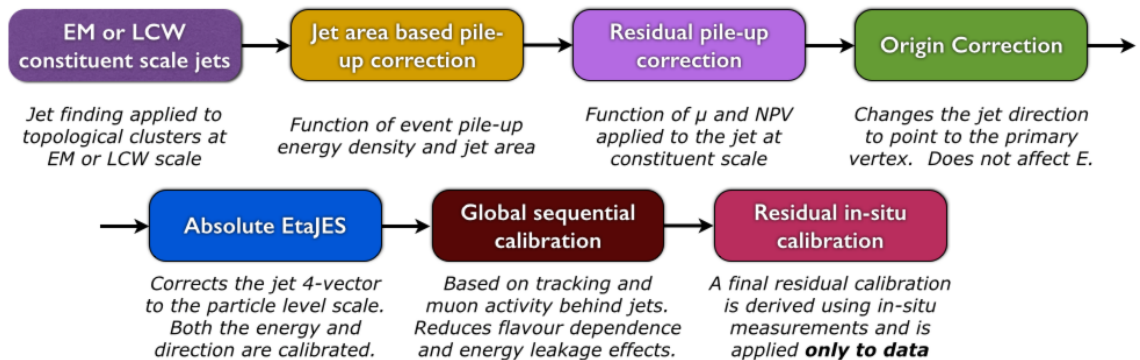


Figure 4.13 Overview scheme of jet calibration in the ATLAS.

4.2.1 Pile-up corrections

In order to eliminate a great amount of energy deposits from pile-up, a jet area-based subtraction of pile-up contribution to the p_T of each jet per event is applied as the start of the calibration chain.

After all pile-up corrections are applied, the jet p_T is given by:

$$p_T^{\text{corr}} = p_T^{\text{reco}} - \rho \times A - \alpha \times (N_{\text{PV}} - 1) - \beta \times \mu \quad (4.4)$$

where p_T^{reco} indicates the reconstructed jet p_T before any pile-up correction is applied. The jet area A is defined by certain number of ghost tracks associated with a jet after clustering thus can quantify the liability of a jet to pile-up. The pile-up p_T density ρ is used to evaluate the contribution from pile-up in the y - ϕ plane. To calculate the density ρ of each jet in the distribution p_T/A , a k_t algorithm with radius $R = 0.4$ is employed to reconstruct jet from positive-energy topo-clusters within the range of $|\eta| < 2$. The calculation of ρ performed in such η range for pile-up measurement is due to the fact that ρ tend to be zero beyond $|\eta| \approx 2$ as a result of lower occupancy in coarser segmentation in the forward region. Therefore, pile-up sensitivity in the forward region is not fully described after such correction.

An additional residual correction is thus applied from the MC simulation to account for the difference between the reconstructed jet p_T and truth jet p_T as a function of the number of reconstructed primary vertices in the event N_{PV} and the mean number of interactions per bunch crossing μ , which are sensitive to in-time and out-of-time pile-up, separately.

Both the initial values of α and β coefficients are derived in bins of truth jet p_T and geometric centre of the detector $|\eta_{\text{det}}|$. A logarithmic dependence on truth jet p_T is observed.

4.2.2 Jet energy scale and η calibration

Following the pile-up mitigation, the absolute jet energy scale and η calibration are introduced to correct the four-momentum of the reconstructed jet to the truth-particle jets, accounting for defecting calorimeter response, energy losses when particles passed through certain materials, boundary effects and biases in the reconstructed jet in different η due to the transition between the granularities and technologies changes in calorimeter.

Since the detector responses differ across the detector η range, the reconstructed jets are thus divided into small bins of η_{det} and the energy of the truth jet E^{truth} as the response distribution for fixed E^{truth} is Gaussian. The average jet energy response \mathcal{R} is defined as $E^{\text{reco}}/E^{\text{true}}$ using the mean of a Gaussian fit in η_{det} and E^{truth} bins, and is further parameterized as a function of E^{reco} . Such response for PFlow jets is higher than that for EMtopo jet at low energies as the tracking information is considered.

Besides Jet energy scale (JES) correction, the bias from the η of the reconstructed jet to that of the truth jet is taken into account. The bias is defined as a significant devi-

726 ation from zero in the signed difference between the reconstructed jet η^{reco} and truth jet
 727 η^{truth} , separately. Then a second correction is applied as such difference is parameterized
 728 as a function of η_{det} and E^{truth} .

729 The calibration is derived as a function of energy and η from the MC samples which
 730 do not have the effects from pile-up, and only correct the jet p_T and η instead of full four-
 731 momentum. The EMtopo and PFlow jets after full JES and η calibration are regarded as
 732 EM+JES scale and PFlow+JES scale, respectively. Small non-closures beyond $|\eta_{det}| \approx$
 733 3.2 in the calibration are seen due to approximate treatment of hadronic showers in the
 734 forward region, lead to an additional systematic uncertainty.

735 4.2.3 Global sequential calibration

736 The global sequential calibration (GSC), based the global jet observables such as
 737 the fraction of jet energy measured in the different layer of hadronic and the EM
 738 calorimeters, the tracking information associated with the jets, and the number of muon
 739 track segment. For each observable, a series of multiplicative corrections are applied on
 740 the four-momentum as a function of p_T^{truth} and $|\eta_{det}|$. Considered any observable x , the
 741 correction is derived from the inverted jet response \mathcal{R} :

$$C(x) = \frac{\mathcal{R}^{-1}}{\langle \mathcal{R}^{-1}(x) \rangle} \quad (4.5)$$

742 where $\langle \mathcal{R} \rangle$ is the average jet response.

743 As a result, the fluctuations in the jet particle composition are reduced and the jet
 744 resolution can be improved without changing the average jet energy response which
 745 depends on the flavour and the energy distribution of the constituent particles. The shape
 746 of a jet varies between quark- and gluon-initiated jets as hadrons are often included in a
 747 quark-initiated jet with higher fraction of the jet p_T with higher calorimeter response.

748 After applied GSC for PFlow jet, the average jet p_T response on each observable is
 749 reduced to lower than 2% with small deviations from correlations between observables.

750 The fractional jet resolution $\sigma_{\mathcal{R}}/\mathcal{R}$ is derived from the jet resolution $\sigma_{\mathcal{R}}$, which is
 751 defined by the standard deviation of a Gaussian fit to the distribution of jet p_T response.
 752 This fractional jet resolution is used to determine the size of the fluctuations in the jet
 753 energy reconstruction.

754 **4.2.4 Residual *in situ* calibration**

755 The final step of the jet calibration is performed only in data to account for the
756 differences of jet response measurement in data and the MC, the derived ratio of it is
757 used as a correction in data. The differences are introduced by the inadequate nature of
758 the detector materials and the imperfect simulation of the real physics processes. Such
759 differences can be quantified by weighting the p_T of a jet to other reference objects that
760 are well-measured. The correction factor can be denoted as follows:

$$c = \frac{\mathcal{R}_{\text{in situ}}^{\text{data}}}{\mathcal{R}_{\text{in situ}}^{\text{MC}}} \quad (4.6)$$

761 the response $\mathcal{R}_{\text{in situ}}$ represents the average ratio of the jet p_T to the reference object
762 p_T in bins of reference object p_T , where the average value is founded from peak value
763 of a Gaussian fit to the distribution. The double ratio is robust to secondary effects thus
764 more reliable in term of the measurement of jet energy.

765 Three stages are carried out in such *in situ* calibration. First, η -intercalibration is
766 performed on the energy scale of forward jets ($0.8 \leq |\eta_{\text{det}}| < 4.5$) to match the central jets
767 ($|\eta_{\text{det}}| < 0.8$) using the jet p_T in dijet events. Then $Z+\text{jet}$ and $\gamma+\text{jet}$ analyses balance the
768 measurement of p_T response of a well-calibrated Z boson or photon. Finally, a multijet
769 balance (MJB) analysis is employed to calibrate low- p_T jets to a very high- p_T jet. Both
770 MJB and $Z/\gamma+\text{jet}$ analyses are used only for jets in the central region ($|\eta| < 1.2$). All
771 three *in situ* calibrations are done sequentially so that the systematic uncertainties can be
772 propagated from each to the next. The systematic uncertainties in each calibration pro-
773 cess come from three sources: the MC modelling of physics processes, the uncertainties
774 in the measurement and from topology obtained by different event selections.

775

5 The calibration of quark/gluon jets taggers

776 The classification of jets originated from a quark or a gluon is useful for improving the
777 SM measurements and searches for BSM physics at the LHC. According to the QCD,
778 gluons are in the adjoint representation of the $SU(3)$ gauge group thus carry both colour
779 and anti-colour quantum numbers, whereas quarks are in the fundamental representation
780 and have only a single colour number [45]. As a result, a gluon-initiated jet (gluon-jet)
781 tend to have more constituents and a broader radiation pattern than a quark-initiated jet
782 (quark-jets).

783 The manifestation of colour charges is intrinsic to quarks and gluons; however,
784 the confinement phenomenon inherent in QCD theory indicates that only colour neutral
785 hadrons can be observed in the detector. Such principle brings significant challenges
786 for the identification of quark- or gluon-jets in ATLAS. The identification method relies
787 on the number of charged tracks within the jets and the reconstruction algorithm for
788 it. The calibration described in this paper demonstrates the measurement of the tagging
789 efficiencies of the aforementioned jet taggers. The more advanced boosted decision tree
790 (BDT) algorithm is employed to constructed the jet tagging variable based on the charge
791 multiplicity inside jets. A matrix method is established with the use of quark/gluon
792 fraction in quark-/gluon-enriched subsamples, defined by the pseudorapidity of jets. The
793 scale factors extracted from the difference between data and simulation are provided
794 for tagger working points corresponding to 50%, 60%, 70% and 80% fixed quark-jet
795 efficiencies for both quark- and gluon-jets, respectively.

796 In addition to earlier investigations that concentrated on single-variable taggers
797 within a lower p_T range [46, 47], this research emphasizes the development of a novel
798 q/g tagger that incorporates multiple jet substructure parameters. Additionally, it aims
799 to expand the application of q/g tagging to a broader energy spectrum.

800 5.1 Data and Monte Carlo samples

801 5.1.1 Data

802 The data recorded in 2015-2018 with integrated luminosity of 140 fb^{-1} (full Run 2
803 data)[48] is used in this study. The data samples are processed through the un-skimmed
804 DAOD_JETM1 derivation scheme in order to obtain multi-jet events. The lowest un-

prescaled small- R single-jet trigger is employed for this analysis. The jet p_T threshold for the trigger in this analysis is 420 GeV, keeping the selection consistent across years, together with additional requirements that ensure events of good qualities are used [49].
 The additional selections are:

- Good Run List (GRL): Make sure a steady state of all relevant detectors so that physics processes recorded by them are good.
- LAr: Liquid Argon Calorimeter error rejected.
- Tile: Tile Calorimeter error rejected.
- SCT: SCT single event upsets rejected.
- Core: Incomplete event build rejected.
- Primary Vertex: the highest $\sum p_T^2(\text{trk})$ vertex has at least two tracks associated with it
- Trigger: Passes the lowest unprescaled single-jet trigger, HLT_j420

Additional kinematic selection criteria are discussed in Section 5.2.

5.1.2 Monte Carlo simulation

For this calibration, multi-jet events are generated and modelled with several MC simulations, processed through the same DAOD_JETM1 derivation scheme. For the nominal result, PYTHIA 8.230 [50] MC generator is used with leading-order (LO) matrix element (ME) for dijet production. Parton density functions (PDFs) are considered for systematic uncertainties evaluation as the PDF set [51] is used for PYTHIA 8.230 with the A14 tune [52]. Alternative samples with different choices of parton shower modelling, ME generation, and the simulation of the multi-parton interactions are included to estimate the systematic uncertainties.

Two set of MC samples generated using SHERPA 2.2.5 [53] are used with the same ME for the (2→2) process at LO, to provide the uncertainties of hadronisation modelling [54, 55]. The CT10 PDF [56] sets are included in both SHERPA samples where one based on the cluster hadronisation whereas the other used SHERPA interface to the Lund string fragmentation [57] model as PYTHIA 8.230.

833 Two set of MC samples generated using HERWIG 7.1.3 [58] are used for parton
 834 shower uncertainties as one uses angular ordering shower whereas the other one uses
 835 dipole shower. These samples are produced at next-to-leading order (NLO) with a PDF
 836 set of MMHT [59].
 837

837 Another set of multijet samples that produced with POWHEG [60, 61, 62] interfaced
 838 to PYTHIA at NLO accuracy is employed with NNPDF2.3 LO PDF [63] set, to estimate
 839 the effects from the ME uncertainty as different perturbative scales in the ME and parton
 840 distribution functions are included. The renormalization and factorisation scales are set
 841 to the p_T of the underlying Born configuration. These samples included different pertur-
 842 bative scales in the ME and parton distribution functions are used for the estimation of
 843 ME uncertainty.
 844

A list of the MC samples used is given in table 5.1.

PDF set	Generator	Cross-section	Parton shower	Hadronisation
NNPDF2.3	PYTHIA 8.230	LO	p_T -ordered	String
CT10	SHERPA 2.2.5	LO	p_T -ordered	Cluste
CT10	SHERPA 2.2.5	LO	p_T -ordered	String
MMHT	HERWIG 7.1.3	NLO	Dipole	Cluster
MMHT	HERWIG 7.1.3	NLO	Angular-ordered	Cluster
NNPDF2.3	Powheg+PYTHIA	NLO	p_T -ordered	String

Table 5.1 The MC simulation used for the multi-jet processes in this calibration. The PDF sets, generators for a hard process, the order in α_s of cross-section calculations and the simulator of parton showers, and hadronisation are shown.

845 5.2 Object and Event selection

846 In order to perform the calibration of the quark-/gluon-jet tagger, it is requisite to
 847 establish two distinct subsamples. One subsample should be predominantly composed of
 848 quark-jets, called quark-enriched sample, while the other should predominantly consist
 849 of gluon-jets, as gluon-enriched sample. These subsamples are gained from the dijet
 850 events. This section describes the reconstruction and selection of jet objects used in this
 851 calibration, as well as the approach to construct quark- and gluon-enriched subsamples.
 852

852 **5.2.1 Physics object definition**

853 The PFlow jets that are reconstructed with the algorithm with a radius parameter
 854 R set to 0.4. An overall jet energy calibration described in section 4.2 has been done
 855 to rectify residual detector effects and pile-up. In order to ensure a good quality jet, an
 856 event-based jet cleaning with standard loose cut is applied to reject events with flawed
 857 leading or subleading jet.

858 Tracks that reconstructed [64] from the ID are required to have $p_T > 500$ MeV, and
 859 within the ID range $|\eta| < 2.5$. Additional criteria such as primary vertex are required to
 860 ensure selected tracks originating from the collision and prevent the mis-reconstructed
 861 tracks from pile-up hits in the detector. The alignment of tracks with calorimeter-based
 862 jets is executed through the application of the ghost-association technique. This entails
 863 a repetition of the jet clustering procedure augmented by the inclusion of 'ghost' repre-
 864 sentations of registered tracks [65]. These ghost tracks share the same direction as their
 865 actual counterparts but possess an infinitesimally small p_T , thereby ensuring that they do
 866 not induce any alterations to the intrinsic characteristics of the calorimeter-based jets. A
 867 criterion for track-jet correspondence is established: a given track is associated to a jet if
 868 its corresponding ghost track is contained in the jet after reclustering.

869 Jet reconstructed from the simulated MC is known as "truth jets" [43], with the
 870 same $R = 0.4$ algorithm as PFlow jets. Geometric correspondence between truth jets
 871 and PFlow jets is established via angular proximity, adhering to the criterion $\Delta R < 0.4$.
 872 Each truth jet is bestowed with a flavour label, referred to as a truth label [46, 47]. The
 873 truth flavour label attributed to a jet is defined by the flavour of the highest-energy parton
 874 situated within a cone of size $\Delta R < 0.4$ around the jet's axis, prior to the process of hadro-
 875 nisation in the parton shower. Following this definition, jets arising from the splintering
 876 of gluons into b - or c -quark pairs are labelled as heavy flavour jets. These heavy flavour
 877 jets are often identifiable by the long-lived or leptonically decaying hadrons. Therefore,
 878 no distinct discriminant tailored for heavy-flavour quarks is investigated within the cur-
 879 rent framework [66, 67]. Jets will be unlabelled if there is no corresponding truth parton
 880 with $p_T > 1$ GeV is found within the cone surrounding the truth jet. These instances of
 881 unlabelled jets commonly emerge as a consequence of pile-up effects, and less than 1%
 882 of the dataset used. They are thus ignored [68].

5.2.2 Event Selection and definition of quark and gluon-enriched samples

Events are chosen by the single-jet trigger, HLT_j420. The jet p_T is required to be greater than 500 GeV, as more quark-jets and better resolution on the jet constituents are given. Only the leading two jets with the highest p_T are used, as dijet events, and are required to be $|\eta| < 2.5$ so that their charged constituents are collected within the coverage of the ID. To maintain the equilibrium in p_T and suppress non-isolated jets, a criterion demands that the ratio of the p_T of the leading jet to that of the sub-leading jet remains within 1.5. The two leading p_T jets serve as the cornerstone for the formulation of quark-enriched and gluon-enriched subsamples.

The quark-enriched sample is derived from the jet with higher $|\eta|$ among the leading two jets, while the gluon-enriched sample is extracted from the jet with lower $|\eta|$. This selection strategy capitalizes on the intrinsic behaviour of PDFs at higher proton momentum fraction range, where there exists a higher likelihood of encompassing valence quark-jets. Consequently, jets situated in more forward regions (higher $|\eta|$) have a higher probability of being quark-jets, while jets positioned closer to the central region (lower $|\eta|$) manifest an increased likelihood of corresponding to gluon-jets [69].

Selection	Multi-jet sample
Trigger	HLT_j420
Number of jets	≥ 2
$p_T(j_1)$	> 500
$p_T(j_2)$	> 500
$p_T(j_1)/p_T(j_2)$	< 1.5
$ \eta(j_1) $	< 2.1
$ \eta(j_2) $	< 2.1
Target parton	Quark(Higher $ \eta $) or Gluon (Lower $ \eta $)

Table 5.2 The selections to retrieve quark/gluon-enriched samples. " j_i " represents the i -th jet in p_T -ordering.

The distribution of leading and subleading jets p_T in dijet event after selections is shown in Figure 5.14 for both MC and data.

5.3 Quark/gluon tagging variables

According to QCD, the colour factor of gluons is larger than that of quarks by factor 9/4 ("Casimir ratio") [45], which makes gluons emit more particles in the hadronisation

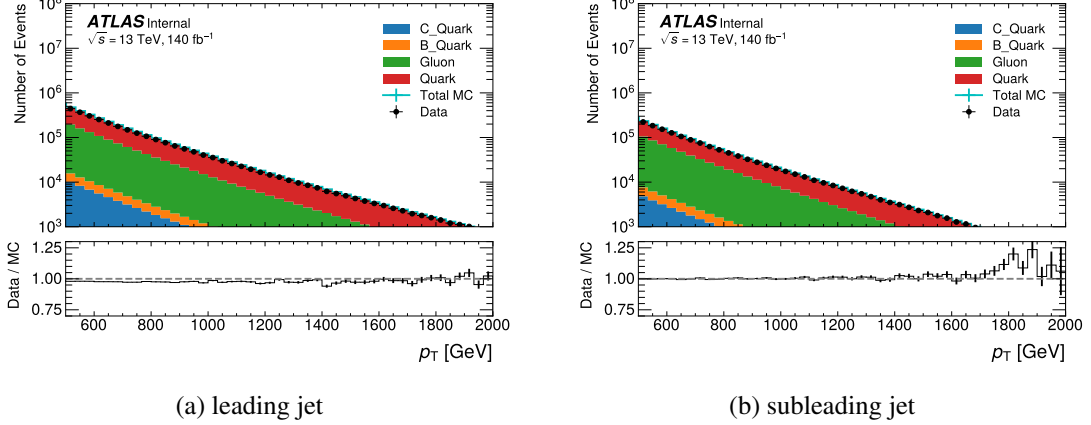


Figure 5.14 The p_T distribution of the leading jets and sub-leading jets with PYTHIA samples for dijet event.

than quarks. As a result, a gluon-initiated jet has more charged multiplicity associated and its width is larger than that of a quark-initiated jet. Therefore, the information of the track multiplicity inside a jet is crucial to distinguish quarks from gluons.

The q/g tagging variables used in this study are based on the track multiplicity and are specified as : number of tracks (N_{trk}), jet width (W_{trk}) [46, 70], and two point energy correlation function ($C_1^{\beta=0.2}$) [71, 72] computed from the associated tracks. The expressions are defined as follows:

$$N_{\text{trk}}$$

N_{trk} is a number of tracks associated with the jet.

$$N_{\text{trk}} = \sum_{\text{trk} \in \text{jet}} \quad (5.1)$$

$$W_{\text{trk}}$$

W_{trk} is a track- p_T -weighted width of the jet divided by the scalar sum of track transverse momenta. It is defined as

$$W_{\text{trk}} = \frac{\sum_{\text{trk} \in \text{jet}} p_{T,\text{trk}} \Delta R_{\text{trk},\text{jet}}}{\sum_{\text{trk} \in \text{jet}} p_{T,\text{trk}}}, \quad (5.2)$$

where $p_{T,\text{trk}}$ is a p_T of a charged track reconstructed by the ID and $\Delta R_{\text{trk},\text{jet}}$ is a distance in the $\eta - \phi$ plane between the track and the jet axis.

$$C_1^{\beta=0.2}$$

Two point energy correlation function is defined as

$$C_1^{\beta=0.2} = \frac{\sum_{i,j \in jet}^{i \neq j} p_{T,i} p_{T,j} (\Delta R_{i,j})^{\beta=0.2}}{\left(\sum_{trk \in jet} p_{T,trk} \right)^2}, \quad (5.3)$$

where i and j denote tracks associated with the jet and the sum runs over all the combination of two tracks. The β is fixed to 0.2, which is known to be suitable for q/g tagging.

5.3.1 The BDT tagger

Multivariate Analysis (MVA) is a technique introduced to discriminate signal from background, one type of classification algorithm in MVA is the BDT. A tree structure is built to classify datasets through a sequence of branching binary decisions. Data with desirable features is kept by discriminating algorithm whereas others are rejected. Each decision point made construct a node at each level of the decision tree, and a score is assigned to every classifier that goes into the boosting process based on its error rate. One decision node can have two or more branches to split the datasets. Such procedure is iterated from top to down so that a termination condition such as the minimum number of samples in a node or a maximum depth in a tree depth is met. A diagram of a single decision tree is shown in Figure 5.15. After all series of cuts are applied, the BDT is defined. Therefore, a cut based on the BDT score can be employed as the most correct classification of datasets.

The BDT tagger is constructed by the combination of tracking-related observables: N_{trk} , W_{trk} , $C_1^{\beta=0.2}$ and p_T of a jet are included as the distribution of the track multiplicity is affected by them. In this study, the BDT score is used to classify quark- or gluon-jets from the multi jet samples, with the truth-labelled information from MC to train until a quark signal efficiency larger than 90% is reached.

The BDT tagger is trained using the LGBMClassifier from lightGBM [73] framework, and hyper-parameter tuning is performed with Optuna [74]. The MC PYTHIA samples are employed.

An individual score is allocated to each BDT within the boosting procedure, factoring in its error rate. This BDT score serves as the criterion for classifying a given jet as either a quark-jet or a gluon-jet.

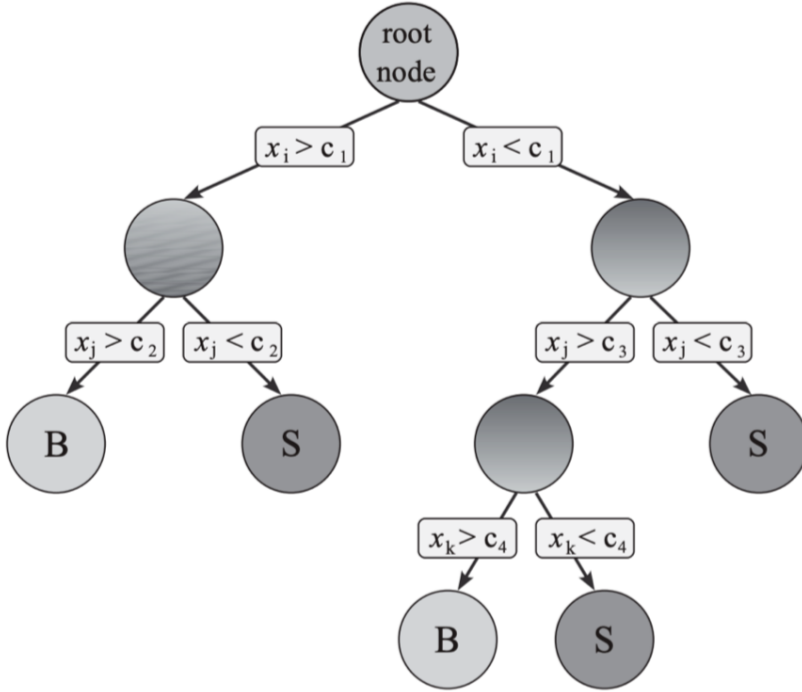


Figure 5.15 A scheme of a single decision tree with a depth of three

5.3.1.1 Feature selections

Drawing upon the features employed during the training process, an exploration of the correlation matrix is undertaken to assess the interdependence among jet attributes, including p_T , $|\eta|$, and jet substructure variables N_{trk} , W_{trk} , $C_1^{\beta=0.2}$, and the BDT. Figure 5.16 shows N_{trk} , W_{trk} and $C_1^{\beta=0.2}$ exhibit notable interrelationships among themselves, displaying relatively robust correlations. In contrast, p_T and η display a diminished level of correlation. The distributions of all single jet substructure variables and BDT score with systematic uncertainty in forward and central regions are shown in Figure 5.17. The distributions of all single jet substructure variables and BDT score with systematic uncertainty of quark- and gluon-jets in different p_T ranges from the MC simulation are shown in Figure 5.18.

Rather than employing multiple BDTs for different p_T ranges, an universal BDT can be trained using events in all p_T ranges. Given the intrinsic correlation between N_{trk} and the jet p_T , a natural way to choose features is including p_T in addition to three q/g tagging variables. Concerning the remaining variable, η , two comparative scenarios are juxtaposed: one involves its inclusion, and the other pertains to its exclusion. This comparison facilitates an assessment of whether or not to incorporate $|\eta|$.

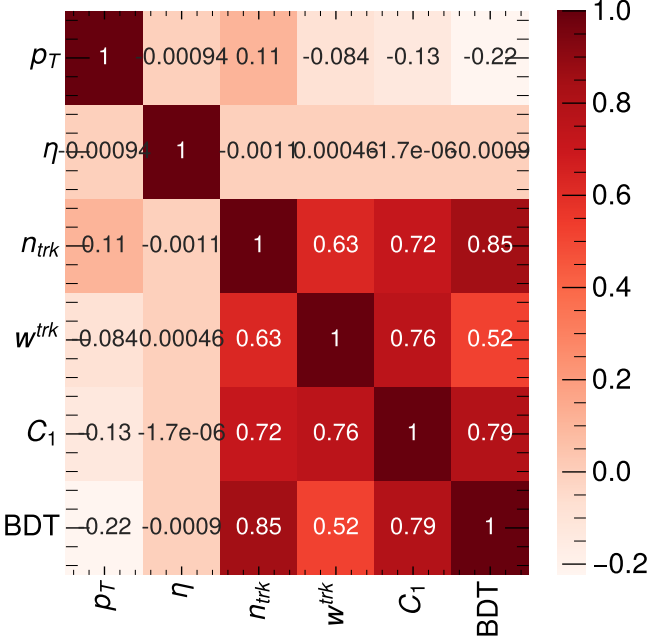


Figure 5.16 correlation matrix of jet variables.

- 964 1. p_T , N_{trk} , W_{trk} and $C_1^{\beta=0.2}$
 965 2. p_T , $|\eta|$, N_{trk} , W_{trk} and $C_1^{\beta=0.2}$

966 The result depicted in Figure 5.19 shows a distinct discrepancy when $|\eta|$ is encom-
 967 passed within the training. This violates the assumptions that the partons distribution in
 968 more forward and more central regions should not change. Specifically, the distribution
 969 of BDT scores for forward quarks substantially diverges from that of central quarks, a
 970 trend that is similarly observed for gluons. Moreover, adopting the BDT tagger that in-
 971 corporates $|\eta|$ would result in inadequate performance for jets situated within the central
 972 region when this tagger is applied to a pure sample of quark-jets (e.g., $Z+jet$ samples).
 973 In the present analysis, the BDT is endowed with the spectra of p_T , N_{trk} , W_{trk} , and $C_1^{\beta=0.2}$,
 974 as exemplified in scenario 1. At detector-level, however, the observed radiation pattern
 975 within jets no longer remains unaffected by $|\eta|$, owing to variances in the detector ma-
 976 terial and technology. To counteract this effect, a subsequent re-weighting procedure is
 977 implemented, described in Section 5.5.

978 **5.3.1.2 Training weights**

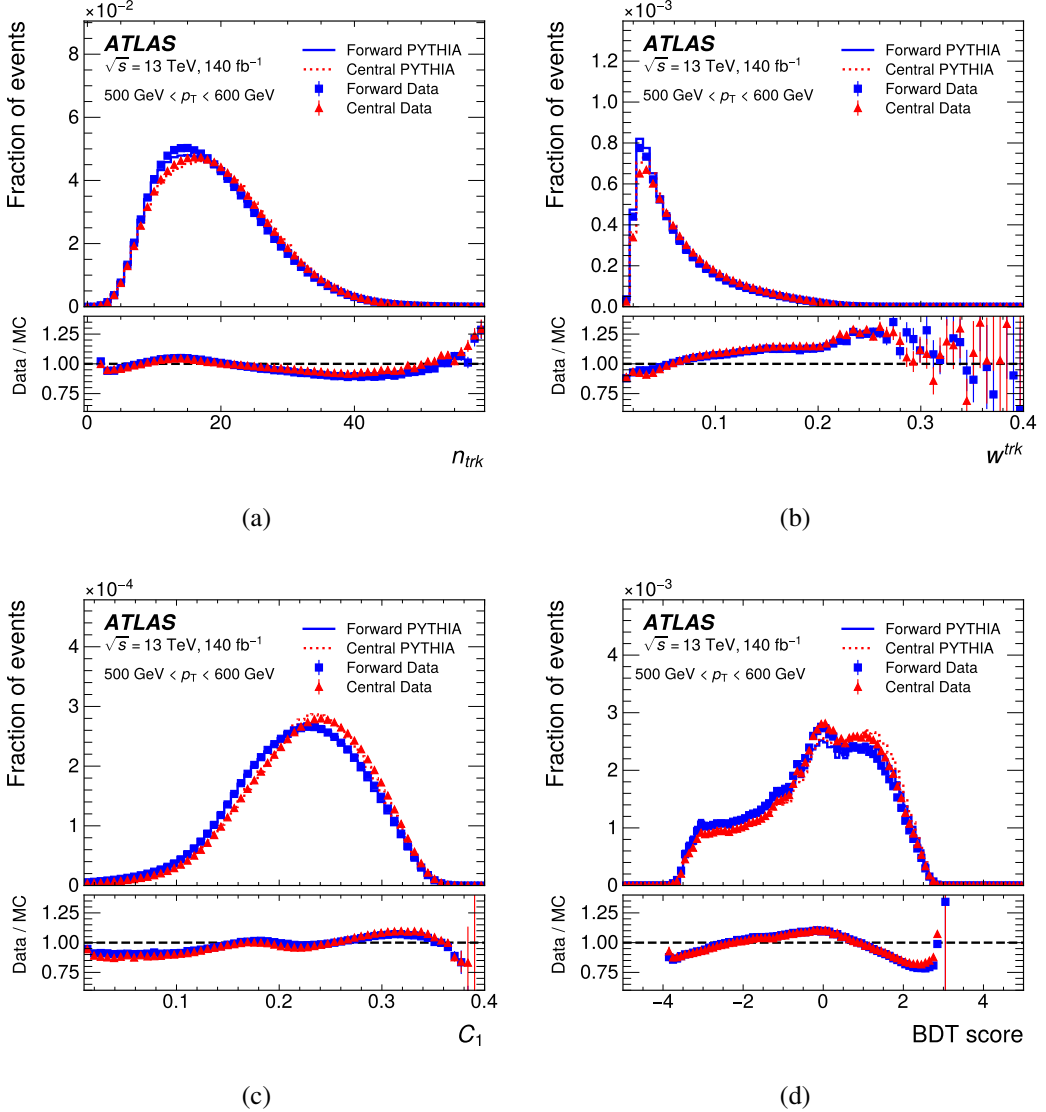


Figure 5.17 The distributions of N_{trk} (a), W_{trk} (b), C_1 (c) and BDT score (d) in the forward and central regions in data (closed symbols) and the PYTHIA MC (lines) are shown in the upper panels. The bottom panels show the ratio of the data and the MC. The distributions shown are for jet p_T in the range between 500 GeV and 600 GeV. The vertical error bars show the statistical uncertainty.

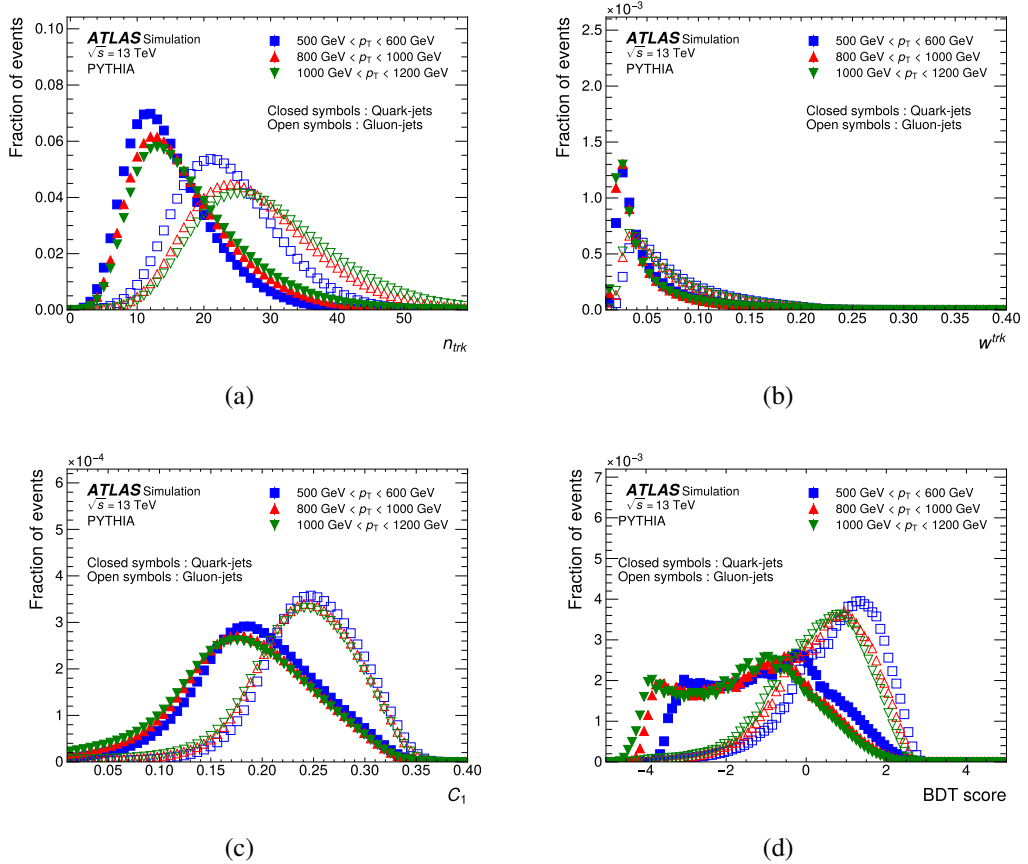


Figure 5.18 The distributions of N_{trk} (a), W_{trk} (b), C_1 (c) and BDT score (d) in the quark-jets (closed symbols) and gluon-jets (open symbols) in given p_T regions using the PYTHIA MC samples.

The calibration of quark/gluon jets taggers

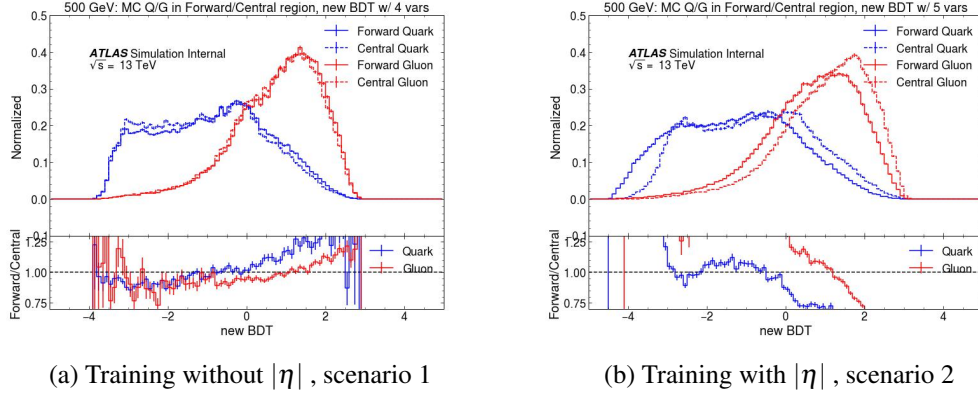


Figure 5.19 The comparison of BDT distribution for different scenarios in the jet p_T range from 500 to 600 GeV.

An additional data processing step is conducted to modify the event weights, such
 that a flat distribution of the p_T spectrum is given. This adjustment is motivated by the
 observation that higher p_T jets have less probability to occur, so the training on the higher
 p_T jets need to be emphasise. This newly introduced weight, referred to as the "flat p_T -
 weight" within this context, is exclusively employed during the training process. Con-
 versely, for other scenarios, such as assessing tagger performance on validation datasets
 and subsequent calibration endeavours, the original event weights based on physical con-
 siderations remain employed.

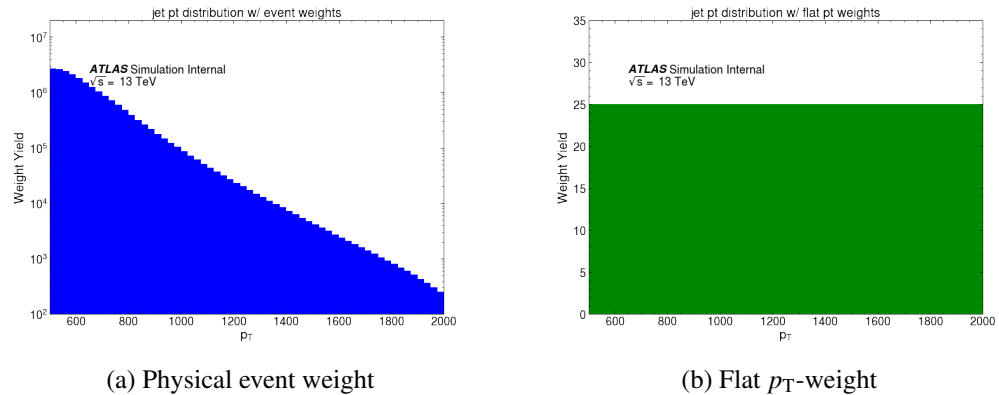


Figure 5.20 The comparison of jet p_T distributions with different weights.

987 5.3.1.3 Training Configuration

988 Approximately 30% of the data from each period of the MC PYTHIA 8 A, D, E is
 989 randomly allocated for the training investigation, constituting an aggregate of roughly 60
 990 million jets. The dataset division for training, validation, and testing is structured in a
 991 ratio of 80% for training, 10% for validation, and 10% for testing.

992 Optuna is employed to conduct a search for optimal hyperparameters. Following the
 993 hyperparameter tuning process, the most optimal model is achieved after 100 iterations
 994 of such procedure. The optimised parameters are listed:

- 995 • bagging_fraction 0.9176347488279626
- 996 • bagging_freq 2
- 997 • feature_fraction 0.9084973008559477
- 998 • lambda_11 0.0016400096502256838
- 999 • lambda_10 0.006327330258011633
- 1000 • min_child_samples 13
- 1001 • num_leaves 224

1002 The performance of a classification model at all classification criteria can be illus-
 1003 trated using a receiver operating characteristic (ROC) curve. The idea is to compare
 1004 the true positive rate (TPR, also known as sensitivity, recall or probability of detection)
 1005 against the false positive rate (FPR, also known as the probability of false alarm) at dif-
 1006 ferent criteria given. Consider a binary classification case, where the outputs are either
 1007 labelled as positive (p) or negative (n), in total there are four possible outputs from a two-
 1008 class prediction problem. A true positive (TP) is given if the output from a prediction is
 1009 p and the actual value is also p, otherwise a false positive (FP) is assigned if the actual
 1010 value is n. Conversely, a true negative (TN) is given if both the prediction outcome and
 1011 the actual value are n, whereas a false negative (FN) is assigned if the actual value is p.
 1012 TPR as a synonym for recall is defined as:

$$TPR = TP / (TP + FN) \quad (5.4)$$

1013 while the FPR is defined as:

$$FPR = FP / (FP + TN) \quad (5.5)$$

1014 In this analysis, the prediction true is defined by higher $|\eta|$ jet and prediction neg-
 1015 ative is defined by lower $|\eta|$ jet. The actual truth value is given by the quark jet from
 1016 the MC truth information, whereas the actual negative value is given by the gluon truth
 1017 information. Thus the quark efficiency is the TPR and the gluon rejection is FPR. An
 1018 Area Under the ROC Curve (AUC) is used to evaluate the performance of a classifier,
 1019 the better performance is indicated by higher AUC values.

1020 Several ROC plots are made to compare different features and the BDT in different
 1021 p_T ranges. To check whether the BDT tagger is overtrained, the shape comparison is
 1022 shown in Figure 5.21, between training dataset and validation dataset. No overtraining
 1023 is observed as the distribution of training dataset is very similar to that of testing dataset.

1024 Figure 5.22 shows the ROC curve for all single jet variables and the BDT-tagger
 1025 in given p_T ranges in forward and central regions. Figure 5.23 shows the AUC of both
 N_{trk} -only tagger and the BDT-tagger as a function of jet p_T .

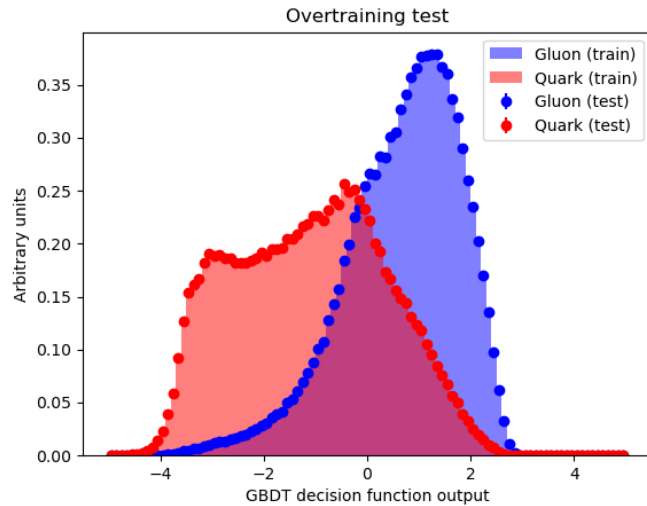
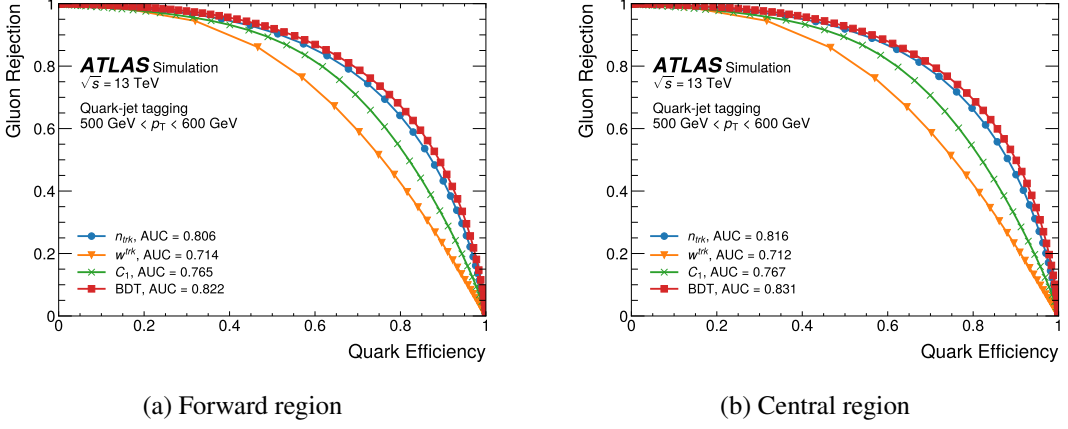
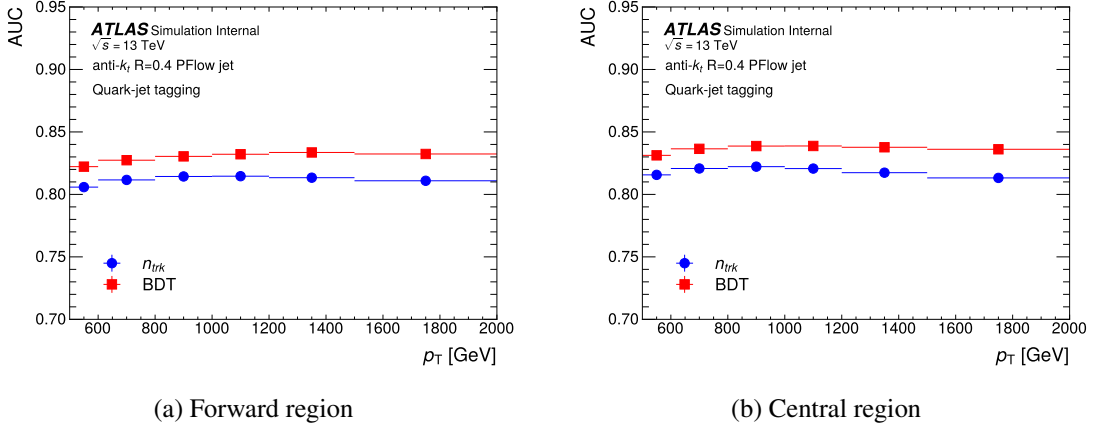


Figure 5.21 Overtraining validation

1026
 1027 The N_{trk} -only tagger is found to be the most sensitive observable than other indi-
 1028 vidual jet substructure variables for q/g tagging, W_{trk} and $C_1^{\beta=0.2}$ are less sensitive to the
 1029 number of tracks inefficiencies because they are defined as ratios, the BDT-tagger which
 1030 include the W_{trk} and $C_1^{\beta=0.2}$ has better AUC than N_{trk} -only tagger across all jet p_T ranges.
 1031 This indicates that the BDT-based tagging mechanism has a heightened capacity to dis-
 1032 criminate against gluon-jets at the same level of efficiency in identifying quark-jets with
 1033 N_{trk} -only tagger . Both taggers are calibrated in this paper, more details are presented in


 Figure 5.22 The ROC Curve for different taggers in the given jet p_T .

 Figure 5.23 The AUC for different taggers across jet p_T .

1034 the next section.

1035 **5.4 Matrix Method**

1036 The distribution of q/g tagging variables depend strongly on jet p_T . Thus a matrix
 1037 method [47] approach used to extract the shape of the q/g tagging variables is performed
 1038 on each p_T bin defined in Table 5.3 for quark- and gluon-jets, separately.

1039 To measure the performance of the q/g taggers under study, samples exclusively
 1040 composed of either quark-jets or gluon-jets are needed. In order to deduce the distribu-
 1041 tion shapes of the q/g tagging variables pertaining to quark- and gluon-jets within the
 1042 empirical data, a methodology that capitalizes on samples possessing varying q/g ratios is

p_T bin boundary [GeV]					
500-600	600-800	800-1000	1000-1200	1200-1500	1500-2000
Forward & Central $ \eta $ jet samples in multi-jet					

Table 5.3 The p_T range division for the calibration of the q/g tagging variables and samples used in extraction of pure quark and gluon jets.

employed. This approach, known as the matrix method [47], facilitates the extraction of the distinct distributions of q/g tagging variables for the aforementioned jet categories.

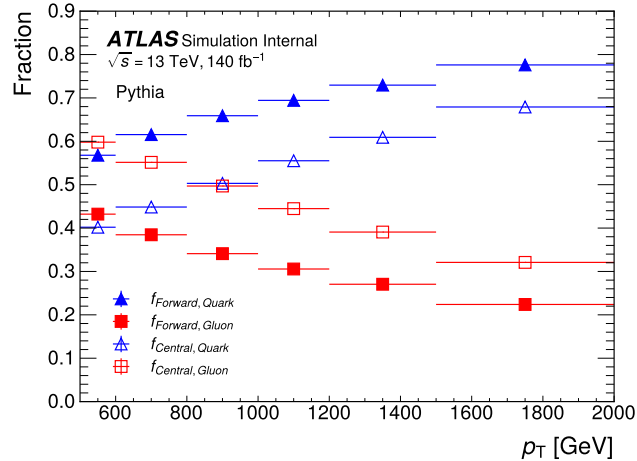
Pure quark- or gluon-jets can be extracted from forward and central jet samples following the matrix:

$$\begin{pmatrix} p_F(x) \\ p_C(x) \end{pmatrix} = \underbrace{\begin{pmatrix} f_{F,Q} & f_{F,G} \\ f_{C,Q} & f_{C,G} \end{pmatrix}}_{\equiv F} \begin{pmatrix} p_Q(x) \\ p_G(x) \end{pmatrix} \quad (5.6)$$

$$\begin{pmatrix} p_Q(x) \\ p_G(x) \end{pmatrix} = F^{-1} \begin{pmatrix} p_F(x) \\ p_C(x) \end{pmatrix}. \quad (5.7)$$

where $p_{Q,G}(x)$ represents the distributions of the q/g tagging variable x in pure quark- and gluon-enriched jet samples, $p_F(x)$ and $p_C(x)$ show the distributions of jet variables in forward and central regions, respectively, $f_{F/C,Q/G}$ are the fractions of quarks and gluons in a forward or central region. The inverse matrix of F is thus constructed and used to extract pure quark/gluon $p_{Q,G}$. Data is used to obtain the distributions of the quark- and gluon-enriched samples, MC is used to calculate the fraction of quarks and gluons in them as shown in Figure 5.24, as well as the distributions of q/g tagging variables. The matrix is calculated in each x bin and each jet p_T range.

Figure 5.25 illustrates the fraction of light and heavy quark- and gluon-jets in the PYTHIA 8 dijet sample. These fractions are depicted in a stacked format, summing up to a cumulative value of 1. It should be noted that the involvement of heavy flavour quarks constitutes a minor fraction, amounting to a few percent, and is deemed negligible for the later study. Previous investigations [ref21] have established that any discrepancies among the fractions derived from various MC event generators remain minimal. Furthermore, the shapes of distributions obtained from the MC simulations generally exhibit congruence with those observed within the data. The distributions of N_{trk} and BDT score in higher and lower jet regions are shown in Figure 5.26 and Figure 5.27 in jet p_T range



(a)

Figure 5.24 Fractions of quark-jets and gluon-jets in forward jet and central jet regions from PYTHIA dijet process. These values are used as elements in F matrix in Equation 5.6.

1064 500 GeV - 600 GeV. The shapes of distributions obtained from the MC simulations is
 1065 generally consistent with that from data.

The calibration of quark/gluon jets taggers

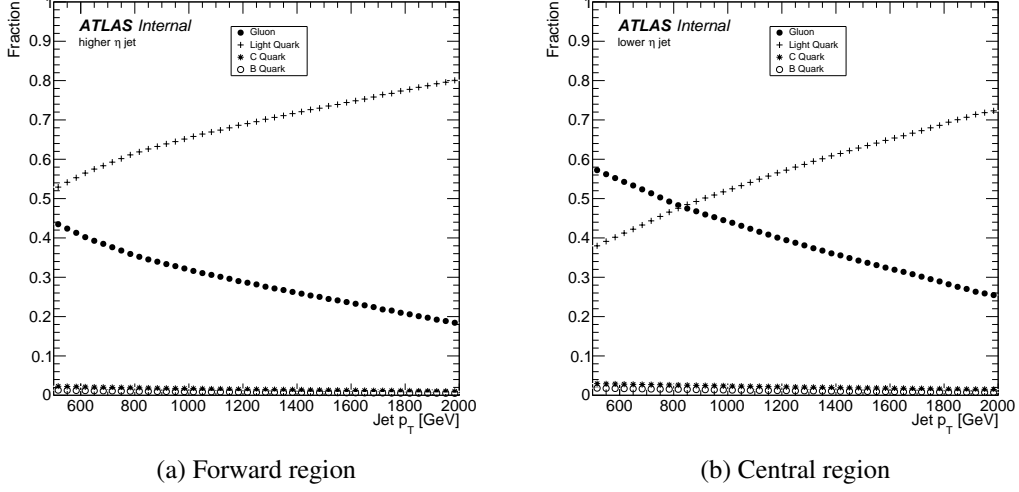


Figure 5.25 Flavor composition of forward (a) or central (b) multi-jet events.

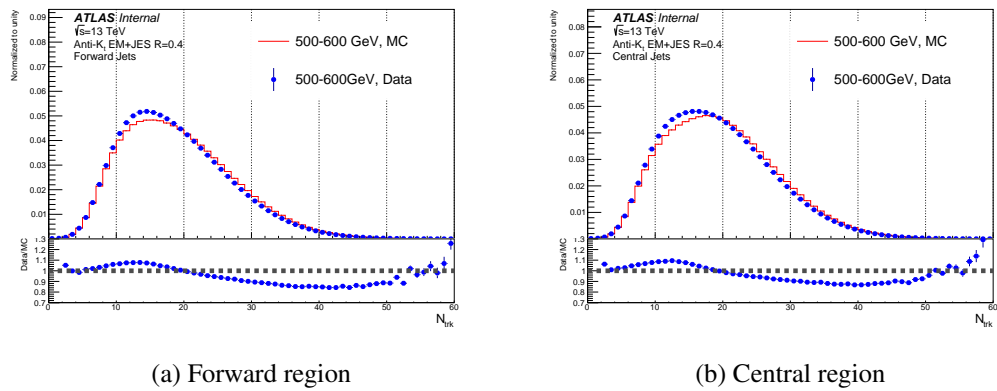


Figure 5.26 The N_{trk} distribution of the leading two jets with PYTHIA 8 in the MC and data.

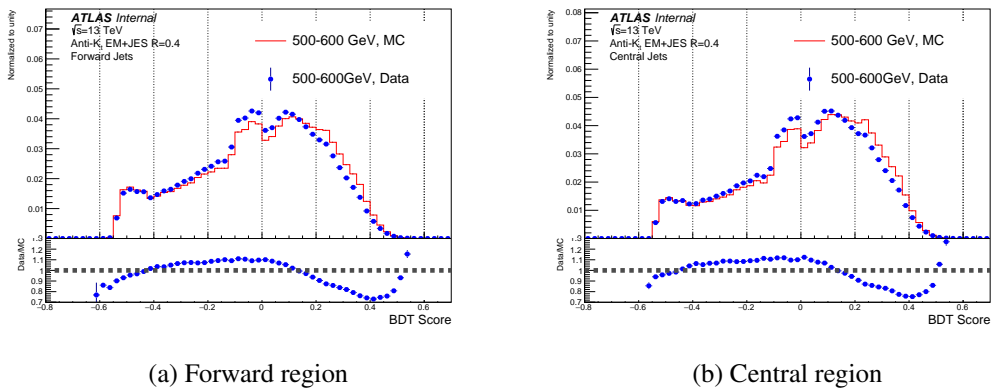


Figure 5.27 The BDT score distribution of the leading two jets with PYTHIA 8 in the MC and data.

1066 5.5 MC non-closure

1067 The matrix method is valid under the assumption that the shapes of $p_Q(x)$ and $p_G(x)$
 1068 remain consistent, regardless of whether the jets are situated in the central or forward
 1069 regions. Jet fragmentation at a pp collider is expected to be predominantly influenced
 1070 by the jet p_T and is generally considered independent of η , considering the underlying
 1071 parton type. Consequently, an approach aimed at extracting distributions associated with
 1072 the radiation patterns of quark-jets and gluon-jets should be valid at the particle level. At
 1073 the detector level, however, the measured radiation pattern within jets no longer retains its
 1074 η -independence. This is due to variations arising from differences in detector materials
 1075 and technologies, leading to distinctions between the central and forward regions in terms
 1076 of response. As a consequence of these effects, the matrix method experiences deviations
 1077 from closure, indicating a disparity between the expected and actual outcomes.

1078 The distributions of N_{trk} have been seen to have systematic difference for the truth-
 1079 labelled quark/gluon jets in the quark-enriched and gluon-enriched regions in each p_T bin.
 1080 To rectify this discrepancy and ensure alignment in the distribution of jet tagging vari-
 1081 ables between the central and forward regions, a re-weighting procedure is implemented.
 1082 This procedure involves applying adjustments to account for the observed differences.
 1083 For each event, the central jet is weighted by a re-weighting factor :

$$w_{Q/G}(x; p_{T,j}) = \frac{p_{Q/G, \text{forward}}(x; p_{T,j})}{p_{Q/G, \text{central}}(x; p_{T,j})} \quad (5.8)$$

1084 where q/g tagging variable x is calculated in each jet p_T bin for quark and gluon jets,
 1085 respectively. By default the re-weighting factor derived from truth-labelled quark-jets is
 1086 implemented for both types of jets, whereas the re-weighting factor derived from truth-
 1087 labelled gluon-jets is used as an alternative to evaluate the systematic uncertainty from
 1088 the re-weighting procedure, known as MC non-closure systematic uncertainty for the
 1089 calibration.

1090 The distributions of N_{trk} in extracted pure quark- and gluon-jets and truth-labelled
 1091 MC before re-weighting as shown in Figure 5.28. After the re-weighting the distributions
 1092 of N_{trk} are shown in Figure 5.29. The non-closure is at few percent level and is taken
 1093 as MC non-closure systematic uncertainty.

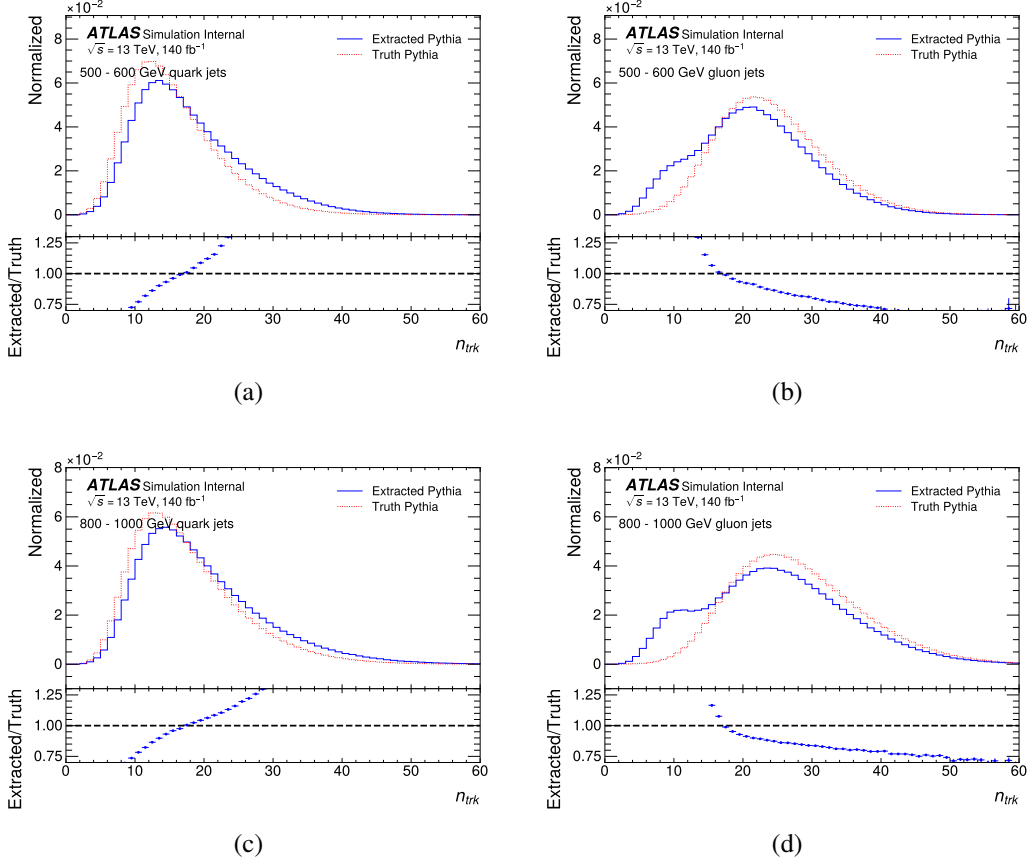


Figure 5.28 Before re-weighting: the N_{trk} distributions of quark-jet (a) (c) and gluon-jet in (b) (d) from PYTHIA 8 sample. Dashed and solid-line show the N_{trk} distributions in the truth MC and extracted MC, respectively. Bottom panels show the ratio of the extracted MC to the truth MC.

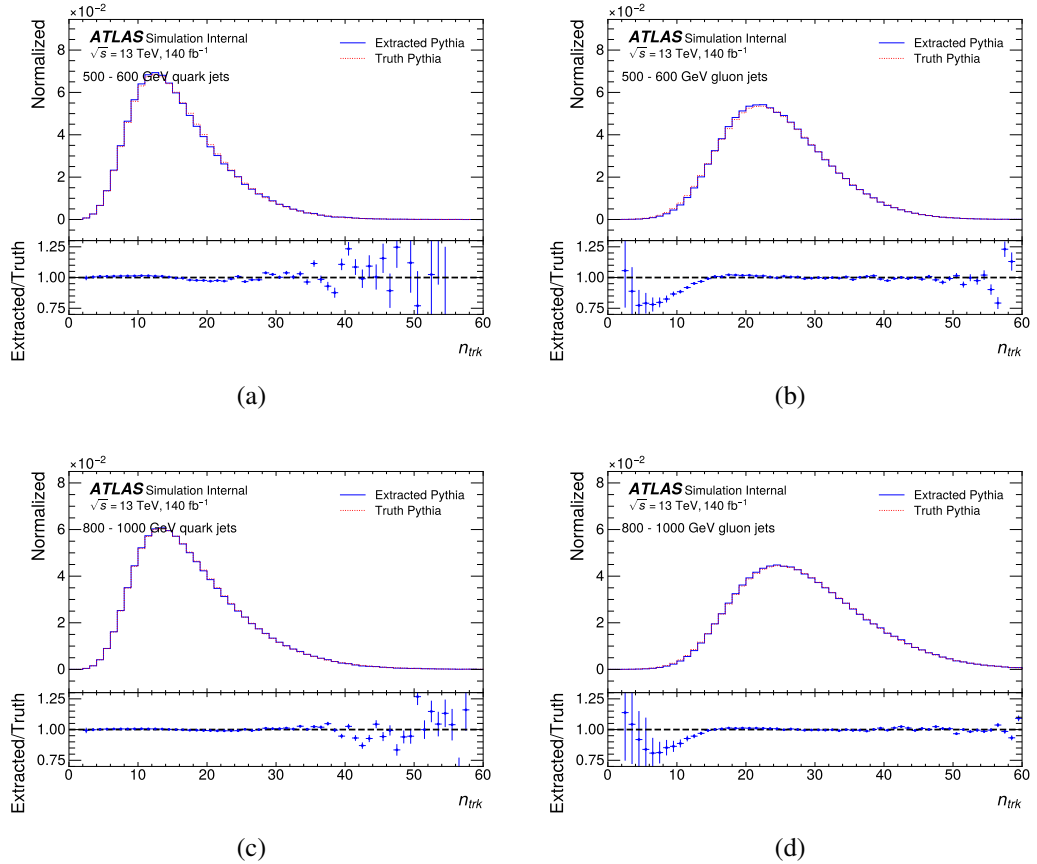


Figure 5.29 After re-weighting with quark factor: the N_{trk} distributions of quark-jet (a) (c) and gluon-jet in (b) (d) from PYTHIA 8 sample. Dashed and solid-line show the N_{trk} distributions in the truth MC and extracted MC, respectively. Bottom panels show the ratio of the extracted MC to the truth MC.

1094 **5.5.1 Closure test for BDT tagger**

1095 Similar to the distribution of N_{trk} , the distributions of BDT score for truth labelled-
 1096 jets exhibit systematic disparities in forward and central regions. Therefore, the same
 1097 re-weighting procedure as described is performed for BDT tagger as well. The MC non-
 1098 closure test is thus conducted by comparing the distributions of BDT score for extracted
 1099 and truth quark- and gluon-jets, separately, as shown in Figure 5.30. The distributions
 1100 of BDT before and after re-weighting are shown in Figure 5.31 and Figure 5.32. The
 1101 non-closure is about few percent level and taken as one systematic uncertainty.

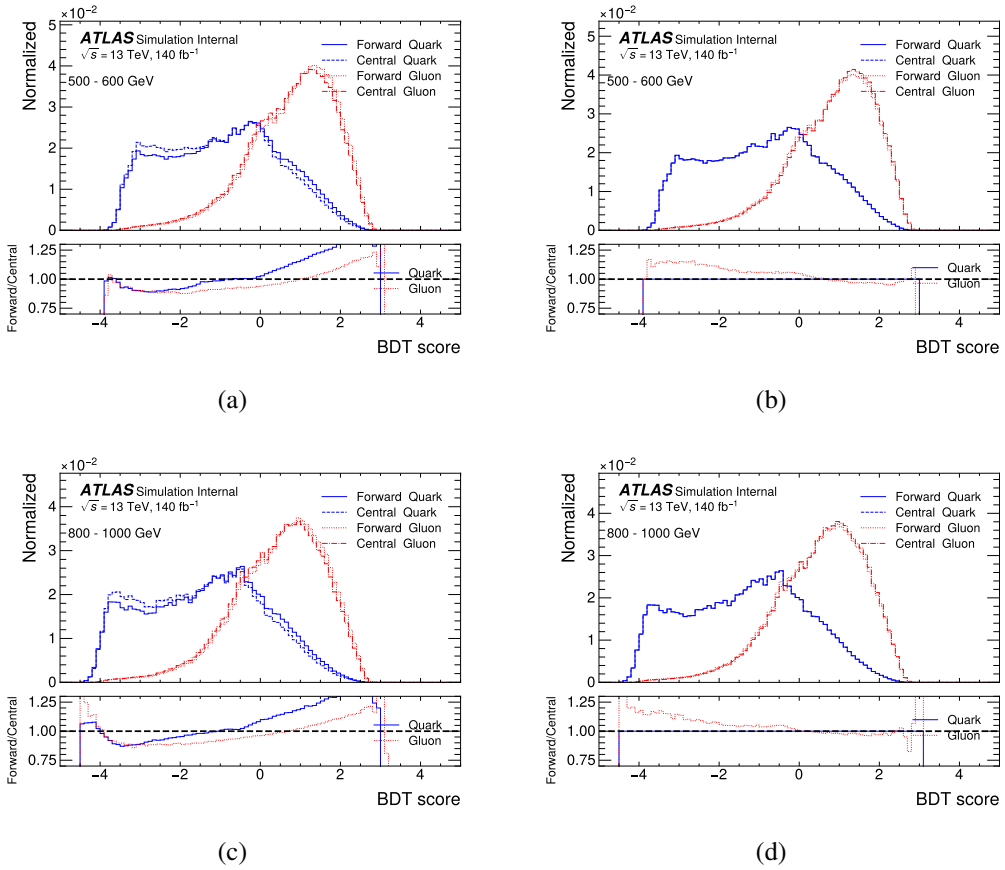


Figure 5.30 The distribution of BDT score for jets before (a) (c) and after (b) (d) re-weighting.

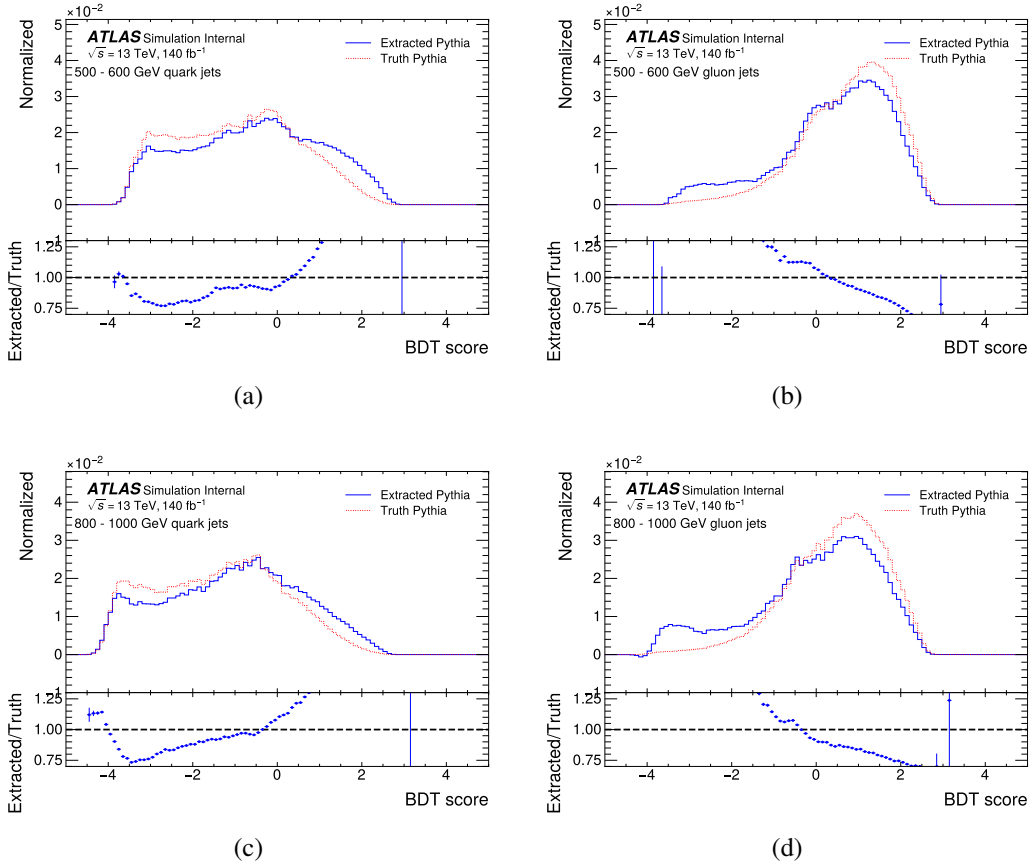


Figure 5.31 Before re-weighting: the MC-closure for quark-jet in (a) (c) and for gluon-jet in (b) (d) in BDT distributions from PYTHIA 8 sample. Dashed and solid-line histograms show the BDT distributions in the truth MC and extracted MC, respectively. Bottom panels show the ratio of the extracted MC to the truth MC.

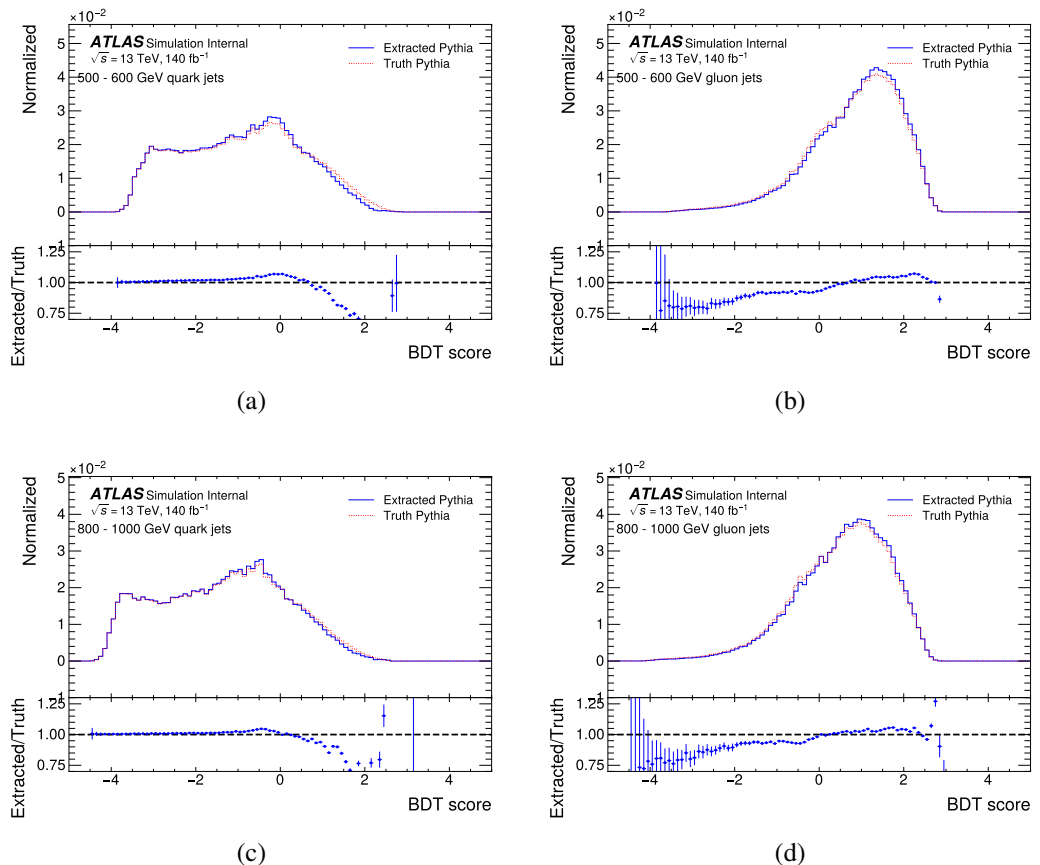


Figure 5.32 After re-weighting: the MC-closure for quark-jet in (a) (c) and for gluon-jet in (b) (d) in BDT distributions from PYTHIA 8 sample. Dashed and solid-line histograms show the BDT distributions in the truth MC and extracted MC, respectively. Bottom panels show the ratio of the extracted MC to the truth MC.

5.5.2 Summary for the MC Closure test

After applied the re-weighting factor to the jet tagging variables N_{trk} and BDT, the distributions of extracted quark-and gluon-jets converge with those of truth jets. The residual discrepancy, which has only few percent level to the total events is taken into account as MC non-closure systematic uncertainty. No obvious dependency on jet η is observed from the distributions of jet tagging variables.

5.6 Scale factor

The calibration of the q/g tagging variables is performed by applying binned scale factor (SF) in the simulation for each quark- and gluon-jet, respectively. The scale factor is obtained from distributions of the variables in quark- and gluon-jets from MC in order to match the shape of the simulation to that of the data.

The tagger working points (WP) are established for fixed quark-jets efficiency in the nominal MC sample, for both taggers. At a given working point, the efficiencies for quark- and gluon-jets are defined as follows:

$$\epsilon_{Q/G}(x^{WP}) = \int_{x < x^{WP}} p_{Q/G}(x) dx. \quad (5.9)$$

Rejection factors corresponding to quark- and gluon-jets can also be given as:

$$\xi_{Q/G}(x^{WP}) = 1 / \int_{x > x^{WP}} p_{Q/G}(x) dx = 1 / (1 - \epsilon_{Q/G}(x^{WP})). \quad (5.10)$$

Discrepancies observed between the quark-jet tagging efficiencies and gluon-jet rejections obtained from data and the corresponding values anticipated from the MC simulations are quantified using data-to-MC scale factors (SF). These factors are computed separately for each q/g tagger in various p_T bins, at a fixed WP. The SF is defined using Equation 5.9 and 5.10 for quark- and gluon-jets, respectively :

$$\text{SF}_Q(x^{WP}) = \frac{\epsilon_Q^{\text{Data}}(x^{WP})}{\epsilon_Q^{\text{MC}}(x^{WP})}. \quad (5.11)$$

$$\text{SF}_G(x^{WP}) = \frac{\xi_G^{\text{Data}}(x^{WP})}{\xi_G^{\text{MC}}(x^{WP})}. \quad (5.12)$$

1122 where $\varepsilon_{Q/G}^{\text{Data}}(x^{WP})$ and $\varepsilon_{Q/G}^{\text{MC}}(x^{WP})$ are $\varepsilon_{Q/G}(x^{WP})$ in data and MC, respectively. Same defi-
1123 nitions apply to $\xi_{Q/G}(x^{WP})$. The WPs corresponding to fixed quark-jets tagging efficien-
1124 cies of 50%, 60%, 70%, and 80% have been examined, revealing analogous trends in the
1125 characteristics of SFs.

1126 Figure 5.33 to 5.36 show the distribution of all jet tagging variables in quark- and
1127 gluon-jets after matrix method extraction in all different MC samples and data in given
1128 p_T range.

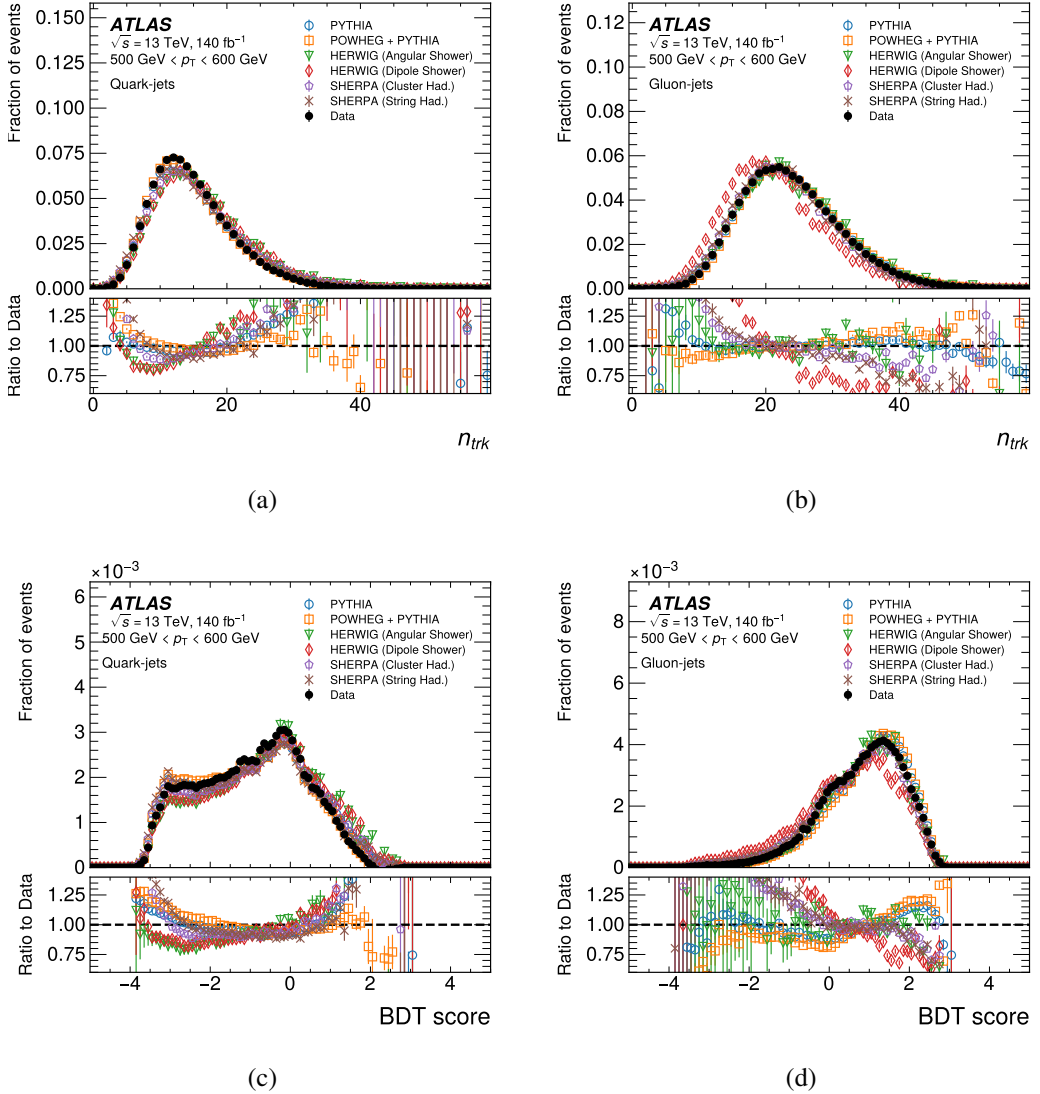


Figure 5.33 The distributions of N_{trk} (a,b) and BDT score (c,d) for quark-jets (left) and gluon-jets (right) using different generators (open symbols) and data (closed symbol) are shown in the upper panels. The lower panels show the ratio of each MC distribution and the data. The vertical error bars show the statistical uncertainty.

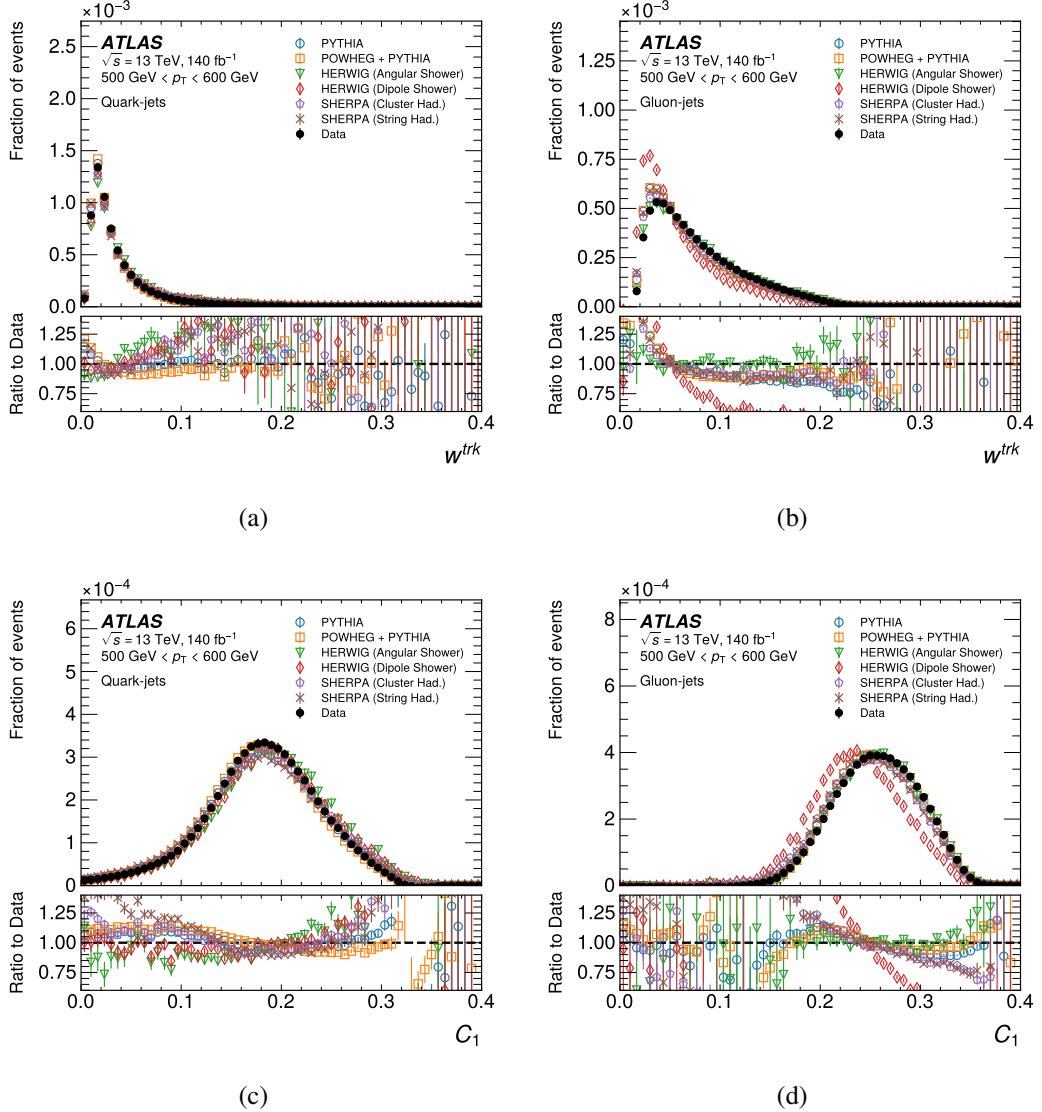


Figure 5.34 The distributions of W_{trk} (a,b) and C_1 (c,d) for quark-jets (left) and gluon-jets (right) using different generators (open symbols) and data (closed symbol) are shown in the upper panels. The lower panels show the ratio of each MC distribution and the data. The vertical error bars show the statistical uncertainty.

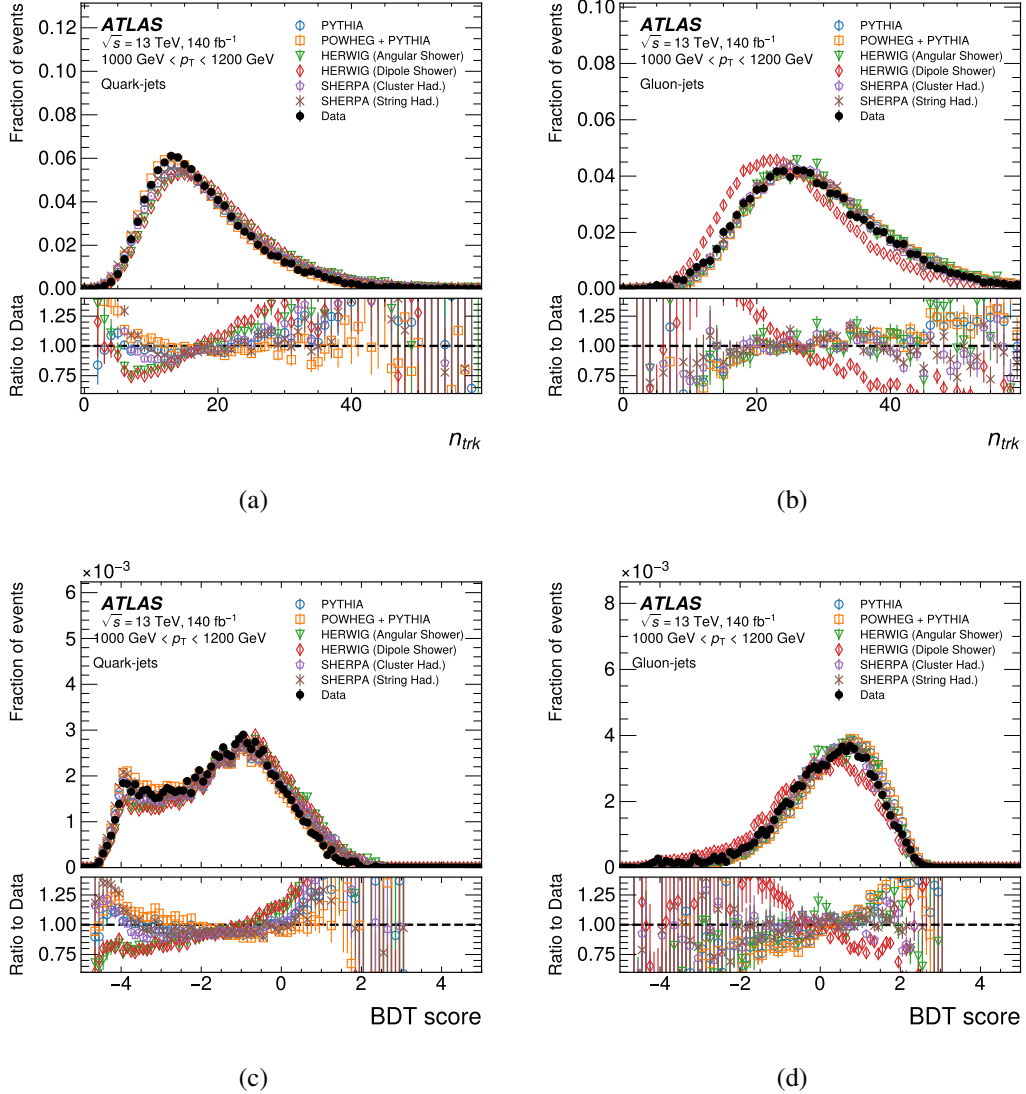


Figure 5.35 The distributions of N_{trk} (a,b) and BDT score (c,d) for quark-jets (left) and gluon-jets (right) using different generators (open symbols) and data (closed symbol) are shown in the upper panels. The lower panels show the ratio of each MC distribution and the data. The vertical error bars show the statistical uncertainty.

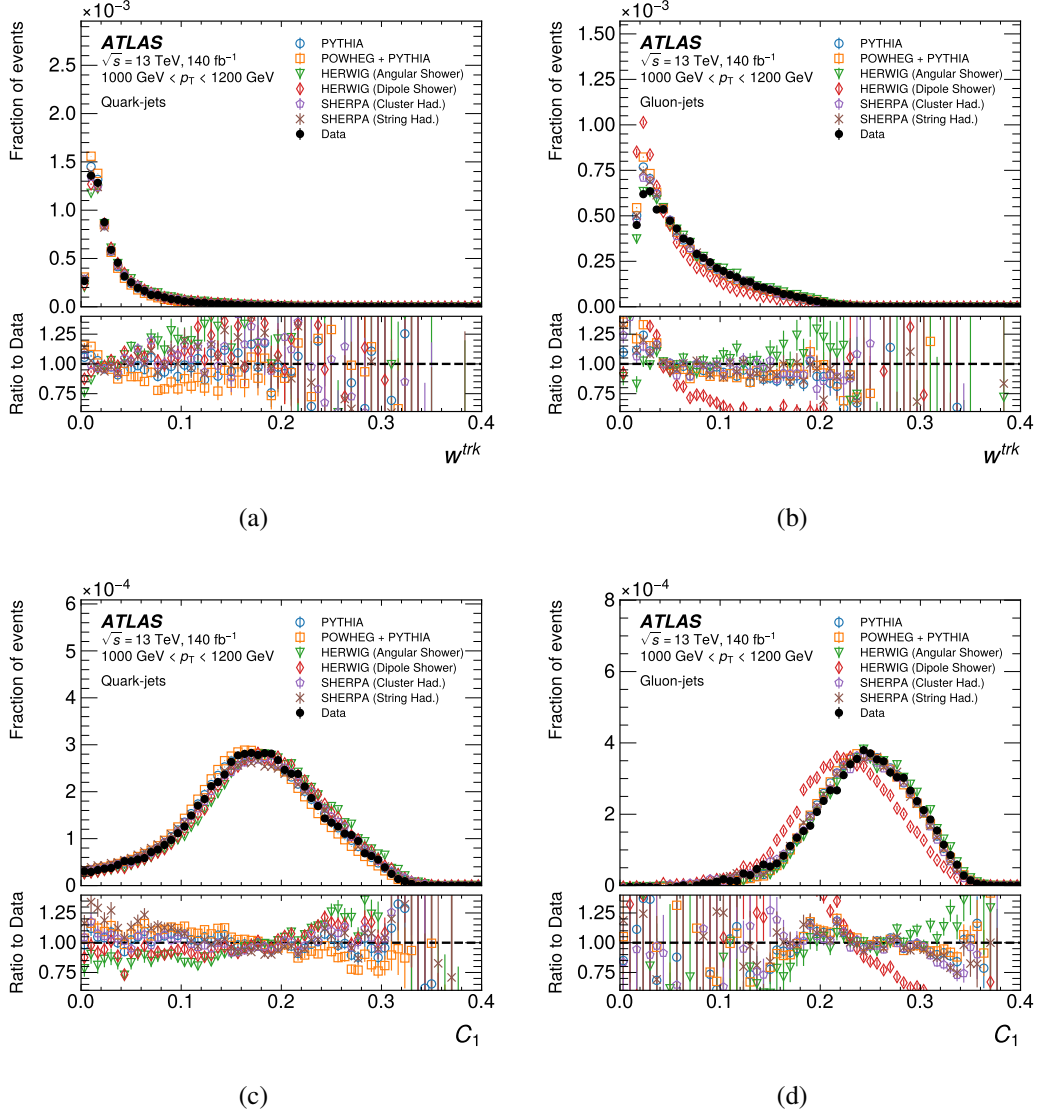


Figure 5.36 The distributions of W_{trk} (a,b) and C_1 (c,d) for quark-jets (left) and gluon-jets (right) using different generators (open symbols) and data (closed symbol) are shown in the upper panels. The lower panels show the ratio of each MC distribution and the data. The vertical error bars show the statistical uncertainty.

1129 Cut values corresponding to the 50% WP are summarised in Table 5.4 for the N_{trk} -
 1130 only tagger and Table 5.5 for the BDT-tagger. Figure 5.37 shows the gluon-jets efficiency
 1131 of both N_{trk} -only tagger and the BDT-tagger as a function of jet p_{T} , for the MC and data,
 1132 at four WPs.

1133 Both the N_{trk} -only and BDT-taggers demonstrate commendable performance on
 1134 data, with high quark signal efficiency across all p_{T} range. Notably, at the 50% work-
 1135 ing point, the N_{trk} -only tagger achieves approximately 90% rejection of gluon-jets, while
 1136 the BDT tagger surpasses this performance by rejecting around 93% of gluon-jets. The
 1137 BDT-tagger outperforms the N_{trk} -only tagger by exhibiting superior gluon-jets rejection
 1138 rates at the identical WP. This disparity in performance arises from the inclusion of a
 1139 more comprehensive set of jet substructure variables in the BDT approach. The discrep-
 1140ancy between the level of gluon-jet rejection observed in data and that predicted by the
 1141 MC samples increases as the jet p_{T} increases. This phenomenon is closely tied to the
 1142 dissimilarity between the modelling of gluons and their actual behaviour in data.

p_{T} [GeV]	500 - 600	600 - 800	800 - 1000	1000 - 1200	1200 - 1500	1500 - 2000
WP						
0.5	15.0	16.0	17.0	18.0	18.0	19.0
0.6	17.0	18.0	19.0	20.0	20.0	21.0
0.7	19.0	20.0	21.0	22.0	23.0	24.0
0.8	22.0	23.0	24.0	26.0	27.0	28.0

Table 5.4 Cut values of N_{trk} at different working point in each of jet p_{T} range

p_{T} [GeV]	500 - 600	600 - 800	800 - 1000	1000 - 1200	1200 - 1500	1500 - 2000
WP						
0.5	-0.8	-1.0	-1.2	-1.4	-1.6	-1.8
0.6	-0.4	-0.6	-0.8	-1.0	-1.2	-1.4
0.7	0.0	-0.2	-0.4	-0.6	-0.8	-1.0
0.8	0.4	0.2	0.0	-0.2	-0.3	-0.6

Table 5.5 Cut values of BDT at different working point in each of jet p_{T} range

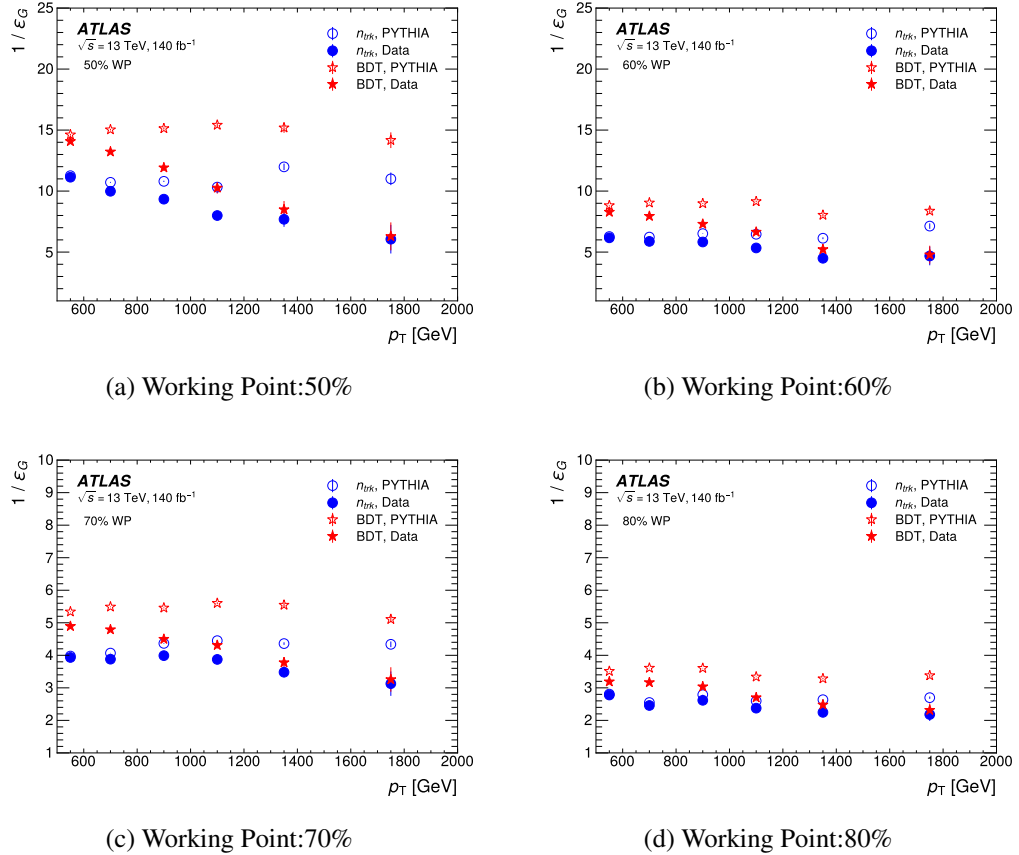


Figure 5.37 Inverse of the gluon-jet efficiency of N_{trk} (circles) and BDT (stars) as a function of jet p_T at the each WP in data (closed symbols) and the PYTHIA (open symbols) MC. The vertical error bars show the statistical uncertainty.

1143 **5.7 Systematic uncertainties**

1144 In this study, different types of systematic uncertainty are taken into account. The
1145 distribution of N_{trk} and BDT for truth-labelled quark-/gluon-jets are given by the MC
1146 simulation samples, therefore, theoretical uncertainties originate from aspects encom-
1147 passing the modelling of the MC simulation, such as choices involving parton showering,
1148 hadronisation, matrix element, PDFs, scale variations, and Splitting-Kernel effects. Fur-
1149 thermore, experimental uncertainties such as JES and JER, tracking reconstruction effi-
1150 ciencies are meticulously incorporated. The potential impact of methodological choices,
1151 including N_{trk} or BDT re-weighting, as well as the non-closure behaviour of MC simula-
1152 tions, is propagated to the resultant SFs.

1153 The nominal result in this analysis is provided using PYTHIA 8 MC samples, all
1154 other MC samples are considered as alternative samples to study corresponding system-
1155 atic uncertainty.

1156 **5.7.1 Parton shower modelling uncertainty**

1157 The different chose of algorithmic or parametric in the modelling of the parton
1158 shower could result in different SF result. This systematic uncertainty is estimated by
1159 comparing the SFs extracted from two MC samples with the same ME and hadronisation
1160 but different types of showers: HERWIG Angular-ordered and HERWIG Dipole samples.
1161 The corresponding fractions of quarks and gluons present in these two MC samples, are
1162 presented in Figure 5.38. The difference of extracted SFs between these two samples is
1163 less than 10% for quark signal efficiency and around 20% for gluon rejection efficiency.
1164 While the influence on quark scale factors is negligible, it takes on a dominant role in the
1165 context of gluon scale factors.

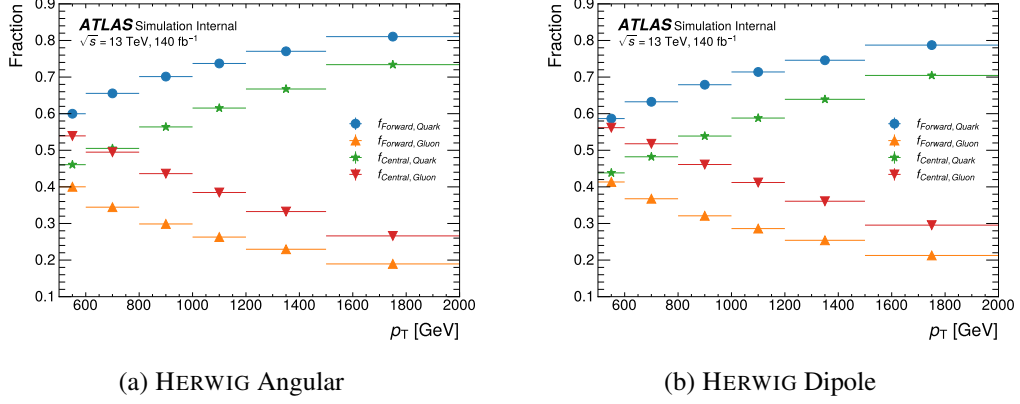


Figure 5.38 Fractions of quark- gluon-jets of HERWIG angular (a) and HERWIG dipole (b) samples.

1166 5.7.2 Hadronisation modelling uncertainty

1167 The uncertainty from hadronisation modelling is given by the difference between
 1168 the extracted SFs from the SHERPA MC samples with cluster-based hadronisation mod-
 1169 elling and string-based hadronisation modelling, separately. The corresponding fractions
 1170 of quarks and gluons present in these two MC samples are presented in Figure 5.39. The
 1171 uncertainty on the SFs range from 1% to 8% for both jet types.

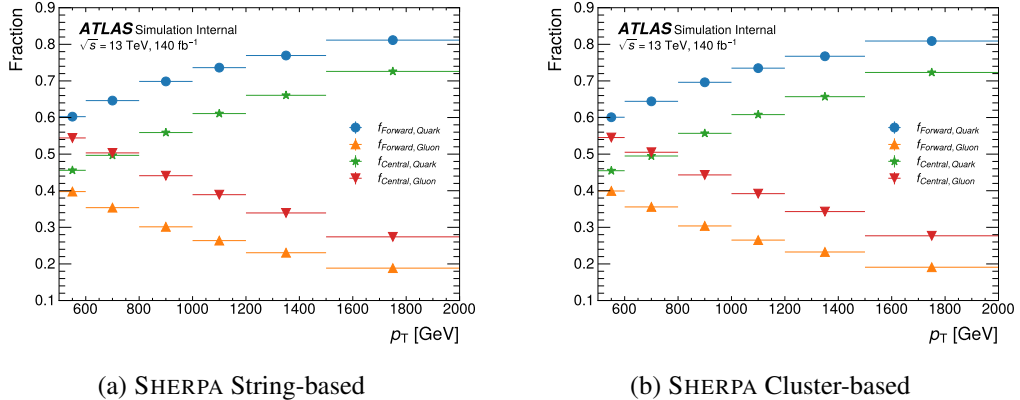


Figure 5.39 Fractions of quark- and gluon-jets in each SHERPA sample.

1172 5.7.3 Matrix element uncertainty

1173 The uncertainty introduced by different types of ME in the MC samples is taken
 1174 from the differences in the extracted SFs in two MC samples with different ME : POWHEG and
 1175 PYTHIA . The corresponding fractions of quarks and gluons present in the POWHEG sam-
 1176 ples are presented in Figure 5.40.

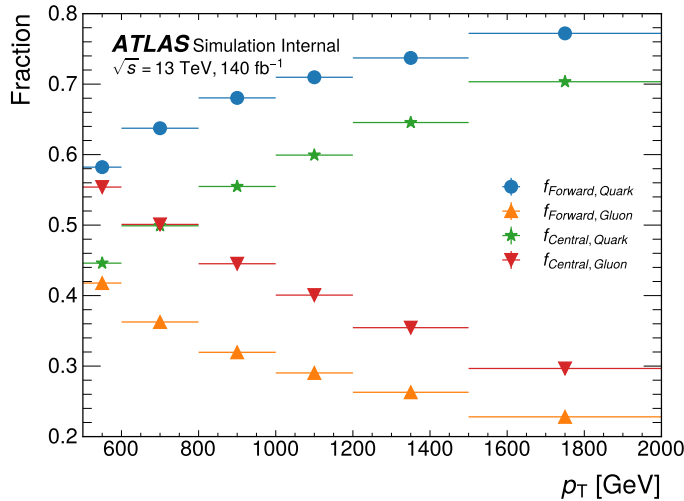


Figure 5.40 Fractions of quark jets and gluon jets in POWHEG samples.

1177 5.7.4 PDF uncertainty

1178 The uncertainty from the PDF set is evaluated using LHAPDF [75] package which
 1179 provides the PDF internal variations for each PDF set, a NNPDF2.3 set is chosen
 1180 to evaluate the various weights which depend on the momentum fraction. The PDF
 1181 uncertainty is given by changing the nominal PDF weight to the systematic variation,
 1182 then compare the SFs extracted from each of variations. The PDF uncertainty is around
 1183 5% - 7% level and almost negligible compared to others.

1184 5.7.5 Scale variation uncertainty

1185 The variation of the renormalisation (μ_R) and factorisation (μ_F) scales in QCD is
 1186 used to evaluate the uncertainty caused by missing higher order corrections. The nominal
 1187 PYTHIA sample is used for such estimation. In total there are 7 scale variations (μ_R, μ_F)
 1188 in (2,2), (2,1), (1,1), (1,2), (1,0.5), (0.5,1), (0.5,0.5) studied in this analysis. The scale

1189 uncertainty is given by taking the maximum shift of the envelope with respect to the
1190 nominal one at each working points. The total scale uncertainty is around 4% - 7%.

1191 **5.7.6 Splitting-Kernel variation uncertainty**

1192 All formulations of shower processes are constructed on the fundamental foundation
1193 of the universal behaviour exhibited by singular infrared (soft and/or collinear) lim-
1194 its within QCD. Nonetheless, when one ventures beyond these limits into the physical
1195 phase space where these kernels are employed as approximations, there are in principle
1196 infinitely many different radiation functions to choose from, sharing the same singular
1197 terms but having different non-singular ones. The Splitting-Kernel variations [76] are
1198 variations of the non singular part of the splitting functions, for initial-state radiation and
1199 final-state radiation. Such uncertainty is less than 1%.

1200 **5.7.7 Tracking uncertainty**

1201 he number of associated tracks is the most important input for both taggers, with
1202 tracking-related systematics exerting an impact on the measurement of SFs. he uncer-
1203 tainty associated with reconstructed tracks is partitioned into two components: the un-
1204 certainty pertaining to track reconstruction efficiency and the MC fake rate [64]. Both
1205 sources of uncertainty are factored in to recalibrate the count of tracks associated with
1206 jets.

1207 The track reconstruction efficiency uncertainty originates from material-related un-
1208 certainties, which constitutes the prevailing source, as well as from considerations related
1209 to the physics model. These uncertainties are estimated through a comparison of track
1210 efficiency across samples that encompass diverse detector modelling configurations. On
1211 the other hand, the MC fake rate is determined by contrasting the trends in a specific
1212 aspect of track multiplicity as a function of the average number of interactions per bunch
1213 crossing between empirical data and the MC simulation. The disparity in final SFs be-
1214 tween the nominal value and the outcome of the systematic variation contributes to the
1215 tracking systematic uncertainty. This uncertainty spans a range of approximately 1% to
1216 8%.

1217 **5.7.8 JES /JER uncertainty**

1218 The uncertainties associated with JES stem from the process of calibrating the trans-
1219 verse momentum balance between jets located in the central and forward regions, while
1220 also accommodating uncertainties linked to single-particle and test beam measurements.
1221 The JER uncertainties encompass the disparities between data and the MC. For each
1222 JES/JER variation, a corresponding SF is derived, and the difference between the nom-
1223 inal value and the variation is computed to determine the systematic uncertainty. The
1224 cumulative JES/JER uncertainty amounts to approximately 0.2%.

1225 **5.7.9 N_{trk} / BDT re-weighting**

1226 The quark-enriched and gluon-enriched regions are defined by comparing the η of
1227 leading and subleading jets, introduces to an η dependency from track reconstruction
1228 process. A re-weighting factor defined by Equation 5.8 is applied on N_{trk} and BDT
1229 taggers for each event to reduce the impact from different track multiplicity in different
1230 η range. The re-weighting factors acquired from truth-labelled gluon jets are regarded
1231 as an alternative source of contribution to the systematic uncertainty. It's worth noting
1232 that the differences arising from the re-weighting procedure remain comparatively minor
1233 (about 0.1% - 0.5%) in comparison to other sources of uncertainty.

1234 The distributions of N_{trk} and BDT for extracted quark and gluon-jets after re-weighting
1235 with quark factor have been shown in the previous chapter. The truth distribution of
1236 quark/gluon in forward/central jets using gluon factors are shown in Figure 5.41 for
1237 N_{trk} and Figure 5.42 for BDT, respectively. Figure 5.43, Figure 5.44 shows the distribu-
1238 tions of extracted quark and gluon-jets after reweighting with gluon factor.

The calibration of quark/gluon jets taggers

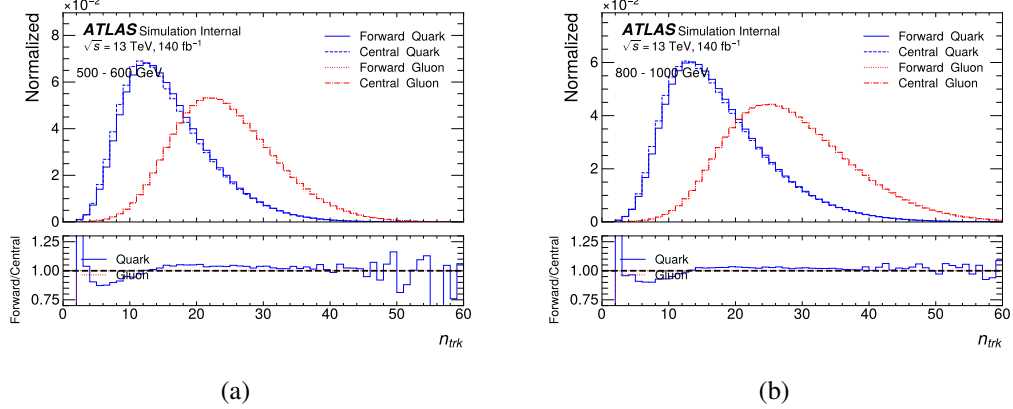


Figure 5.41 The distribution of N_{trk} for jets between 500-600 GeV (a) and 800-1000 GeV (b) after N_{trk} re-weighting using gluon factor.

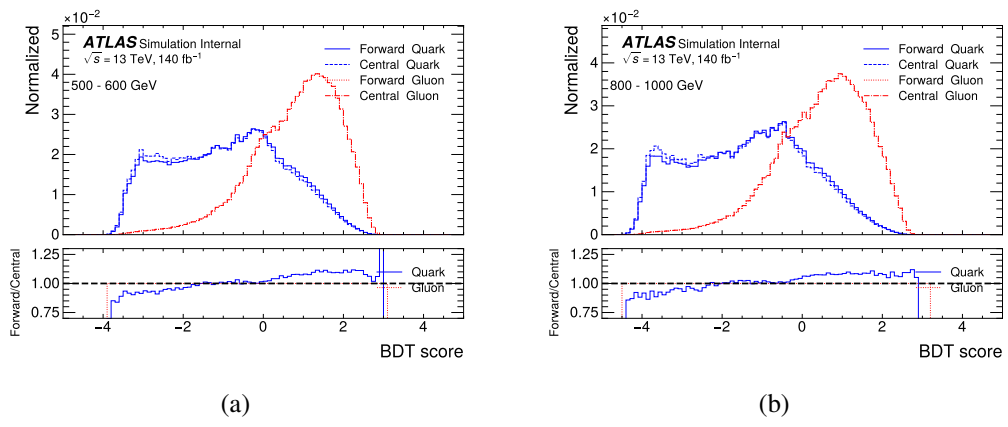


Figure 5.42 The distribution of BDT for jets between 500-600 GeV (a) and 800-1000 GeV (b) after re-weighting using gluon factor.

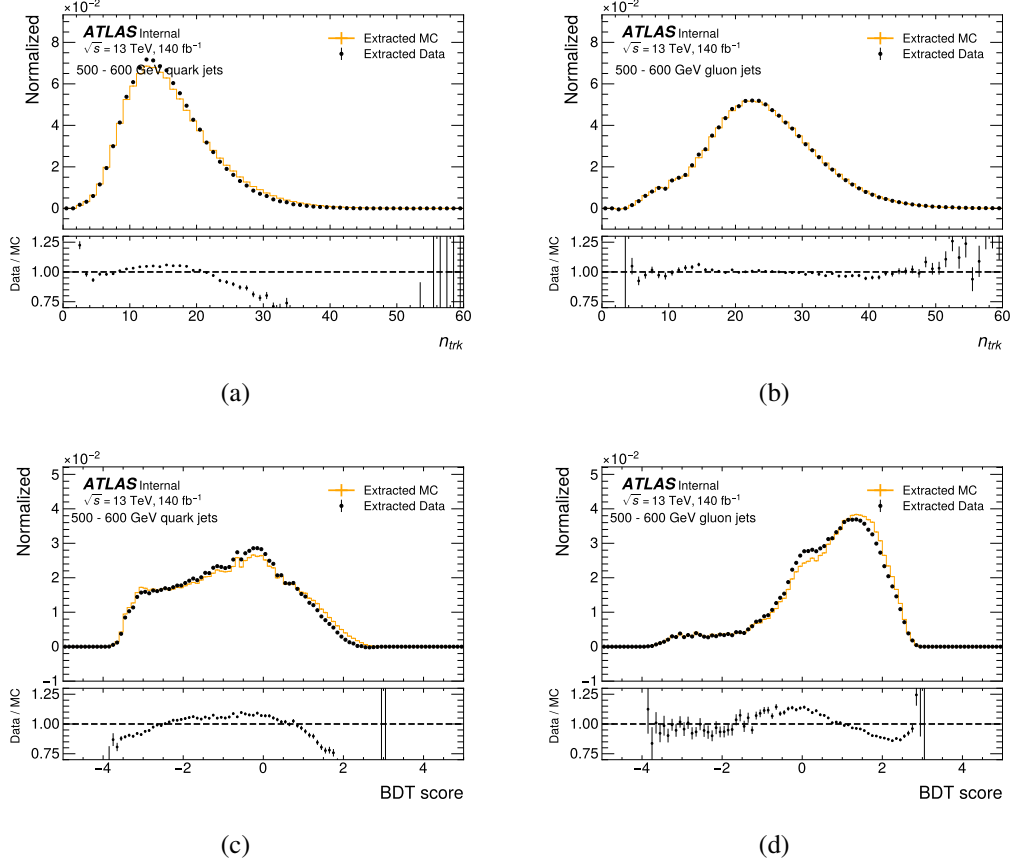


Figure 5.43 The N_{trk} (top) and BDT (bottom) distributions extracted by the matrix method from the data and MC of pure quark-jets (a) (c) and gluon-jets (b) (d) by PYTHIA 8. extracted by the matrix method from the data and MC. The gluon factor is applied. Solid-line histograms show the distributions of quark or gluon-jets defined by the jet parton flavour label in the MC. A bottom panel in each figure shows the ratio of the extracted data to the extracted MC by the matrix method.

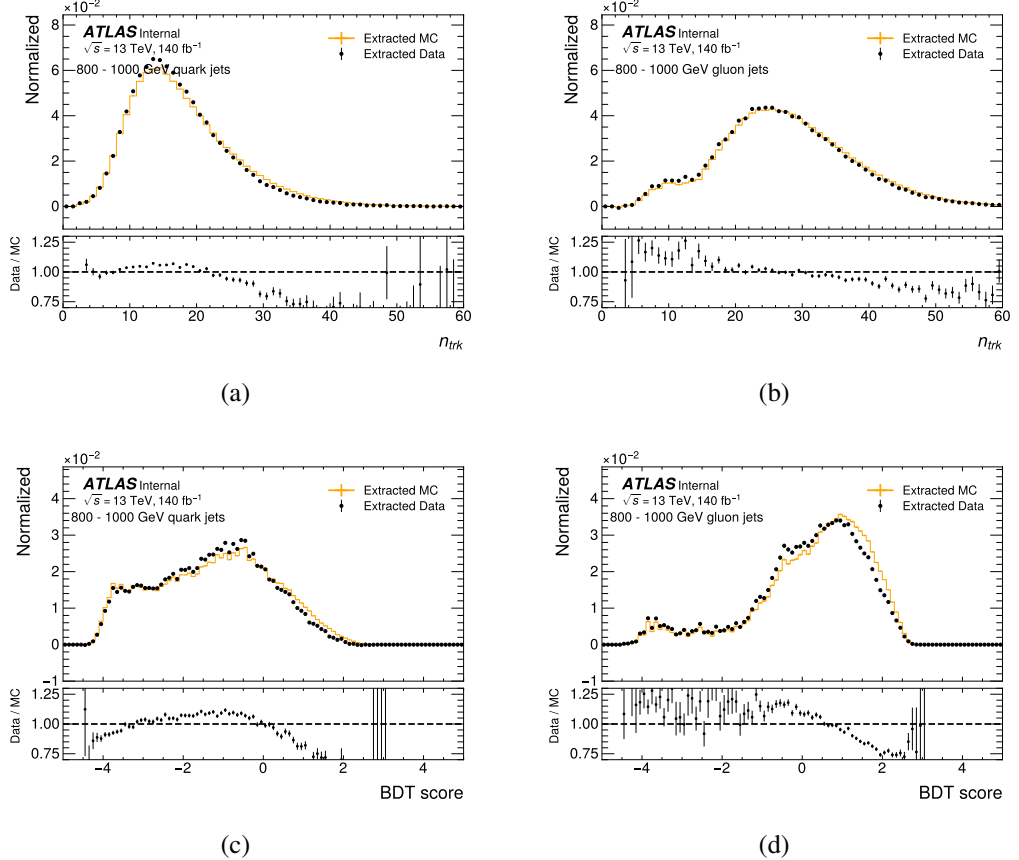


Figure 5.44 The N_{trk} (top) and BDT (bottom) distributions extracted by the matrix method from the data and MC of pure quark-jets (a) (c) and gluon-jets (b) (d) by PYTHIA 8. extracted by the matrix method from the data and MC. The gluon factor is applied. Solid-line histograms show the distributions of quark or gluon-jets defined by the jet parton flavour label in the MC. A bottom panel in each figure shows the ratio of the extracted data to the extracted MC by the matrix method.

5.7.10 The MC non-closure

As described in Section 5.5, the MC closure test is conducted using MC samples wherein each jet is assigned a truth label. After re-weighting, the distributions of N_{trk} and BDT obtained through the matrix method exhibit consistency with the truth-labelled ones for quark- and gluon-jets, respectively. The remaining difference for both taggers is only 1% level.

5.7.11 Statistical uncertainty

The estimation of statistical uncertainty involves a stepwise process. It commences by varying the input data/MC distributions bin-by-bin, using Poisson/Gaussian distributions wherein the number of data events within each bin serves as the central value. These variations of the input histograms yield templates, subsequently employed as inputs for the template variations technique. This procedure is iterated 5000 times, with the standard deviation of these uncertainties of all toys taken is used to derive the statistical uncertainty of the SFs. This uncertainty is around 0.1%.

The distributions of SFs are shown in 5.45 for N_{trk} and 5.46 for the BDT.

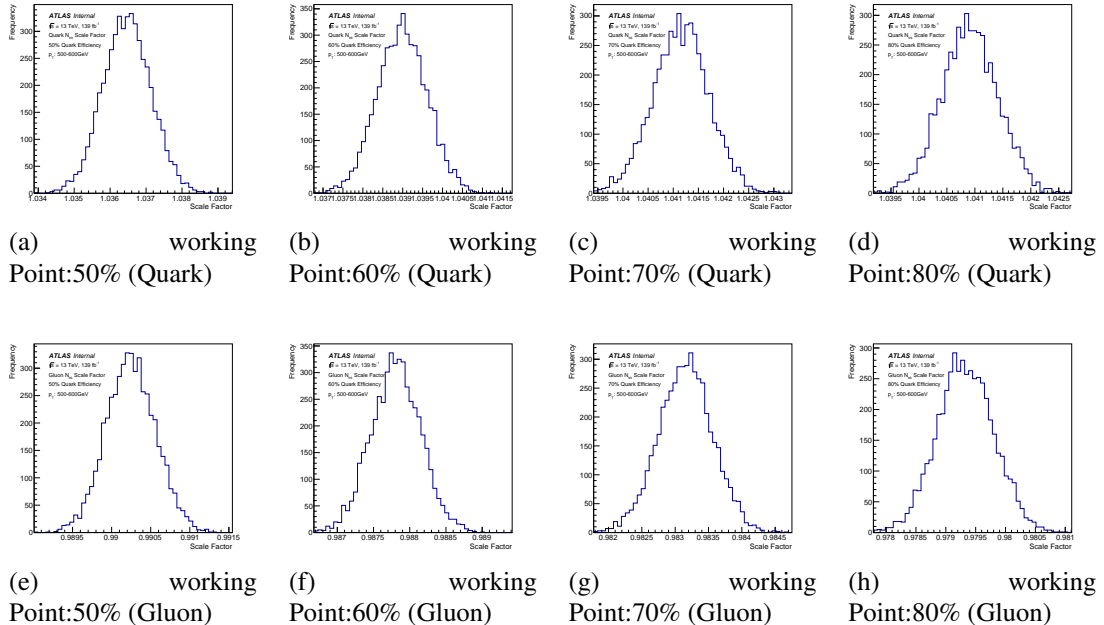


Figure 5.45 The distribution of SF by varying the input data distributions bin-by-bin using a Poisson distribution with the number of data events in each bin as the central value for 5000 times for working point of N_{trk} in jet p_T range 500-600 GeV.

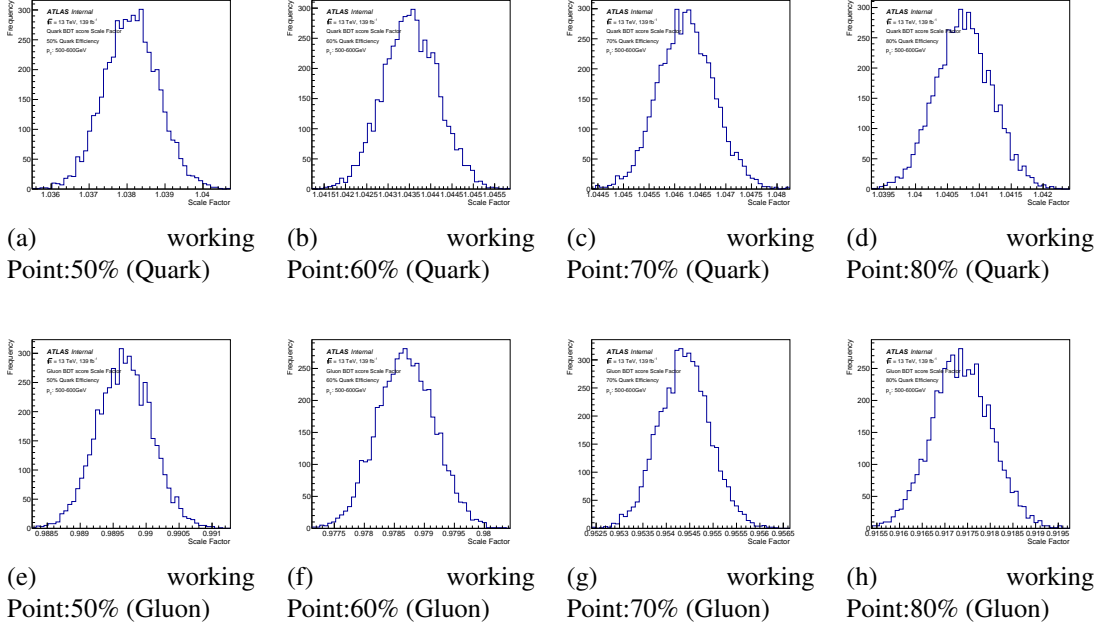


Figure 5.46 The distribution of SF by varying the input data distributions bin-by-bin using a Poisson distribution with the number of data events in each bin as the central value for 5000 times for working point of BDT in jet p_T range 500-600 GeV.

1253 5.8 Results

1254 Overall, both the N_{trk} -only tagger and the BDT-tagger exhibit commendable performance,
 1255 and can effectively distinguish quark-jet from gluon-jet with high efficiency. The
 1256 SFs for both quark- and gluon-jet fall within the range of approximately 0.9 to 1, indicating
 1257 a reasonable agreement. The systematic uncertainty for quark-jet SFs hovers around
 1258 10%, while for gluon-jet SFs it's approximately 20%. Detailed of each uncertainty are
 1259 shown in Section 5.7. The BDT-tagger showcases a slightly superior performance com-
 1260 pared to the N_{trk} only tagger, i.e. higher gluon-jet rejection at the same WP.

1261 The uncertainties of SF for each source of WP are estimated in each jet p_T range
 1262 are given from Table 5.6 to Table 5.13 for quark-jets. Table 5.14 to Table 5.21 show the
 1263 uncertainties of SF at each WP for gluon-jets. All systematics are ordered from largest to
 1264 smallest in p_T range 500 - 600 GeV. the systematic uncertainties associated with quark-
 1265 jet scale factors tend to be smaller than those linked to gluon-jet scale factors. Notably,

¹²⁶⁶ for both quark- and gluon-jets, these uncertainties are primarily governed by the source
¹²⁶⁷ of uncertainty stemming from parton showering.

Table 5.6 The quark scale factor (nominal) and the difference between the nominal and systematic variation results for 50% quark tag efficiency from $N_{\text{trk}}\text{tagger}$

	500-600	600-800	800-1000	1000-1200	1200-1500	1500-2000
nominal	1.02	1.04	1.04	1.03	1.02	1.01
scale variation	0.09	0.1	0.12	0.11	0.13	0.12
pdf weight	0.09	0.11	0.12	0.13	0.13	0.11
hadronization	0.09	0.07	0.06	0.05	0.04	0.04
tracking	0.08	0.07	0.06	0.05	0.05	0.04
matrix element	0.05	0.06	0.06	0.05	0.05	0.04
parton shower	0.02	0.03	0.05	0.06	0.07	0.08
MC nonclosure	0.02	0.04	0.04	0.03	0.02	0.01
splitting kernel	0.01	0.01	0.01	0.01	0.01	0.01
JES/JER	0.01	0.01	0.01	0.01	0.01	0.01
gluon reweight	0.01	0.01	0.01	0.01	0.01	0.01
Statistical	0.01	0.01	0.01	0.01	0.01	0.02
Total Uncertainty	0.19	0.19	0.21	0.21	0.22	0.19

Table 5.7 The quark scale factor (nominal) and the difference between the nominal and systematic variation results for 60% quark tag efficiency from $N_{\text{trk}}\text{tagger}$

	500-600	600-800	800-1000	1000-1200	1200-1500	1500-2000
nominal	1.03	1.04	1.04	1.03	1.01	1.01
pdf weight	0.09	0.1	0.12	0.12	0.12	0.1
tracking	0.08	0.07	0.06	0.05	0.05	0.04
scale variation	0.07	0.08	0.1	0.09	0.1	0.09
hadronization	0.06	0.05	0.04	0.04	0.03	0.03
matrix element	0.05	0.05	0.05	0.05	0.05	0.04
MC nonclosure	0.02	0.04	0.04	0.03	0.02	0.02
parton shower	0.02	0.03	0.03	0.04	0.06	0.08
splitting kernel	0.01	0.01	0.01	0.02	0.01	0.01
JES/JER	0.01	0.01	0.01	0.01	0.01	0.01
gluon reweight	0.01	0.01	0.01	0.01	0.01	0.01
Statistical	0.01	0.01	0.01	0.01	0.01	0.01
Total Uncertainty	0.16	0.17	0.18	0.18	0.18	0.17

Table 5.8 The quark scale factor (nominal) and the difference between the nominal and systematic variation results for 70% quark tag efficiency from N_{trk} tagger

	500-600	600-800	800-1000	1000-1200	1200-1500	1500-2000
nominal	1.03	1.04	1.04	1.03	1.02	1.0
pdf weight	0.08	0.09	0.11	0.11	0.11	0.08
tracking	0.07	0.06	0.05	0.05	0.04	0.03
scale variation	0.06	0.06	0.07	0.07	0.07	0.06
hadronization	0.05	0.04	0.04	0.03	0.03	0.02
matrix element	0.04	0.05	0.04	0.04	0.04	0.03
MC nonclosure	0.03	0.04	0.04	0.04	0.02	0.01
parton shower	0.02	0.02	0.02	0.03	0.04	0.05
splitting kernel	0.01	0.01	0.01	0.02	0.02	0.01
JES/JER	0.01	0.01	0.01	0.01	0.01	0.01
gluon reweight	0.01	0.01	0.01	0.01	0.01	0.01
Statistical	0.01	0.01	0.01	0.01	0.01	0.01
Total Uncertainty	0.14	0.14	0.16	0.16	0.15	0.13

 Table 5.9 The quark scale factor (nominal) and the difference between the nominal and systematic variation results for 80% quark tag efficiency from N_{trk} tagger

	500-600	600-800	800-1000	1000-1200	1200-1500	1500-2000
nominal	1.03	1.03	1.03	1.02	1.01	1.0
tracking	0.06	0.05	0.05	0.04	0.03	0.02
pdf weight	0.06	0.07	0.09	0.09	0.08	0.06
scale variation	0.03	0.04	0.05	0.04	0.04	0.05
MC nonclosure	0.03	0.04	0.04	0.03	0.02	0.01
hadronization	0.03	0.02	0.02	0.02	0.02	0.02
matrix element	0.03	0.04	0.03	0.03	0.03	0.02
parton shower	0.01	0.01	0.02	0.01	0.02	0.03
splitting kernel	0.01	0.01	0.01	0.02	0.02	0.01
JES/JER	0.01	0.01	0.01	0.01	0.01	0.01
gluon reweight	0.01	0.01	0.01	0.01	0.01	0.01
Statistical	0.01	0.01	0.01	0.01	0.01	0.01
Total Uncertainty	0.11	0.11	0.13	0.12	0.11	0.1

The calibration of quark/gluon jets taggers

Table 5.10 The quark scale factor (nominal) and the difference between the nominal and systematic variation results for 50% quark tag efficiency from BDT tagger

	500-600	600-800	800-1000	1000-1200	1200-1500	1500-2000
nominal	1.01	1.02	1.03	1.02	1.01	1.0
pdf weight	0.09	0.1	0.12	0.13	0.12	0.1
scale variation	0.09	0.1	0.12	0.12	0.13	0.1
hadronization	0.07	0.06	0.06	0.06	0.04	0.04
matrix element	0.05	0.06	0.06	0.05	0.05	0.04
tracking	0.05	0.05	0.05	0.04	0.04	0.04
MC nonclosure	0.01	0.01	0.02	0.01	0.01	0.01
parton shower	0.01	0.01	0.03	0.04	0.05	0.07
splitting kernel	0.01	0.01	0.01	0.01	0.02	0.01
gluon reweight	0.01	0.01	0.01	0.01	0.01	0.01
JES/JER	0.01	0.01	0.01	0.01	0.01	0.01
Statistical	0.01	0.01	0.01	0.01	0.01	0.02
Total Uncertainty	0.17	0.18	0.2	0.2	0.2	0.18

Table 5.11 The quark scale factor (nominal) and the difference between the nominal and systematic variation results for 60% quark tag efficiency from BDT tagger

	500-600	600-800	800-1000	1000-1200	1200-1500	1500-2000
nominal	1.02	1.03	1.04	1.03	1.02	1.01
pdf weight	0.09	0.1	0.11	0.12	0.12	0.1
scale variation	0.07	0.08	0.1	0.1	0.11	0.08
hadronization	0.06	0.05	0.05	0.05	0.03	0.04
tracking	0.05	0.05	0.05	0.04	0.04	0.04
matrix element	0.05	0.05	0.05	0.05	0.04	0.03
splitting kernel	0.01	0.01	0.01	0.01	0.02	0.01
gluon reweight	0.01	0.01	0.01	0.01	0.01	0.01
MC nonclosure	0.01	0.02	0.02	0.02	0.01	0.01
JES/JER	0.01	0.01	0.01	0.01	0.01	0.01
Statistical	0.01	0.01	0.01	0.01	0.01	0.01
parton shower	0.01	0.01	0.03	0.03	0.05	0.06
Total Uncertainty	0.15	0.16	0.18	0.18	0.18	0.15

The calibration of quark/gluon jets taggers

Table 5.12 The quark scale factor (nominal) and the difference between the nominal and systematic variation results for 70% quark tag efficiency from BDT tagger

	500-600	600-800	800-1000	1000-1200	1200-1500	1500-2000
nominal	1.03	1.04	1.04	1.03	1.02	1.02
pdf weight	0.08	0.09	0.1	0.11	0.1	0.08
scale variation	0.06	0.06	0.08	0.08	0.08	0.06
tracking	0.06	0.05	0.05	0.05	0.04	0.04
hadronization	0.05	0.04	0.04	0.04	0.03	0.03
matrix element	0.04	0.04	0.04	0.04	0.03	0.02
splitting kernel	0.01	0.01	0.01	0.02	0.01	0.01
parton shower	0.01	0.01	0.02	0.03	0.04	0.04
gluon reweight	0.01	0.01	0.01	0.01	0.01	0.01
JES/JER	0.01	0.01	0.01	0.01	0.01	0.01
MC nonclosure	0.01	0.02	0.03	0.02	0.01	0.01
Statistical	0.01	0.01	0.01	0.01	0.01	0.01
Total Uncertainty	0.13	0.13	0.15	0.15	0.15	0.12

Table 5.13 The quark scale factor (nominal) and the difference between the nominal and systematic variation results for 80% quark tag efficiency from BDT tagger

	500-600	600-800	800-1000	1000-1200	1200-1500	1500-2000
nominal	1.03	1.04	1.04	1.03	1.02	1.01
pdf weight	0.07	0.07	0.08	0.09	0.08	0.06
tracking	0.06	0.05	0.05	0.04	0.03	0.03
scale variation	0.04	0.05	0.06	0.06	0.05	0.05
hadronization	0.04	0.03	0.03	0.02	0.02	0.02
matrix element	0.03	0.04	0.03	0.03	0.02	0.02
splitting kernel	0.01	0.01	0.02	0.02	0.02	0.01
parton shower	0.01	0.01	0.02	0.02	0.02	0.03
gluon reweight	0.01	0.01	0.01	0.01	0.01	0.01
JES/JER	0.01	0.01	0.01	0.01	0.01	0.01
MC nonclosure	0.01	0.01	0.02	0.02	0.01	0.01
Statistical	0.01	0.01	0.01	0.01	0.01	0.01
Total Uncertainty	0.11	0.11	0.12	0.12	0.11	0.1

The calibration of quark/gluon jets taggers

Table 5.14 The gluon scale factor (nominal) and the difference between the nominal and systematic variation results for 50% gluon tag efficiency from N_{trk} tagger

	500-600	600-800	800-1000	1000-1200	1200-1500	1500-2000
nominal	0.99	0.98	0.98	0.96	0.94	0.92
parton shower	0.1	0.11	0.12	0.13	0.11	0.14
pdf weight	0.04	0.05	0.05	0.06	0.06	0.05
splitting kernel	0.02	0.01	0.01	0.01	0.01	0.01
tracking	0.01	0.02	0.02	0.02	0.02	0.01
hadronization	0.01	0.01	0.01	0.01	0.01	0.01
scale variation	0.01	0.01	0.01	0.01	0.01	0.01
MC nonclosure	0.01	0.01	0.02	0.04	0.06	0.07
matrix element	0.01	0.01	0.02	0.03	0.04	0.07
JES/JER	0.01	0.01	0.01	0.01	0.01	0.01
Statistical	0.01	0.01	0.01	0.01	0.01	0.02
gluon reweight	0.01	0.01	0.01	0.01	0.01	0.01
Total Uncertainty	0.11	0.12	0.13	0.15	0.15	0.18

Table 5.15 The gluon scale factor (nominal) and the difference between the nominal and systematic variation results for 60% gluon tag efficiency from N_{trk} tagger

	500-600	600-800	800-1000	1000-1200	1200-1500	1500-2000
nominal	0.99	0.98	0.97	0.95	0.92	0.91
parton shower	0.15	0.17	0.17	0.17	0.17	0.21
pdf weight	0.05	0.06	0.06	0.07	0.07	0.06
splitting kernel	0.03	0.01	0.01	0.01	0.01	0.02
scale variation	0.02	0.03	0.02	0.02	0.02	0.03
tracking	0.02	0.02	0.02	0.02	0.02	0.01
hadronization	0.01	0.01	0.01	0.01	0.01	0.01
MC nonclosure	0.01	0.02	0.02	0.04	0.07	0.08
matrix element	0.01	0.01	0.02	0.03	0.05	0.08
JES/JER	0.01	0.01	0.01	0.01	0.01	0.01
Statistical	0.01	0.01	0.01	0.01	0.01	0.03
gluon reweight	0.01	0.01	0.01	0.01	0.01	0.01
Total Uncertainty	0.17	0.18	0.18	0.2	0.2	0.25

The calibration of quark/gluon jets taggers

Table 5.16 The gluon scale factor (nominal) and the difference between the nominal and systematic variation results for 70% gluon tag efficiency from N_{trk} tagger

	500-600	600-800	800-1000	1000-1200	1200-1500	1500-2000
nominal	0.99	0.97	0.96	0.94	0.91	0.87
parton shower	0.21	0.22	0.23	0.24	0.25	0.31
pdf weight	0.06	0.06	0.07	0.08	0.08	0.07
splitting kernel	0.04	0.01	0.01	0.01	0.01	0.01
scale variation	0.04	0.04	0.03	0.04	0.03	0.04
tracking	0.02	0.02	0.02	0.02	0.01	0.01
hadronization	0.01	0.01	0.01	0.01	0.01	0.01
MC nonclosure	0.01	0.02	0.03	0.05	0.08	0.12
matrix element	0.01	0.01	0.02	0.03	0.06	0.09
JES/JER	0.01	0.01	0.01	0.01	0.01	0.01
gluon reweight	0.01	0.01	0.01	0.01	0.01	0.01
Statistical	0.01	0.01	0.01	0.01	0.01	0.03
Total Uncertainty	0.23	0.24	0.24	0.26	0.28	0.35

Table 5.17 The gluon scale factor (nominal) and the difference between the nominal and systematic variation results for 80% gluon tag efficiency from N_{trk} tagger

	500-600	600-800	800-1000	1000-1200	1200-1500	1500-2000
nominal	0.98	0.97	0.95	0.93	0.89	0.85
parton shower	0.32	0.31	0.33	0.37	0.37	0.45
scale variation	0.07	0.07	0.05	0.07	0.07	0.05
splitting kernel	0.07	0.02	0.02	0.03	0.01	0.02
pdf weight	0.06	0.07	0.07	0.09	0.09	0.08
tracking	0.01	0.01	0.01	0.01	0.01	0.01
MC nonclosure	0.01	0.03	0.04	0.06	0.1	0.15
matrix element	0.01	0.01	0.02	0.04	0.07	0.11
hadronization	0.01	0.01	0.01	0.01	0.01	0.01
JES/JER	0.01	0.01	0.01	0.01	0.01	0.01
gluon reweight	0.01	0.01	0.01	0.01	0.01	0.01
Statistical	0.01	0.01	0.01	0.01	0.01	0.03
Total Uncertainty	0.34	0.33	0.34	0.39	0.41	0.49

The calibration of quark/gluon jets taggers

Table 5.18 The gluon scale factor (nominal) and the difference between the nominal and systematic variation results for 50% gluon tag efficiency from BDT tagger

	500-600	600-800	800-1000	1000-1200	1200-1500	1500-2000
nominal	1.0	0.99	0.98	0.96	0.94	0.92
parton shower	0.09	0.08	0.1	0.1	0.1	0.13
pdf weight	0.04	0.04	0.05	0.05	0.06	0.04
splitting kernel	0.03	0.02	0.02	0.02	0.01	0.02
scale variation	0.01	0.01	0.01	0.01	0.01	0.03
MC nonclosure	0.01	0.02	0.03	0.05	0.06	0.09
hadronization	0.01	0.01	0.01	0.01	0.01	0.01
tracking	0.01	0.01	0.01	0.01	0.01	0.01
matrix element	0.01	0.01	0.02	0.02	0.04	0.07
gluon reweight	0.01	0.01	0.01	0.01	0.01	0.01
JES/JER	0.01	0.01	0.01	0.01	0.01	0.01
Statistical	0.01	0.01	0.01	0.01	0.01	0.02
Total Uncertainty	0.11	0.1	0.11	0.13	0.14	0.18

Table 5.19 The gluon scale factor (nominal) and the difference between the nominal and systematic variation results for 60% gluon tag efficiency from BDT tagger

	500-600	600-800	800-1000	1000-1200	1200-1500	1500-2000
nominal	0.99	0.98	0.97	0.95	0.93	0.91
parton shower	0.11	0.12	0.13	0.13	0.14	0.17
pdf weight	0.05	0.05	0.05	0.06	0.06	0.06
splitting kernel	0.05	0.03	0.03	0.03	0.01	0.04
MC nonclosure	0.02	0.03	0.04	0.06	0.08	0.1
scale variation	0.02	0.02	0.02	0.02	0.02	0.05
hadronization	0.01	0.01	0.01	0.01	0.02	0.01
tracking	0.01	0.01	0.01	0.01	0.01	0.01
matrix element	0.01	0.01	0.02	0.03	0.04	0.08
gluon reweight	0.01	0.01	0.01	0.01	0.01	0.01
JES/JER	0.01	0.01	0.01	0.01	0.01	0.01
Statistical	0.01	0.01	0.01	0.01	0.01	0.02
Total Uncertainty	0.13	0.14	0.15	0.16	0.18	0.23

The calibration of quark/gluon jets taggers

Table 5.20 The gluon scale factor (nominal) and the difference between the nominal and systematic variation results for 70% gluon tag efficiency from BDT tagger

	500-600	600-800	800-1000	1000-1200	1200-1500	1500-2000
nominal	0.98	0.97	0.95	0.93	0.89	0.86
parton shower	0.15	0.15	0.17	0.17	0.17	0.21
splitting kernel	0.07	0.05	0.05	0.04	0.03	0.05
pdf weight	0.05	0.06	0.06	0.07	0.07	0.06
MC nonclosure	0.05	0.05	0.07	0.09	0.12	0.15
scale variation	0.03	0.04	0.03	0.04	0.04	0.07
hadronization	0.02	0.01	0.01	0.01	0.01	0.01
tracking	0.01	0.01	0.01	0.01	0.01	0.01
matrix element	0.01	0.01	0.02	0.03	0.05	0.08
JES/JER	0.01	0.01	0.01	0.01	0.01	0.01
gluon reweight	0.01	0.01	0.01	0.01	0.01	0.01
Statistical	0.01	0.01	0.01	0.01	0.01	0.02
Total Uncertainty	0.18	0.18	0.2	0.21	0.23	0.29

Table 5.21 The gluon scale factor (nominal) and the difference between the nominal and systematic variation results for 80% gluon tag efficiency from BDT tagger

	500-600	600-800	800-1000	1000-1200	1200-1500	1500-2000
nominal	0.96	0.95	0.93	0.9	0.85	0.81
parton shower	0.19	0.18	0.21	0.2	0.22	0.28
splitting kernel	0.09	0.07	0.06	0.06	0.05	0.07
MC nonclosure	0.08	0.09	0.1	0.12	0.17	0.21
pdf weight	0.06	0.06	0.07	0.08	0.08	0.06
scale variation	0.05	0.05	0.05	0.05	0.07	0.08
hadronization	0.02	0.01	0.01	0.01	0.01	0.01
tracking	0.01	0.01	0.01	0.01	0.01	0.01
matrix element	0.01	0.01	0.02	0.03	0.06	0.09
JES/JER	0.01	0.01	0.01	0.01	0.01	0.01
Statistical	0.01	0.01	0.01	0.01	0.01	0.03
gluon reweight	0.01	0.01	0.01	0.01	0.01	0.02
Total Uncertainty	0.23	0.23	0.25	0.26	0.31	0.38

1268 Figure 5.47 to Figure 5.50 show the leading uncertainties with SFs for both tagger.
1269 The SFs for quark-jets and gluon-jets corresponding to the 50% quark-jets efficiency
1270 working point (WP) fall within the range of 0.92 to 1.02, while being subject to an ag-
1271 gregate systematic uncertainty of approximately 20%. Among the various sources of
1272 systematic uncertainty, theoretical modelling emerges as the dominant factor contribut-
1273 ing to the total uncertainty.

1274 To ascertain the robustness of the findings, tests are conducted to assess the stabili-
1275 ty of results across different regions of jet $|\eta|$. The SF measurements are recomputed
1276 through the normalization of jet $|\eta|$ in the quark-/gluon-enriched subsamples. The al-
1277 ternate results obtained in this manner are determined to be consistent with the nominal
1278 outcome, falling within the full range of reported uncertainties.

1279 Given the variations in the usage of different MC samples, a MC-to-MC SF is com-
1280 puted. This involves employing each alternative MC sample while treating the PYTHIA MC
1281 samples as pseudodata. This approach accommodates discrepancies arising from mod-
1282 elling difference between the PYTHIA and alternative MC samples. The MC-to-MC SFs
1283 for both jet taggers at each WP are shown in Figure 5.51 to Figure 5.54. Notably, there
1284 exists a large difference in gluon modelling between the HERWIG Dipole parton shower
1285 MC and the PYTHIA MC. This discrepancy is reflected in the relatively significant MC-
1286 to-MC SF, indicating substantial differences between these models.

The calibration of quark/gluon jets taggers

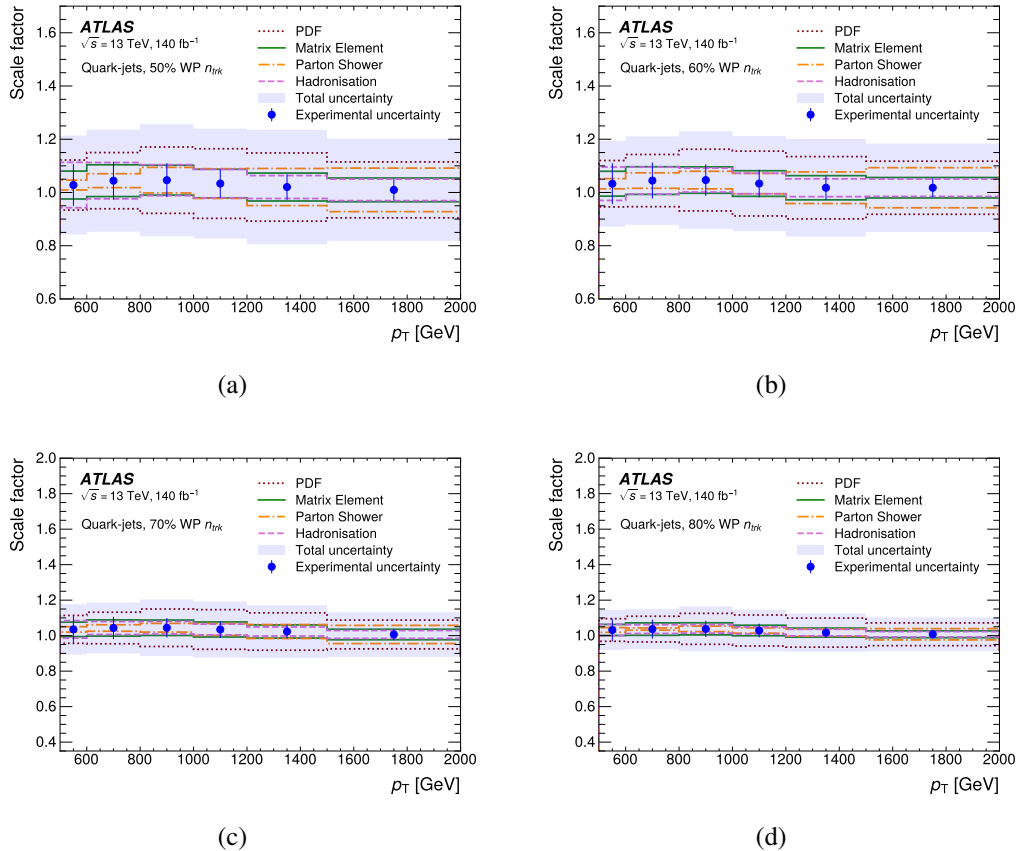


Figure 5.47 The SF with total and leading systematic uncertainty on the jet tagging variable N_{trk} obtained by PYTHIA 8 MCs as a function of jet p_T for quark-jets at each WP.

The calibration of quark/gluon jets taggers

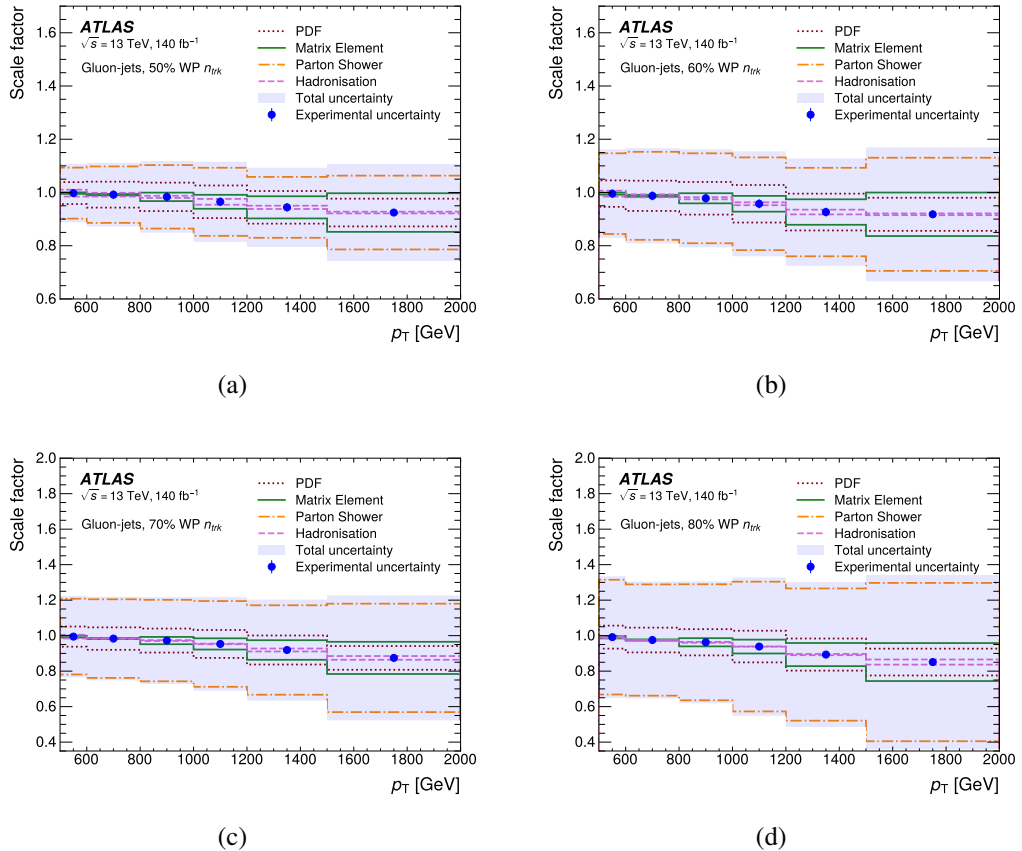


Figure 5.48 The SF with total and leading systematic uncertainty on the jet tagging variable N_{trk} obtained by PYTHIA 8 MCs as a function of jet p_T for gluon-jets at each WP.

The calibration of quark/gluon jets taggers

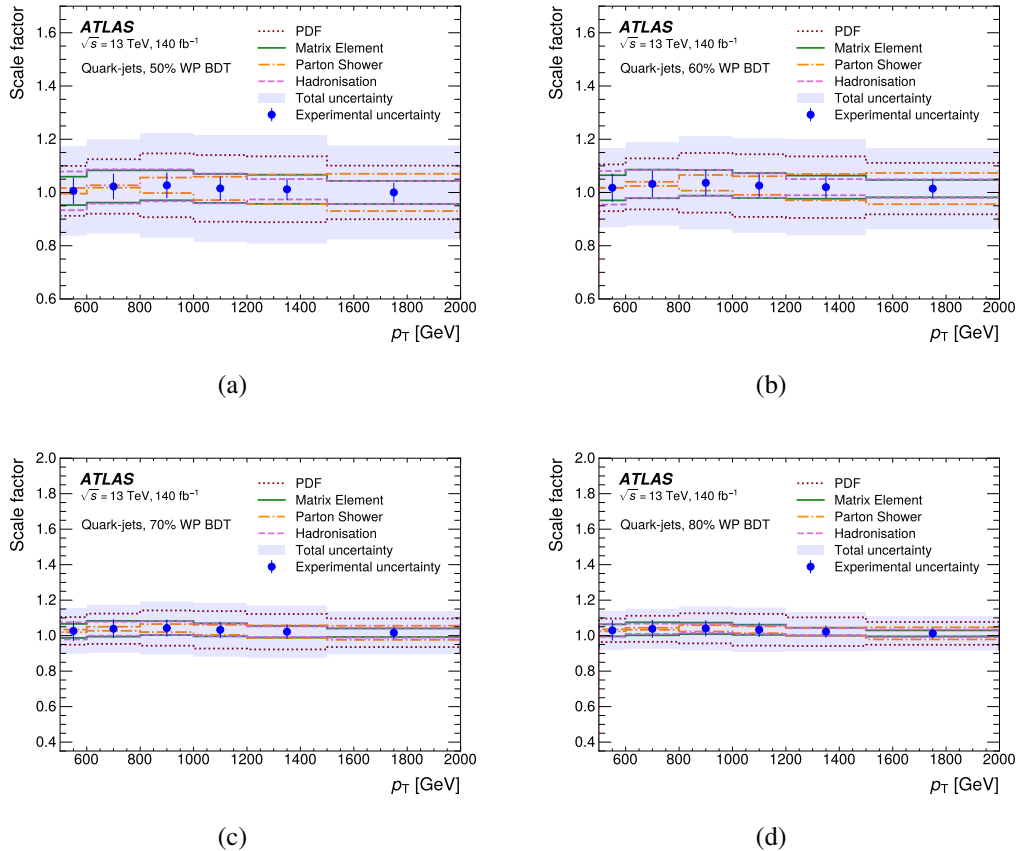


Figure 5.49 The SF with total and leading systematic uncertainty on the jet tagging variable BDT obtained by PYTHIA 8 MCs as a function of jet p_T for quark-jets at each WP.

The calibration of quark/gluon jets taggers

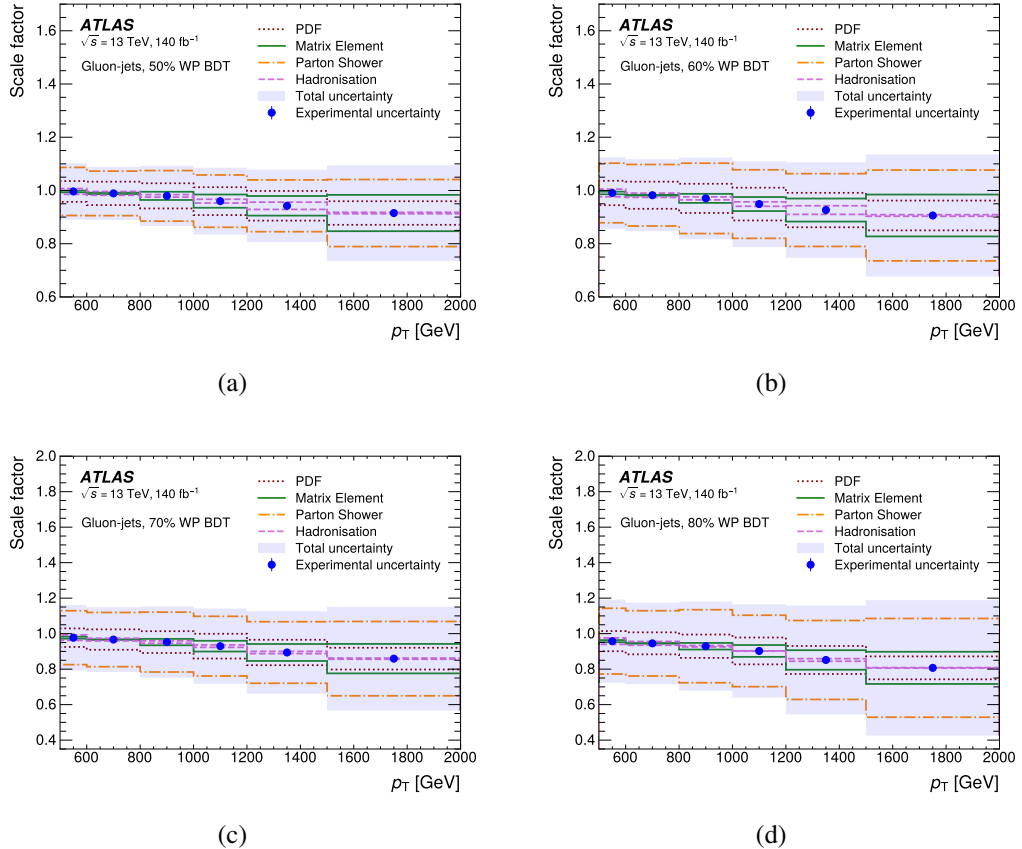


Figure 5.50 The SF with total and leading systematic uncertainty on the jet tagging variable BDT obtained by PYTHIA 8 MCs as a function of jet p_T for gluon-jets at each WP.

The calibration of quark/gluon jets taggers

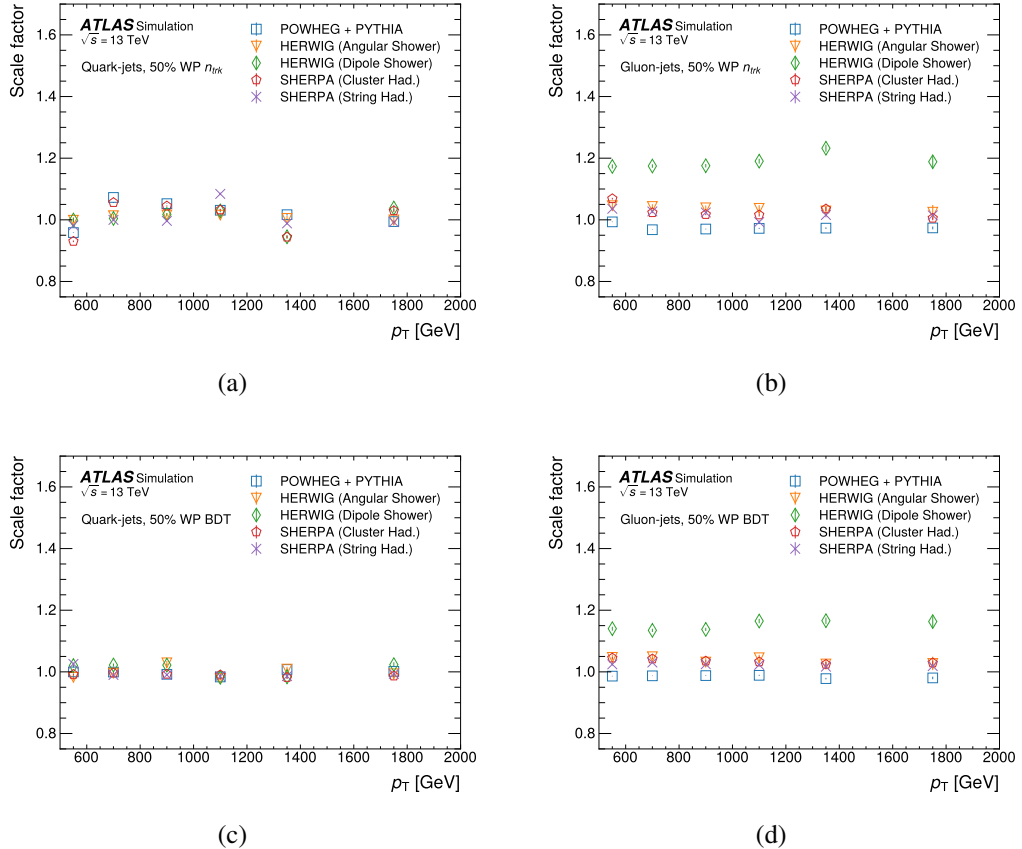


Figure 5.51 The MC-to-MC SF of the N_{trk} , (a) and (b), and BDT, (c) and (d), as a function of jet p_T for quark-jets (left) and gluon-jets (right) at the 50% WP. The vertical error bars show the statistical uncertainty.

The calibration of quark/gluon jets taggers

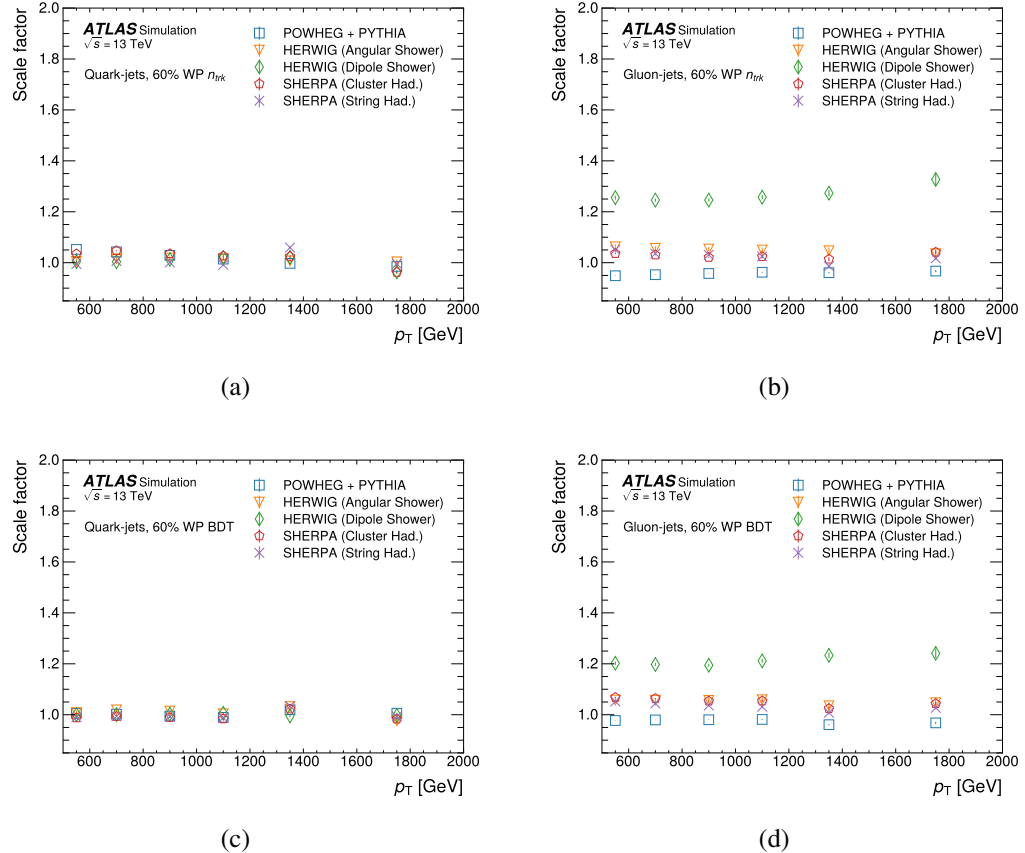


Figure 5.52 The MC-to-MC SF of the N_{trk} , (a) and (b), and BDT, (c) and (d), as a function of jet p_T for quark-jets (left) and gluon-jets (right) at the 60% WP. The vertical error bars show the statistical uncertainty.

The calibration of quark/gluon jets taggers

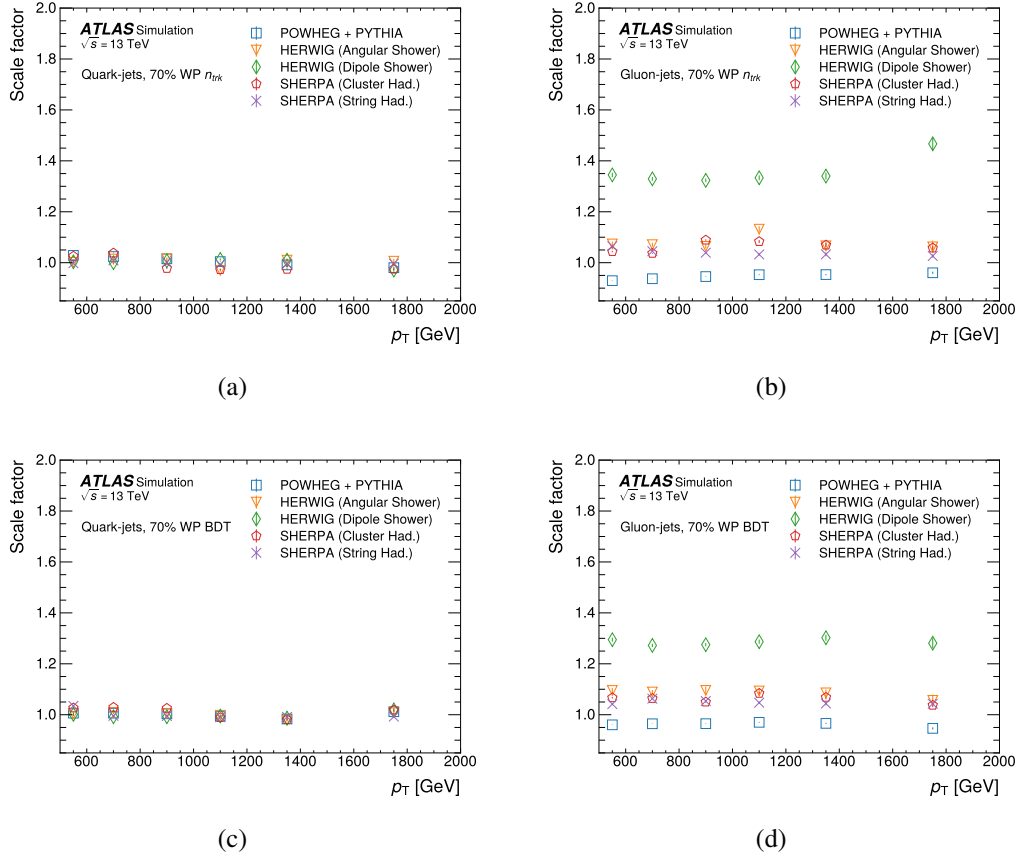


Figure 5.53 The MC-to-MC SF of the N_{trk} , (a) and (b), and BDT, (c) and (d), as a function of jet p_T for quark-jets (left) and gluon-jets (right) at the 70% WP. The vertical error bars show the statistical uncertainty.

The calibration of quark/gluon jets taggers

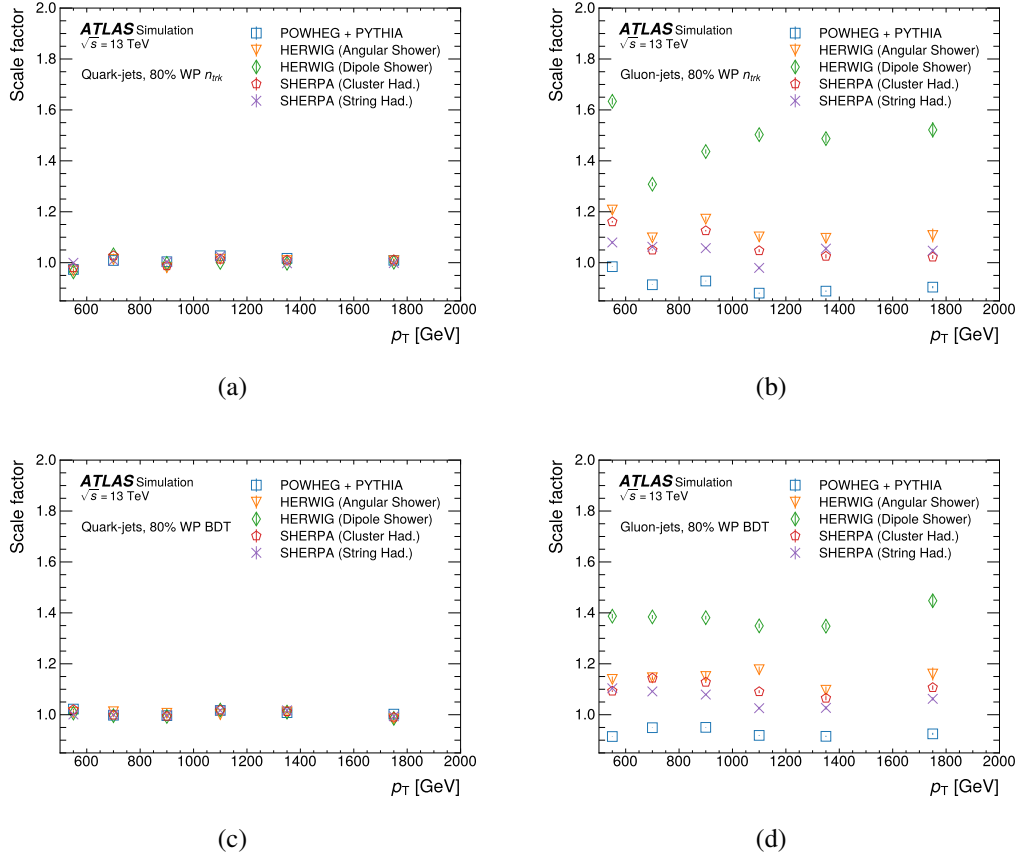


Figure 5.54 The MC-to-MC SF of the N_{trk} , (a) and (b), and BDT, (c) and (d), as a function of jet p_T for quark-jets (left) and gluon-jets (right) at the 80% WP. The vertical error bars show the statistical uncertainty.

1287

6 Search for new phenomena in dijet events

1288 As described in Section 2, the heavy resonance predicted by many BSM play a key role
1289 in understanding many fundamental phenomena. The narrow heavy resonance which
1290 decays into two gluons final state at the LHC, appears to be two hadronic jets in the
1291 detector. Produced by the QCD processes, the dijet events have a smoothly falling dis-
1292 tribution of the invariant mass m_{jj} , whereas two jets appear to be a resonance in the
1293 m_{jj} spectrum. As a result, searches for dijet resonance are one of the flagship exotics
1294 analyses in ATLAS.

1295 Besides, on the assumption that the resonant sample can be classified according to
1296 the type of parton that initiated the jets, the sensitivity of searches for new resonance
1297 can be improved by identifying the types of partons through which the potentially new
1298 particle interact. One of simplest examples of such tagging is gluon-tagging one or more
1299 of the jets. The jet tagging procedure based on the number of charged tracks with trans-
1300 verse momentum p_T above 500 GeV is described in Section. 5. The m_{jj} spectrum of
1301 background is estimated from the data, which is used for the search in three categories:
1302 inclusive, single-gluon, and double-gluon tagged dijet systems. The inclusive m_{jj} spec-
1303 trum is thus considered as control region for quark/gluon studies.

1304 This chapter describes searches for new heavy particles decay in dijet final state
1305 as originating from gluons or quarks, a technique of quark/gluon tagging is employed
1306 to enhance the sensitivity to the results. The search performed uses full Run 2 data
1307 at $\sqrt{s} = 13$ TeV, with higher integrated luminosity compared to previous one (Run 1),
1308 significantly improvements in the understanding of systematic uncertainties are expected.
1309 On the other hand, cross section upper limits will be set if no significantly resonances
1310 are observed.

1311 The simplified procedures in this analysis is performed as following:

- 1312 • Search for high-mass resonances in the untagged (inclusive), single-gluon tagged,
1313 and two-gluon tagged categories with dijet events.
- 1314 • If significant resonances are found, claim something interesting, else the upper
1315 limits are set.
- 1316 • Model independent upper-limits are set on resonance cross sections in inclusive,
1317 single-gluon tagged, and two-gluon tagged categories.

-
- 1318 • For the specific resonance model, set lower limits on the relevant scales in inclu-
 1319 sive, single-gluon tagged, and two-gluon tagged categories. dijet systems.

1320 **6.1 Monte Carlo models**

1321 . This section outlines benchmark models for both background from the QCD and
 1322 for new physics signals that encapsulated in the models chosen: Strings, graviton and
 1323 QBH. Full Run 2 data are used to produce EXOT2 skimmed samples used in this analy-
 1324 sis [77].

1325 **6.1.1 QCD background**

1326 QCD processes from the MC are simulated at LO and NLO in SM perturbative
 1327 theory. Due to the large range in cross section of QCD sample [78], the samples are thus
 1328 sliced based on the leading jet p_T , to obtain comparable statistical precision across the
 1329 jet p_T range of interest.

1330 **6.1.2 String**

1331 As the SM has lots of well known problems such as the quadratically divergent
 1332 corrections to the Higgs self-energy, supersymmetry theory offers a solution to it by
 1333 fine-tuning the cancellation. The superstring theory, additional to the supersymmetry,
 1334 can perform as a framework that unify theories from SM at TeV-scale to quantum gravity
 1335 at Planck-scale.

1336 The fundamental string scale is chosen to be within TeV scale, denotes as string
 1337 mass-scale M_s . The string resonances could happen at masses $m_n = \sqrt{n}M_s$, for $n =$
 1338 $1, 2, 3, \dots$, where the resonance consist of the Regge excitations of quark, gluon, as well
 1339 as the colour singlet that lives on the QCD stack of branes. In total, five string scales
 1340 M_s range from 7.0 TeV to 9.0 TeV, in steps of 0.5 TeV are generated for string-resonance
 1341 samples [79]. The lower limits of mass M_{\min} provided in the generator are shown in
 1342 Table 6.22, together with the resulting cross section of the string samples.

1343 Searches for string resonances have been done in previous dijet mass spectra [80,
 1344 81, 82, 83, 84, 85]. It is worth noting that the string resonance searches mentioned in
 1345 these references have limitations in terms of model constraints and the clarity of the
 1346 methodologies used.

M_s [TeV]	M_{\min} [TeV]	Cross section [fb]
7.0	6.06	7.09E+0
7.5	6.60	1.86E+0
8.0	7.14	4.56E-1
8.5	7.60	1.00E-1
9.0	8.05	1.99E-2

Table 6.22 MC string-resonance samples with string scale M_s , minimum mass M_{\min} , and cross section.

1347 The first ($n = 1$) resonant pole is considered in this study. The widths of string-
 1348 resonances have been calculated in this Ref [79]. As the string resonances have long
 1349 Breit-Wigner tails, the PDFs at low- x (low mass) can significantly enhance the tail. In
 1350 this study, the low-mass tail is truncated since only narrow-resonance structure in m_{jj}
 1351 spectrum is interesting to this analysis. In the range $7.0 \leq M_s \leq 8.0$ TeV, the truncation
 1352 is done at the minimum value in the differential cross section on the lower-mass side of
 1353 the M_s peak, results in around 95% of the area under the Breit-Wigner curve. In the range
 1354 $7.0 \leq M_s \leq 8.0$ TeV, the truncation is done at a lower-mass point that covers 95% of
 1355 the area under the Breit-Wigner curve.

1356 The distribution of signal peak at different mass points is shown in Figure 6.55, the
 1357 distributions are normalized to unity and thus the differences in peak amplitudes are not
 1358 the changes in cross section.

1359 There are five possible $2 \rightarrow 2$ subprocesses from string resonances are simulated.
 1360 with the cross section for each subprocess vary as a function of M_s shown in Table 6.23.
 1361 The dominate subprocess across the M_s values is considered to be $gq \rightarrow gq$, which con-
 1362 tributes around 81-87% of the total cross section. The rest of subprocesses: $qq \rightarrow qq$,
 1363 $\bar{q}\bar{q} \rightarrow \bar{q}\bar{q}$, and $q\bar{q} \rightarrow q\bar{q}$ are model dependent and thus do not included in this analysis.

1364 For generating string samples, the MC event generator STRINGS 1.00 [86] with
 1365 interfaced to PYTHIA 8.240 [50] for parton shower modelling is used, together with the
 1366 A14 tune. The CTEQ6L1 [87] PDF set at the LO is used for the parton shower and the
 1367 hard-scattering process. The decaying processes is simulated using the EvtGen 1.6.0
 1368 program. [88].

1369 The effect from pile-up is simulated by overlaying the MC inelastic pp events gen-
 1370 erated with PYTHIA 8.186 with a PDF set of NNPDF2.3 at LO and the A3 [89] tune over

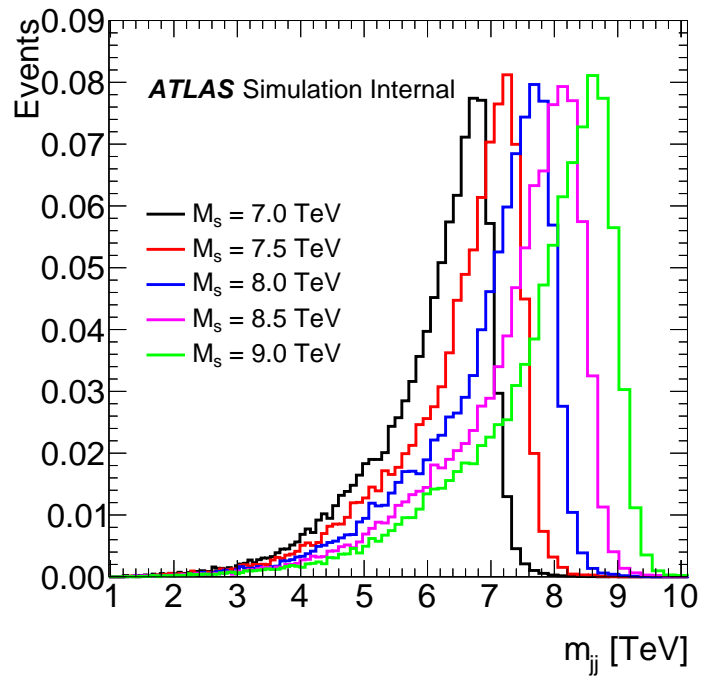


Figure 6.55 Signal shapes for the String signal.

¹³⁷¹ the original hard-scattering events.

Subprocess	M_s [TeV]				
	7.0	7.5	8.0	8.5	9.0
$gg \rightarrow gg$	11.4%	9.5%	8.2%	7.2%	5.1%
$gg \rightarrow q\bar{q}$	0.3%	0.3%	0.2%	0.2%	0.2%
$gq \rightarrow gq$	81.4%	83.1%	84.6%	85.5%	87.6%
$g\bar{q} \rightarrow g\bar{q}$	0.7%	0.6%	0.5%	0.5%	0.5%
$q\bar{q} \rightarrow gg$	6.3%	6.5%	6.5%	6.5%	6.7%

Table 6.23 String-resonance subprocesses and their relative contributions to the total cross section at each string scales M_s . The statistics are based on samples of 66000 events.

6.1.3 Kaluza-Klein Graviton

For the RS KK graviton samples considered in this study, we focus on $k/\overline{M}_{PI} = 0.2$. These samples encompass both gluon-gluon and quark-quark initial states, with decays exclusively to gluons or bottom quarks.

The signal templates for the KK gravitons are generated with different mass values using the PYTHIA 8 event generator. These simulations utilize the A14 tune and NNPDF2.3 PDF set.

Figure 6.56 shows the Graviton to gg invariant mass distribution for the considered mass points.

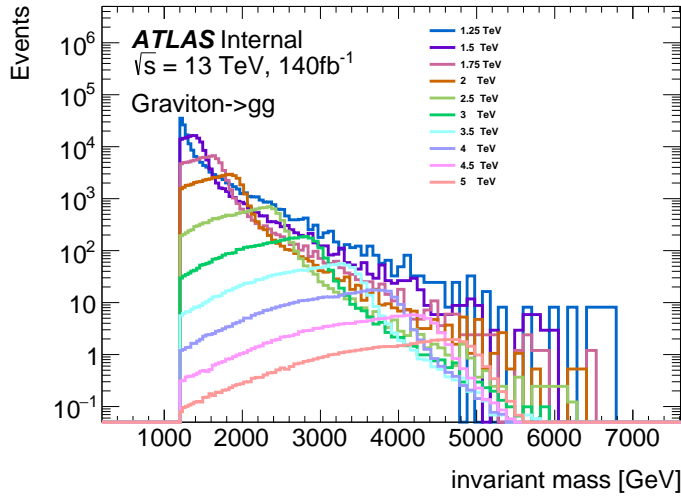


Figure 6.56 (a) Invariant mass distribution for the Graviton to gg samples

1381 **6.1.4 Quantum Black Hole**

1382 In our study, we employ the QBH model for the purpose of comparing limits with
1383 the previous iteration of the analysis. The feasibility of producing QBHs at the LHC
1384 is contingent upon the presence of sufficiently large extra dimensions within the uni-
1385 verse [90]. This model posits that the energy scale of quantum gravity M_D , at which
1386 QBHs are generated, diminishes as the number of these large extra dimensions, denoted
1387 as n , increases. Consequently, a larger n permits lower mass scales at which QBHs can
1388 be formed.

1389 Two-body isotropic final state is expected by the QBH decay at the LHC, where
1390 the M_D energy threshold could be reached [91]. Therefore the quantum gravitational
1391 effects can be probed by searches on m_{jj} spectrum. To simulate events involving quantum
1392 black holes with $n = 6$, we utilize the BlackMax [92] MC generator. This MC generator
1393 facilitates the simulation of QBH events within the $n = 6$ framework.

1394 **6.1.5 Gaussian resonances**

1395 One way to demonstrate the search in the analysis is to set limits on the cross-section
1396 of signal modes. Here a model-independent signal as Gaussian [93] are used to expand
1397 the sensitivity of the search to new signals that may be detectable with this analysis but
1398 not currently theoretically described. Besides, a model-independent signal could help to
1399 evaluate and compare the strength of different analyses without bias, as the case where
1400 specific models are applied and leads less sensitive to the search.

1401 Therefore, model-independent limits are produced based on model-independent sig-
1402 nal resonances. Because this analysis is sensitive to the shape of resonance, specific
1403 models with different shapes would influence the results strongly. In general, a model-
1404 independent signal is a good feature of the analysis which verify the ability to distinguish
1405 different signal models, although the model-independent limits are still influenced by the
1406 shape of the resonance in an implicit way. The motivation to choose a Gaussian reso-
1407 nance as a proxy is the fact that it is similar to the ‘average’ signal with specific width.
1408 Besides, the shape of reconstructed jet p_T of any realistic signal without very specific
1409 model is produced approximately as a Gaussian resonance, without applied JER. Hence
1410 it is straightforward to use Gaussian resonances to represent any realistic resonance.

1411 The general form of Gaussian distribution is:

$$f(x) = \frac{1}{\sigma\sqrt{2\pi}} e^{-\frac{1}{2}\left(\frac{x-\mu}{\sigma}\right)^2} \quad (6.1)$$

1412 where the parameter μ is the mean or expectation of the distribution (and also its median
1413 and mode), while the parameter σ is its standard deviation.

1414 6.2 Events selections

1415 The MC and data events are divided into three categories to perform the search:
 1416 the untagged dijet invariant mass spectrum, one-gluon tagged spectrum, and two-gluon
 1417 tagged spectrum. The evidence of BSM resonances would appear as peaks in the m_{jj}
 1418 spectrum formed by two highest p_T jets in the events. A series of specific cuts is applied
 1419 to improved the sensitivity of the searches.

1420 6.2.1 Observables and Kinematic Variables

1421 The predominant source of dijet events in the SM is two-to-two scattering though
 1422 the QCD processes. This search exams two key properties of the QCD background:

- 1423 • The background at high m_{jj} appears as a smooth and continuously falling spec-
 1424 trum.
- 1425 • The background at high energy strongly peaks in the forward region as a result
 1426 of Rutherford t - and u -channel poles in the cross sections for certain scattering
 1427 processes [94].

1428 Resonances of interest have $\cos \theta$ distributions in the detector, which in contrast to
 1429 Rutherford scattering, are either isotropic or have polynomial behaviour in $\cos \theta$ ¹, thus
 1430 a angular distribution appears. This search therefore defines a y^* to indicate the angle
 1431 separation of the jets in the selected events:

$$y^* = (y_1 - y_2)/2 \quad (6.2)$$

1432 to improve the sensitivity to higher energies where new phenomena are expected. The
 1433 variables y_1, y_2 represent the rapidity of the leading and subleading jet. The value of the
 1434 y^* cut on events is optimized for each signal as discussed in Section .6.4.1.

1435 In this analysis, jets are reconstructed with the anti- k_t algorithm with a radius pa-
 1436 rameter $R = 0.4$, as implemented in the FASTJET package [95]. The EMTopo jets, re-
 1437 constructed from topological clusters via procedures described in Section .4.1, are used.
 1438 The standard *Loose* cut is applied to jet quality as well as jet cleaning. The summarized
 1439 jet criteria are shown in Table 6.24.

¹See Ref. [94] p15 for a summary.

Parameter / Observable	Requirement
Algorithm	anti- k_t
R-parameter	0.4
Input Constituent	EMTopo
p_T	>150 GeV
$ \eta $	<2.1

Table 6.24 Jet selection criteria used in this analysis.

6.2.2 Baseline selection

The triggers used in this analysis is HLT_j420. Besides, two single-jet trigger HLT_j225_gsc420_boffperf_split is also used as the unprescaled trigger for full Run 2 data. Both triggers have the threshold of $p_T > 420$ GeV of the jets, while the GSC is applied to the HLT_j225_gsc420_boffperf_split to the trigger turn-on improvement. A turn-on based on the m_{jj} spectrum is found to be much powerful than the cut requirement of the leading jet p_T , where the m_{jj} cut imposes a soft cut on the leading and subleading jet, respectively [96]. More details are shown in Section 6.4.2.

The baseline event selection is applied for all categories. The GRL and various flags that indicate the status of detector when taking data are provided by the ATLAS Data Quality (DQ) group, are applied to ensure the data integrity. Primary vertex requirement is also included to ensure good quality jets. The

- All jets with $p_T > 150$ GeV pass *Loose* cleaning cuts
- Passes the lowest unprescaled single-jet trigger: HLT_j420
- Jet multiplicity ≥ 2
- Leading jet $p_T > 380$ GeV and subleading jet $p_T > 150$ GeV
- Leading jet $|\eta| < 2.1$ and subleading jet $|\eta| < 2.1$
- $|\Delta\phi|$ between two jets: $|\Delta\phi| > 1.0$
- $m_{jj} > 1100$ GeV

Additional kinematic criteria are applied according to the distributions of signals, in order to optimize the search potential, are then discussed in Section 6.4.1.

6.3 Quark-Gluon Sample Selection

The sensitivity of the search on the resonant is expected to increase by distinguishing the type of parton that initiated the jets. The parton types of dijet events as a function of m_{jj} from the MC with a PYTHIA8.186 at LO NNPDF2.3 PDFs is shown in Figure 6.57, suggesting that the search for new resonance can be improved by tagging quark and gluon jets.

In this section we present the search for new particles using the full Run 2 $\sqrt{s} = 13$ TeV dataset with quark and gluon tagging method.

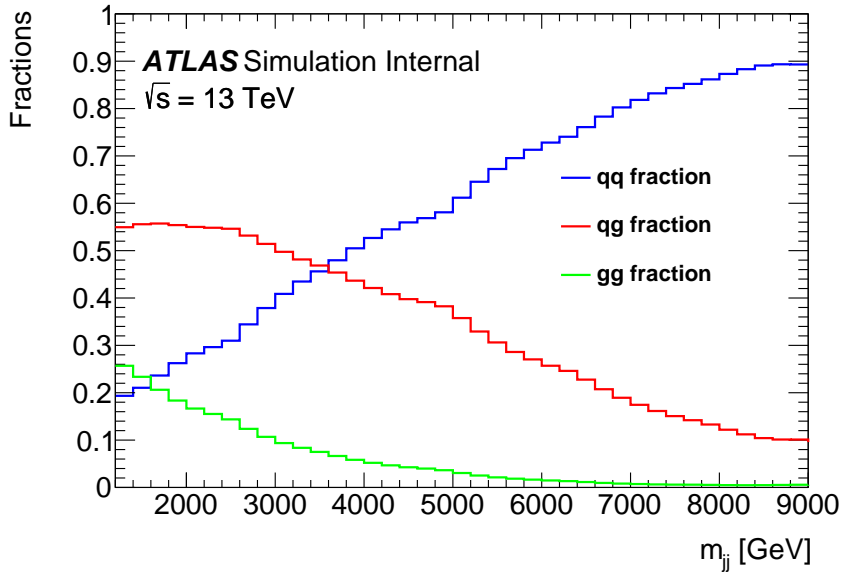


Figure 6.57 The fraction of dijet events that are initiated by quark-quark events (blue), quark-gluon events (green) and gluon-gluon events (red) in simulated data.

Previous study in ATLAS has shown that the jets can be tagged quark or gluon jets based on the number of charged tracks associated with the jets with p_T above 500 MeV. Samples with enhanced fractions of quark or gluon initiated jets can be created by using a selection based on the charged-particle constituent multiplicity N_{trk} . As shown in Figure 6.58, where PYTHIA 8 generator is used for MC to ensure a good agreement with the distribution of N_{trk} in data within the ID acceptance $|\eta| < 2.1$.

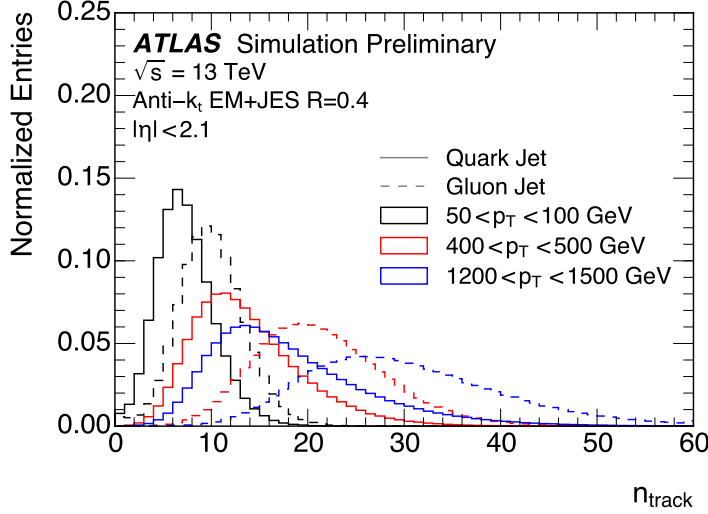


Figure 6.58 Distribution of the jet reconstructed track multiplicity (N_{trk}) in different p_{T} ranges with the PYTHIA 8 MC samples and processes with a full simulation of the ATLAS detector. Tracks are required to have $p_{\text{T}} > 500$ MeV and pass quality criteria described in Ref. [47].

1475 6.3.1 Selection Criteria

1476 The selection criteria for an quark-enriched jet sample was chosen so that 60%
 1477 quark-initiated purity is achieved in each jet p_{T} bin. However, discontinuities in the m_{jj}
 1478 spectrum would occur when such criteria is applied to the high mass ($p_{\text{T}} > 5000$ GeV),
 1479 leads to difficulties presented in resonance search.

A selection criteria is thus built as a linear function of the $\ln(p_{\text{T}})$, results in a smooth m_{jj} distribution. A jet is tagged as being more likely to be quark-initiated if N_{trk} is less than the threshold n_q and more likely to be gluon-initiated if N_{trk} is greater than the threshold n_g :

$$N_{\text{trk}} \leq n_q \text{ quark-initiated sample} \quad (6.3)$$

$$N_{\text{trk}} \geq n_g \text{ gluon-initiated sample}$$

1480 where

$$n_{q(g)} = c_{q(g)} + m_{q(g)} \ln(p_{\text{T}}) \quad (6.4)$$

1481 parameters $m_{q(g)}$ and $c_{q(g)}$ are constants obtained from the MC samples, these are founded
 1482 by finding the value of N_{trk} that corresponds to a given efficiency for truth quark and gluon
 1483 jets in p_{T} bins, and chosen to defined suitable subsamples, the p_{T} here is in units of GeV.

1484 For each p_T bin, the number of tracks N_{trk} that closest to the given selection effi-
 1485 ciency is found. Because the N_{trk} is an integer number of track thus does not correspond
 1486 exactly to the selection efficiency, a linear interpolation is carried out between the given
 1487 efficiencies of the selected bin and the closest bin of it, to correct the fractional number
 1488 of tracks that corresponds to the selection efficiency, the corresponding uncertainty is
 1489 evaluated as binomial distribution.

1490 The jet p_T bin edges are divided into 480, 500, 520, 540, 560, 580, 600, 625, 650,
 1491 700, 750, 800, 900, 1000, 1400, 1600, 1800, 2000, 2500, 3000, 3500, 4000, 5000, 6000
 1492 GeV. An example of the cumulative distribution of N_{trk} for truth quark- and gluon-jets at
 1493 the p_T range of 800 - 900 GeV is shown in Figure 6.59.

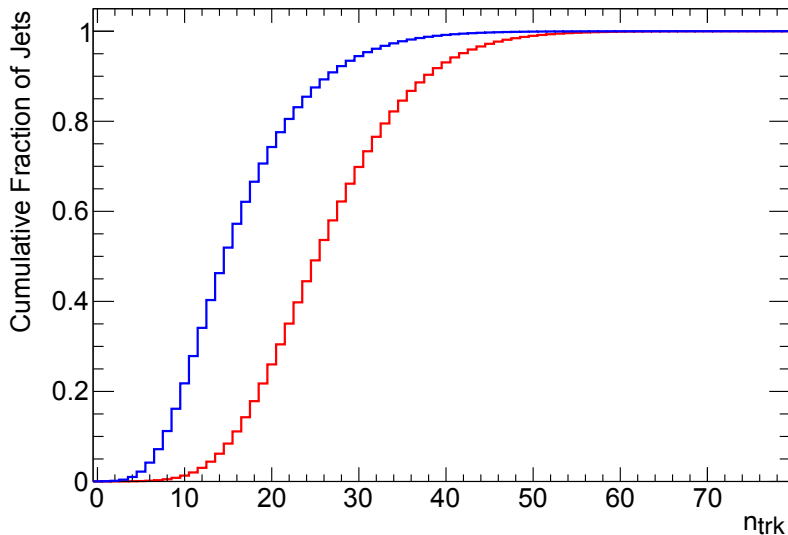


Figure 6.59 The cumulative distribution of N_{trk} for truth quark- (blue) and gluon- (red)jets satisfying $800 < p_T < 900$ GeV.

1494 The coefficients for Equation 6.4 are determined for quark and gluon selection ef-
 1495 ficiencies ranging from 65% to 95% in increments of 5%. The plot showcasing the N_{trk}
 1496 values corresponding to selection efficiencies of 70%, 75%, and 80% is depicted in Fig-
 1497 ure 6.60, along with the optimal fit employing Equation 6.4. The constants' values for
 1498 both quark and gluon selections are summarized in Tables 6.25 and 6.26. For a selec-
 1499 tion efficiency of 75%, the fitting yields a χ^2 of 33.5 (quark selection) and 2.6 (gluon
 1500 selection) for 21 degrees of freedom.

1501 Notably, the N_{trk} value that satisfies the selection efficiency attains a plateau above
 1502 4000 GeV, suggesting the potential presence of a saturation effect. To validate these

1503 findings, the data is subjected to an alternative fit function. An alternative fit function is
 1504 derived as a cross check:

$$n_{q(g)} = c + m \ln(p_T) + n \sqrt{\ln(p_T)}. \quad (6.5)$$

1505 which improve the χ^2 of the fit in a selection efficiency of 75% from 33.5 to 25.1 in
 1506 quark-selection, and from 2.6 to 1.6 in gluon-selection. Figure 6.61 shows the alternative
 1507 fit for quark and gluon selections. The values of the constants for both quark and gluon
 1508 selections are summarised in Tables 6.27 and 6.28.

1509 The values of the constants for both quark and gluon selections are summarised in
 Tables 6.25 and 6.26.

Truth- <i>q</i> selection efficiency	Truth- <i>g</i> selection efficiency	<i>c</i>	<i>m</i>
0.95	0.732	-27.568	8.789
0.90	0.563	-21.518	7.269
0.85	0.447	-17.646	6.304
0.80	0.350	-14.956	5.610
0.75	0.278	-12.600	5.022
0.70	0.221	-10.691	4.536
0.65	0.174	-8.990	4.105

Table 6.25 Values of constants *m* and *c* from Equation. 6.4 such that $N_{\text{trk}} \leq n_q$ for truth quark jets for a range of efficiencies from 65 to 95%.

1510

Truth- <i>g</i> selection efficiency	Truth- <i>q</i> selection efficiency	<i>c</i>	<i>m</i>
0.95	0.586	-7.541	3.233
0.90	0.456	-8.980	3.779
0.85	0.377	-10.419	4.230
0.80	0.320	-11.964	4.659
0.75	0.274	-13.376	5.047
0.70	0.234	-14.937	5.446
0.65	0.202	-16.466	5.834

Table 6.26 Values of constants *m* and *c* from Equation 6.4 such that $N_{\text{trk}} \geq n_g$ for truth quark jets for a range of efficiencies from 65 to 95%.

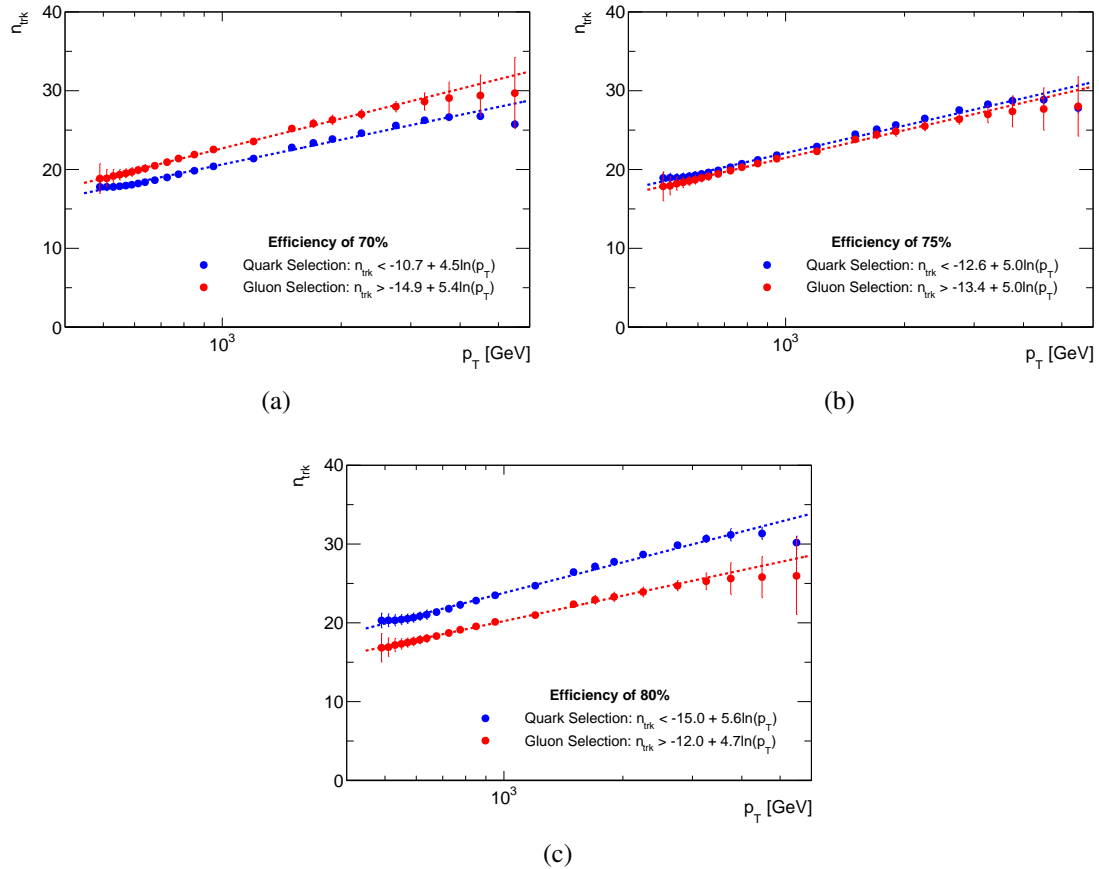


Figure 6.60 The values of N_{trk} for (a) 70%, (b) 75% and (c) 80% quark (blue) and gluon (red) selection efficiencies in each p_T bin along with the best fit to Equation 6.4.

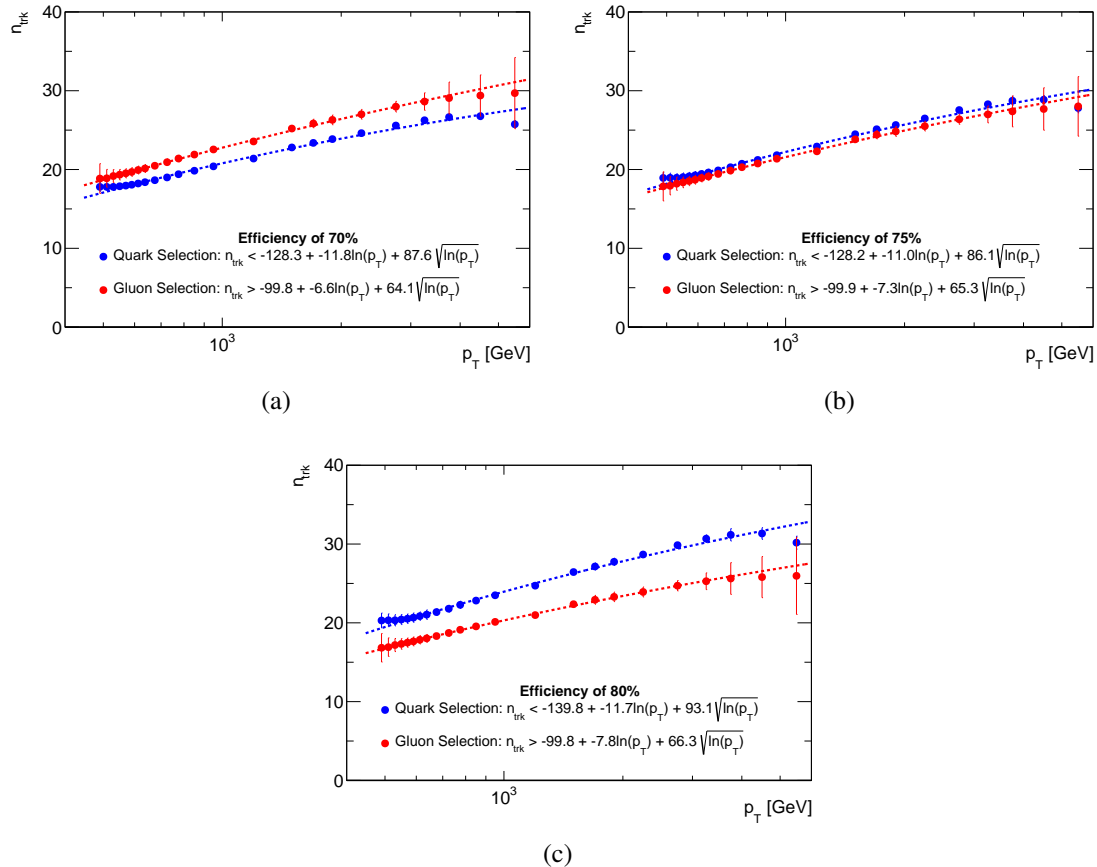


Figure 6.61 The values of N_{trk} for (a) 70%, (b) 75% and (c) 80% quark (blue) and gluon (red) selection efficiencies in each p_T bin along with the best fit to Equation 6.5.

Truth- q selection efficiency	Truth- g selection efficiency	c	m	n
0.80	0.350	-139.822	-11.714	93.100
0.75	0.278	-128.174	-11.001	86.141
0.70	0.221	-128.255	-11.755	87.604

Table 6.27 Values of constants m and c from Equation 6.5 such that $N_{\text{trk}} \leq n_q$ for truth quark jets for a range of efficiencies from 70 to 80%.

Truth- g selection efficiency	Truth- q selection efficiency	c	m	n
0.80	0.320	-99.796	-7.839	66.301
0.75	0.274	-99.949	-7.271	65.347
0.70	0.234	-99.774	-6.640	64.077

Table 6.28 Values of constants m and c from Equation 6.5 such that $N_{\text{trk}} \geq n_g$ for truth quark jets for a range of efficiencies from 70 to 80%.

1511 6.4 Signal Optimisation

1512 6.4.1 y^* Cut Optimisation

1513 In QCD, t -channel in 2-to-2 scattering is the dominant process. Thus the dijet pro-
 1514 duction from the QCD is proportional to $(1 - \cos \theta^*)^{-2}$. However the distribution of
 1515 $\cos \theta^*$ is supposed to be flat for H' signal, which means the y^* of H' signal will peak at 0
 1516 while that of QCD background will minimize at 0.

1517 The significance is defined as:

$$1518 S = \sqrt{\sum_i 2 \left[(S_i + B_i) \cdot \ln \left(1 + \frac{S_i}{B_i} \right) - S_i \right]} \quad (6.6)$$

1518 where S_i (B_i) is the number of signal (background) events in bin i . The calculation of
 1519 such significance only include the bins where signal samples have 95% of the area under
 1520 the distribution, not include the entire m_{jj} distribution.

1521 For some signal samples where S_i is small ($S_i \ll 10^{-5}$) thus the logarithm functions
 1522 do not have enough precision in equation 6.6. An approximation is introduced as follows:

$$1523 S = \sqrt{\sum_i 2 \sum_{n=1}^6 \frac{(-S_i)^{n+1}}{n(n+1)B_i^n}} \quad (6.7)$$

1524 which is accurate up to 10 decimal places around $\frac{S_i}{B_i} = 10^{-5}$ and even more precise for
 1525 smaller $\frac{S_i}{B_i}$.

1526 For String signal, there is also a dependence on $\cos \theta^*$, leads the y^* will peak at 0
 1527 too. Figure. 6.62 shows the significance of String signal as a function of y^* cut. The
 1528 maximum significance in all tagging categories are around 0.8, therefore an optimal y^*
 1529 cut for the String search is set to $|y^*| < 0.8$. The exact values of y^* cut that correspond
 1530 to the peak significance value for the String signal at each mass point are shown in
 1531 Table. 6.29 with the ranges in y^* cut around the peak that gives a significance ≥ 0.99 .

1532 Figure. 6.63 shows the significance of Graviton signal as a function of y^* cut. The
 1533 significance peaks at about 0.6, so the optimal cut for the Graviton search is $|y^*| < 0.6$.
 1534 Table. 6.30 shows the y^* cut corresponding to the peak significance value for Graviton at
 1535 each mass point, and the range in y^* cut around the peak that gives a significance ≥ 0.99

1536 Figure. 6.64 shows the significance of QBH signal as a function of y^* cut. The
 1537 maximum significance is at about 0.9, so the optimal cut for the QBH search is $|y^*| < 0.9$.

Search for new phenomena in dijet events

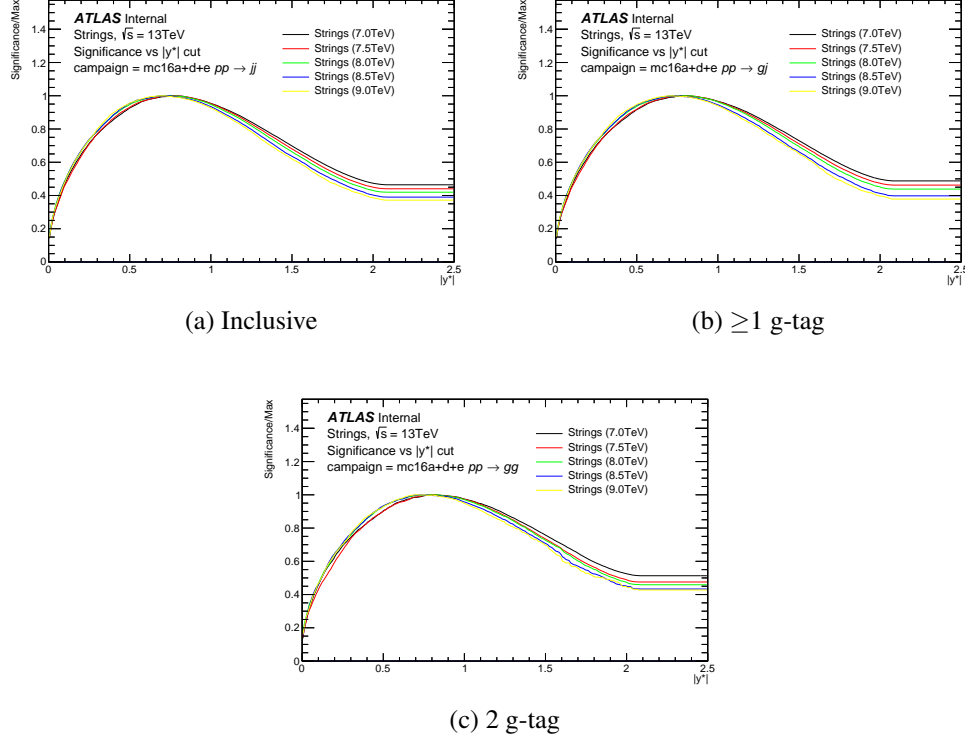


Figure 6.62 String significance as a function y^* cut in the case of (a) Inclusive, (b) ≥ 1 g-tag, (c) 2 g-tag.

String Mass (TeV)	Optimal Selection			Peak Width
	Inclusive	≥ 1 g tag	2 g tag	
7.0	0.78	0.82	0.81	0.70–0.91
7.5	0.77	0.77	0.83	0.68–0.91
8.0	0.72	0.76	0.84	0.66–0.90
8.5	0.74	0.74	0.74	0.65–0.85
9.0	0.71	0.71	0.71	0.62–0.84

Table 6.29 $|y^*|$ selection leading to the maximum significance value calculated using Equation 6.6.

1538 Table. 6.31 shows the y^* cut corresponding to the peak significance value for the QBH at
1539 each mass point, and the range in y^* cut around the peak that gives a significance ≥ 0.99

Search for new phenomena in dijet events

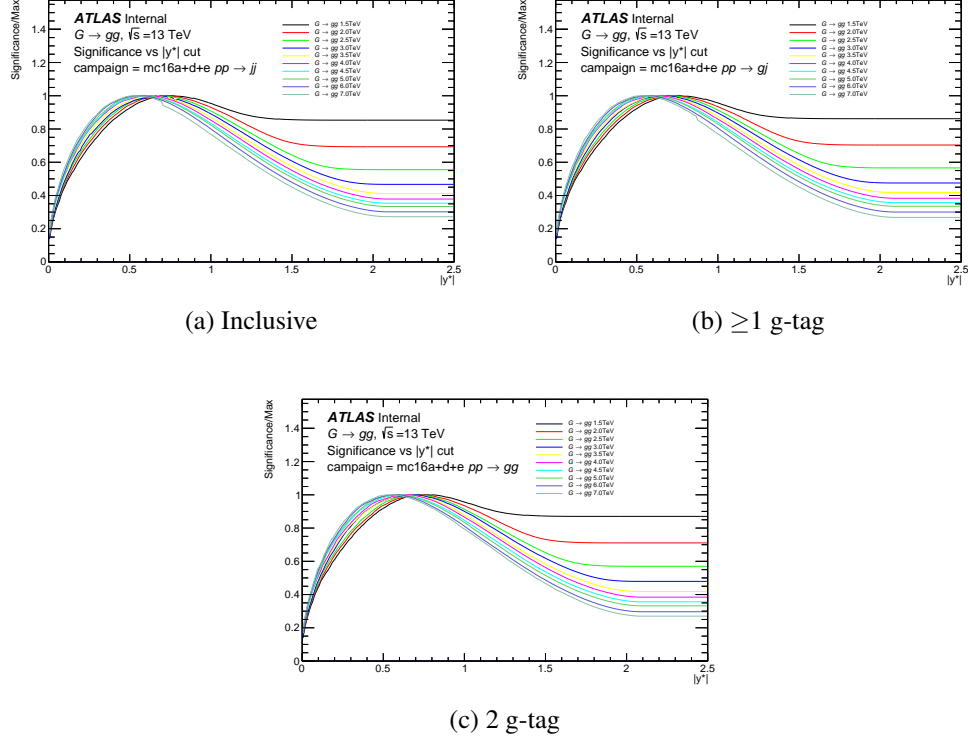


Figure 6.63 Graviton significance as a function y^* cut in the case of (a) Inclusive, (b) ≥ 1 g-tag, (c) 2 g-tag.

Graviton Mass (TeV)	Optimal Selection			Peak Width
	Inclusive	≥ 1 g tag	2 g tag	
1.5	0.77	0.77	0.78	0.65–0.87
2.0	0.71	0.74	0.72	0.65–0.83
2.5	0.67	0.69	0.70	0.61–0.80
3.0	0.66	0.66	0.66	0.60–0.77
3.5	0.64	0.65	0.65	0.57–0.73
4.0	0.63	0.64	0.64	0.55–0.73
4.5	0.59	0.59	0.59	0.53–0.69
5.0	0.59	0.59	0.59	0.50–0.69
6.0	0.57	0.57	0.60	0.49–0.66
7.0	0.53	0.53	0.56	0.47–0.63

Table 6.30 $|y^*|$ selection leading to the maximum significance value calculated using Equation 6.6.

Search for new phenomena in dijet events

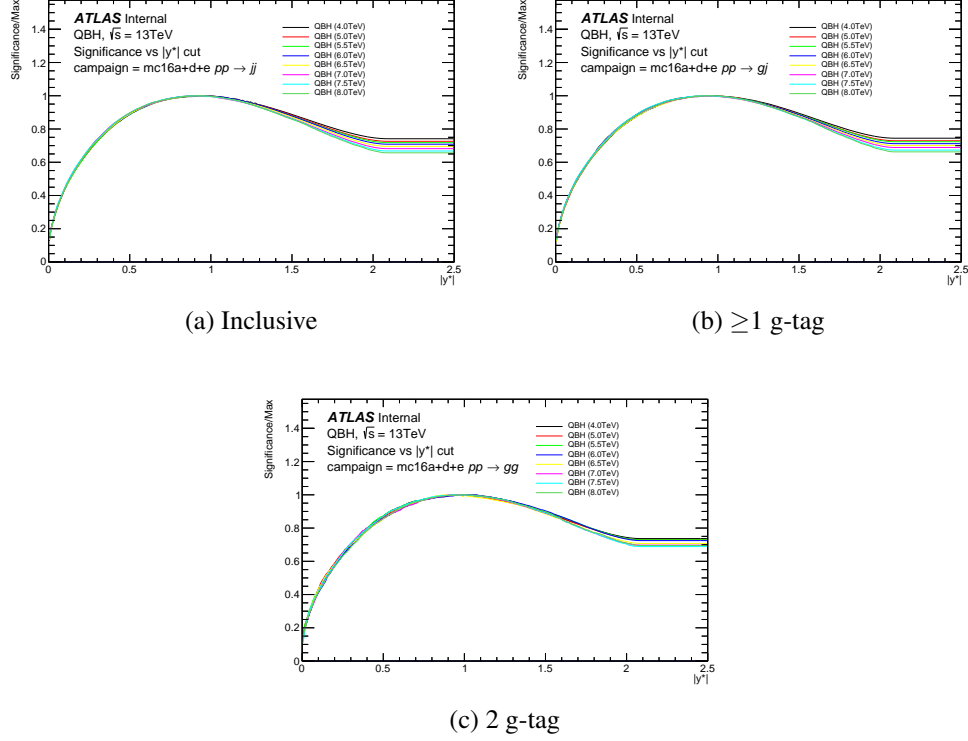


Figure 6.64 QBH significance as a function y^* cut in the case of (a) Inclusive, (b) ≥ 1 g-tag, (c) 2 g-tag.

QBH Mass (TeV)	Optimal Selection			Peak Width
	Inclusive	≥ 1 g tag	2 g tag	
4.0	0.92	0.95	1.01	0.81–1.11
5.0	0.95	0.95	0.95	0.81–1.09
5.5	0.94	0.96	0.94	0.81–1.09
6.0	0.92	0.96	1.01	0.81–1.09
6.5	0.91	0.91	0.93	0.81–1.06
7.0	0.93	0.97	0.94	0.82–1.07
7.5	0.92	0.94	0.93	0.79–1.08
8.0	0.92	0.96	0.99	0.82–1.09

Table 6.31 $|y^*|$ selection leading to the maximum significance value calculated using Equation 6.6.

6.4.2 Dijet Mass Turn-on

The m_{jj} turn-on is investigated by comparing events collected with the highest p_T trigger threshold with one with a lower p_T threshold using data. The efficiency of the HLT_j420 trigger is calculated by comparing to the following triggers in each data taking period: 2015 HLT_j360, 2016 HLT_j380, 2017 and 2018 HLT_mu50. The muon trigger 2017 and 2018 are included as HLT_j420 is the only unprescaled jet trigger available. The full Run 2 dataset is included for comparison as the HLT_mu50 is available for all running periods. Events where the efficiency of trigger less than 99.5% will be removed by a mass cut.

The efficiencies as a function of m_{jj} are shown in Figure. 6.65 for $|y^*| < 0.6$ and Figure. 6.66 for $|y^*| < 0.8$ in two gluon-tag categories for both triggers. The results are summarised in Table. 6.32 for the different data-taking periods. The m_{jj} mass cut is chosen to be slightly above the value of the plateau ($\geq 99.5\%$), so a cut of 1100 GeV for $|y^*| < 0.6$ is applied. For $|y^*| < 0.8$, a cut of 1200 GeV is applied to samples with either one or two gluon tags.

Data Taking Period	Mass turn on $ y^* < 0.6$		Mass turn on $ y^* < 0.8$	
	≥ 1 g-tag (GeV)	≥ 2 g-tag (GeV)	≥ 1 g-tag (GeV)	≥ 2 g-tag (GeV)
2015	1040	1030	1160	1160
2016	1030	1030	1160	1170
2017	990	1000	1110	1120
2018	1000	1010	1110	1120
Run 2	1020	1030	1120	1120

Table 6.32 The m_{jj} value of the start of the plateau ($\geq 99.5\%$) for each period of data taking.

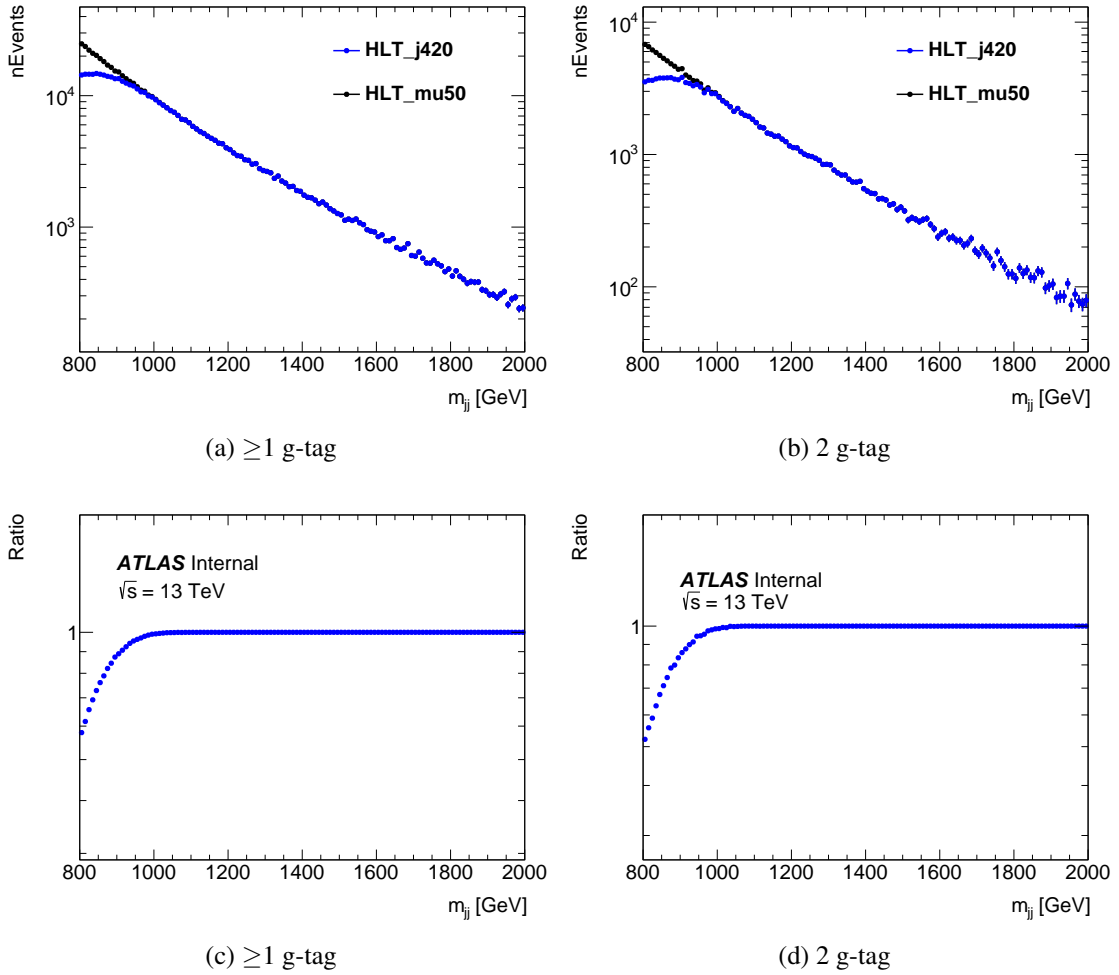


Figure 6.65 Eiciencies as a function of m_{jj} for $|y^*| < 0.6$ using HLT_j420 compared with HLT_mu50 in the case of comparison of mass spectra with (a) ≥ 1 g-tag, (b) 2 g-tag and the ratio between the two (c) ≥ 1 g-tag and (d) 2 g-tag.

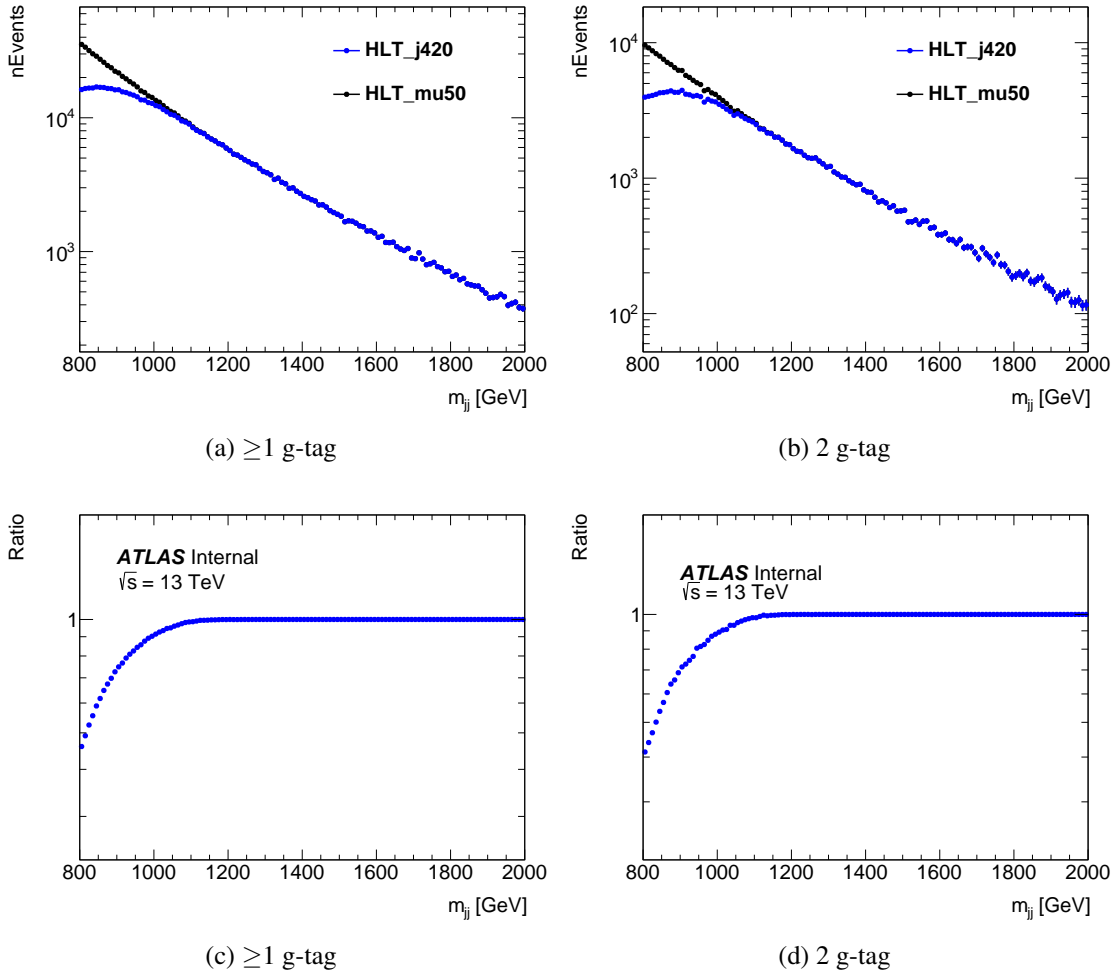


Figure 6.66 Eiciencies as a function of m_{jj} for $|y^*| < 0.8$ using HLT_j420 compared with HLT_mu50 in the case of comparison of mass spectra with (a) ≥ 1 g-tag, (b) 2 g-tag and the ratio between the two (c) ≥ 1 g-tag and (d) 2 g-tag.

1555 6.4.3 Optimised Selection

1556 In addition to the baseline selection described in Section 6.2.2, optimized cuts are
 1557 applied to different tagging regions to improve the search potential with good tracking
 1558 efficiency.

1559 The following additional cuts are applied for the the inclusive samples.

- 1560 • $|y^*| < 0.8$
- 1561 • $m_{jj} > 1200 \text{ GeV}$

1562 The following additional cuts are for quark-gluon tagging.

- 1563 • $|\eta| < 2.1$ (both jets) for track acceptance
- 1564 • ≥ 1 gluon tagged (75% working point)
- 1565 • 2 gluons tagged (75% working point)

1566 where the 75% gluon selection criteria is applied as: $N_{\text{trk}} > -7.3 + 4.2 \ln(p_T)$, with jet
 1567 p_T in GeV.

1568 The acceptance times efficiency as a function of signal masses in inclusive, signal-
 1569 gluon and double-gluon tagged regions for different benchmark signal models are shown
 1570 in Figure 6.67.

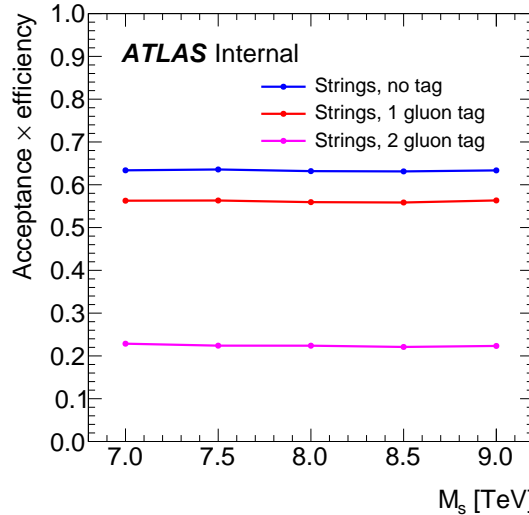


Figure 6.67 Acceptance times efficiency for the String signal.

1571 **6.4.4 Selected Kinematic Plots**

1572 In this section a selection of kinematic and monitoring plots processed with sam-
 1573 ples passed the gluon-gluon selection criteria are shown in Figure 6.68, 6.69, 6.70. The
 1574 distributions of kinematics in MC are consistent with full dataset.

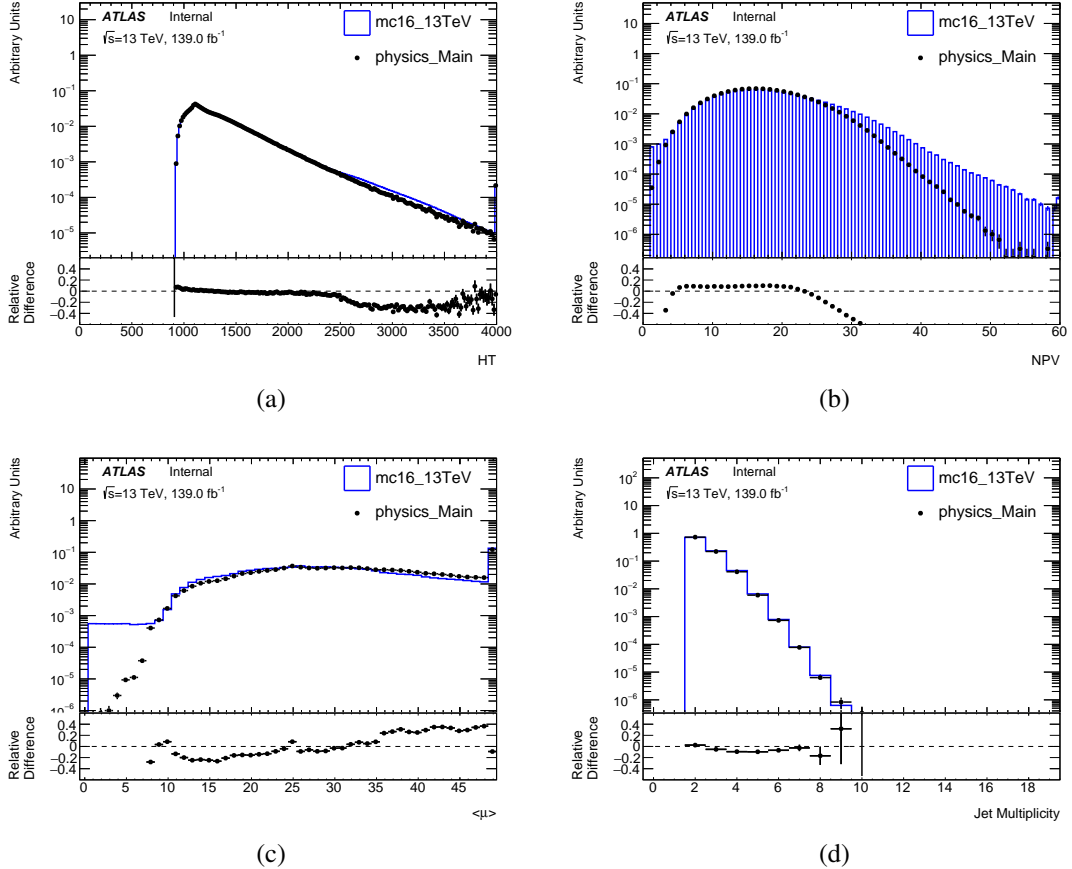


Figure 6.68 Monitoring plots for the gluon-gluon selection. (a) scalar p_T sum of all parton-level jets (H_T), (b) number of primary interaction vertices (NPV), (c) average interactions per bunch crossing, and (d) number of jets.

Search for new phenomena in dijet events

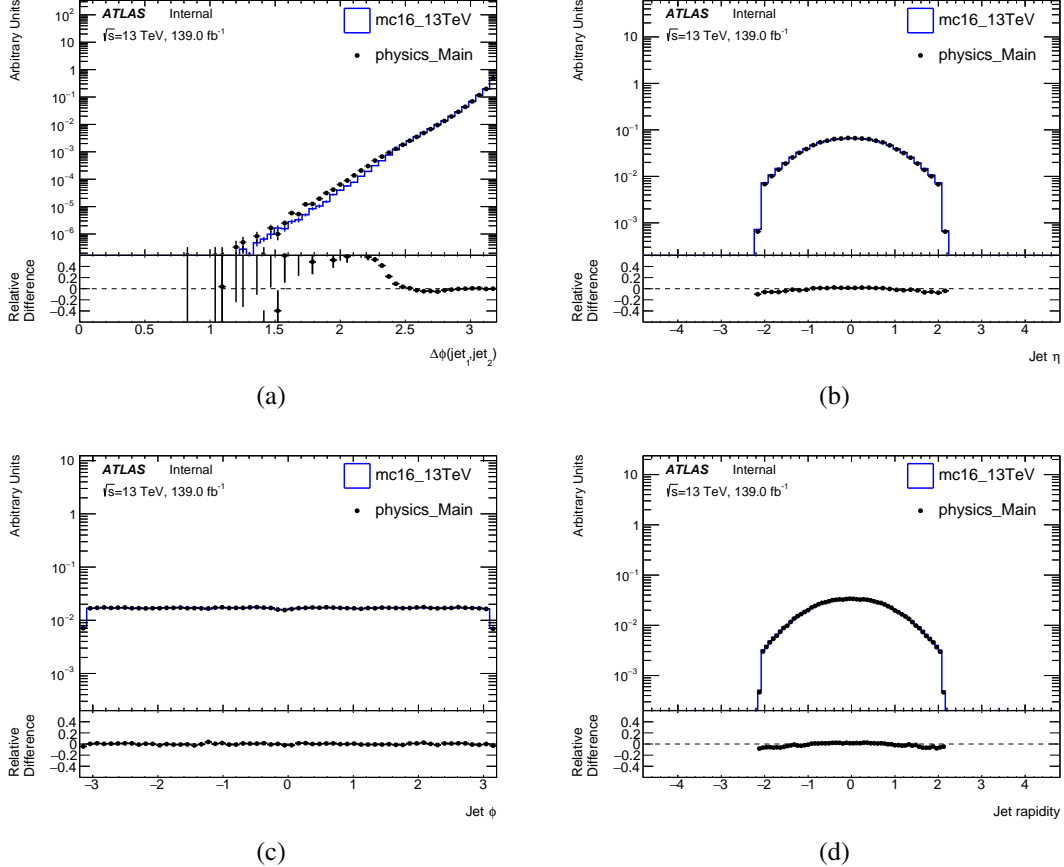


Figure 6.69 Monitoring plots on the gluon-gluon sample. (a) $\Delta\phi$ between the two jets, (b) jet η , (c) jet ϕ , and (d) jet rapidity.

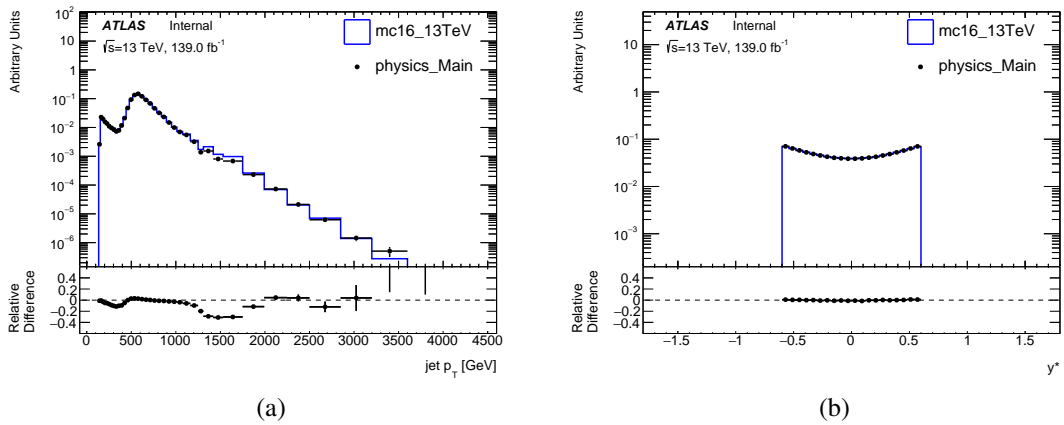


Figure 6.70 Monitoring plots on the gluon-gluon sample. (a) jet p_T , (b) y^* .

1575 6.5 Statistical Framework

1576 6.5.1 Fitting Framework

1577 The fitting framework used to parameterise QCD background is based on XML
 1578 Analytic Workspace Builder [97] (`xmlAnaWSBuilder`), which employs one-dimensional
 1579 observables to create RooFit [98] workspaces. The workflow of the framework is sum-
 1580 marised in Figure 6.71.

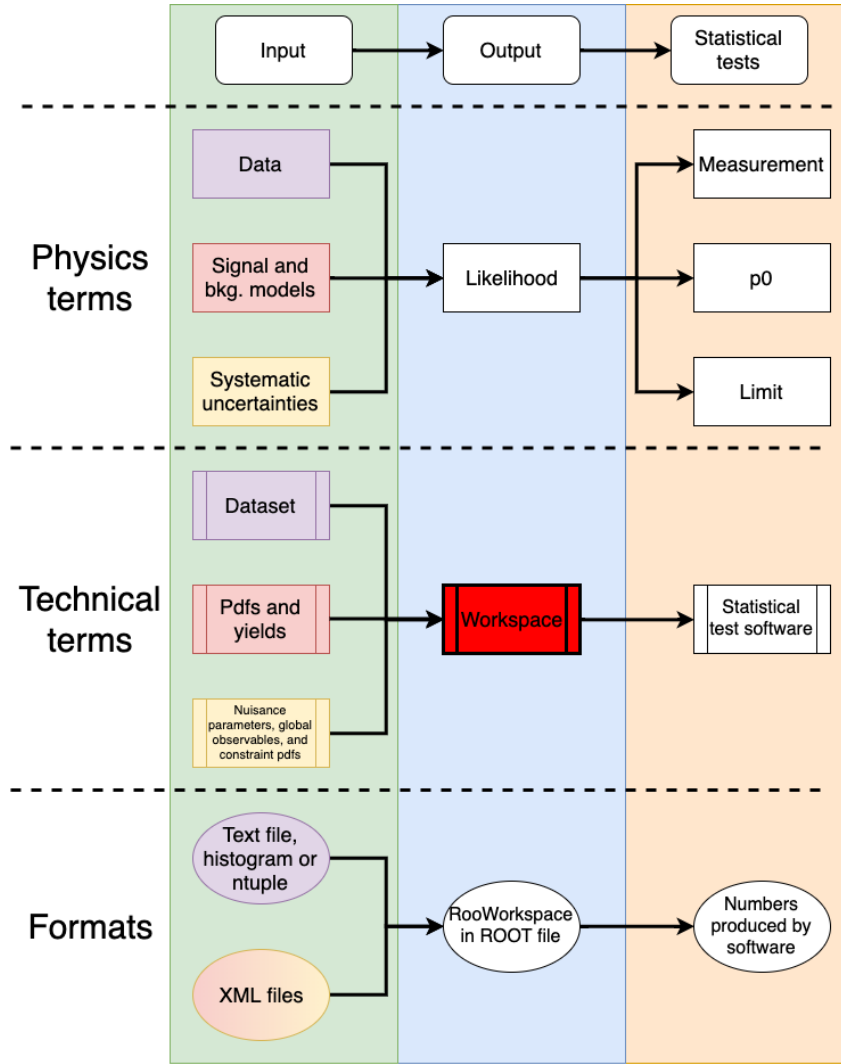


Figure 6.71 Workflow of the `XmlAnaWSBuilder`.

1581 The xRooFit framework [99] that based on RooFit data fitting package is used for
 1582 data fitting. Modifications are needed so that it can integrate over binned data, as RooFit
 1583 evaluates its fit functions using the centre value of each bin rather than the actual average

mass in each bin. As a result, significant biases could occur in the fit results [100]. Recent developments introduce a new class of `RooBinSamplingPdf` in to `RooFit` package, which solve such issue.

6.5.2 Statistical Method

In this analysis, the discriminating variable is set to the dijet invariant mass m_{jj} , and the distribution of it is used as a probability density function (pdf) to build the likelihood function.

6.5.2.1 Parametric background models

The distribution of m_{jj} of background is parameterized by

$$f_b(m_{jj}; \mathbf{p}_b) = f_b(m_{jj}; p_1, p_2, p_3, p_4, p_5) = p_1 \left(1 - \frac{m_{jj}}{\sqrt{s}}\right)^{p_2} \left(\frac{m_{jj}}{\sqrt{s}}\right)^{p_3 + p_4 \ln\left(\frac{m_{jj}}{\sqrt{s}}\right) + p_5 \left[\ln\left(\frac{m_{jj}}{\sqrt{s}}\right)\right]^2}, \quad (6.8)$$

where \mathbf{p}_b are free parameters determined by fitting to data (or pseudo data), and $\sqrt{s} = 13$ TeV. In some cases, $p_5 = 0$ is taken. We will assume Equation (6.8) is normalized to unity as needed.

Given that we are employing a binned likelihood approach and working with histograms, it becomes essential to determine the average count of events in the i th bin, arising from both the signal and background contributions:

$$s_i = s_{\text{tot}} \int_{\text{bin } i} f_s(m_{jj}; \mathbf{p}_s) dm_{jj}, \quad (6.9)$$

$$b_i = b_{\text{tot}} \int_{\text{bin } i} f_b(m_{jj}; \mathbf{p}_b) dm_{jj}, \quad (6.10)$$

where f_s and f_b are pdfs of m_{jj} for the signal and background, respectively. The quantities s_{tot} and b_{tot} represent the total mean numbers of signal and background events. The variable b_{tot} is an additional nuisance parameter. The signal normalization s_{tot} is not treated as a parameter that can be adjusted, but rather is set to the value determined by the nominal signal model. The parameter can be expressed as $s_{\text{tot}} = \sigma L \epsilon$, where σ is fixed by the model cross section, and L and ϵ represent the nominal luminosity and total acceptance times efficiency, respectively.

1606 **6.5.2.2 Uncertainties**

1607 In this analysis, there are six sources of systematic uncertainties on the signal stud-
1608 ied:

1609 δL an uncertainty on the integrated luminosity of the data sample,

1610 $\delta \epsilon$ an uncertainty on the signal efficiency times acceptance,

1611 δt an uncertainty on the gluon-tag efficiency,

1612 δE_{JER} an uncertainty on the jet energy resolution, and

1613 δE_{JES} an uncertainty on the jet energy scale.

1614 δS an uncertainty due to spurious signals.

1615 All these uncertainties are treated as shape uncertainties except for δL which is a normal-
1616 ization uncertainty. These uncertainties are associated to nuisance parameters denoted
1617 by $\alpha_L, \alpha_\epsilon, \alpha_t, \alpha_{E_{\text{JER}}}, \alpha_{E_{\text{JES}}}, \alpha_S$, respectively, and the values of the auxiliary measurements
1618 by $\theta_b, \theta_L, \theta_\epsilon, \theta_t, \theta_{E_{\text{JER}}}, \theta_{E_{\text{JES}}}, \theta_S$, respectively.

1619 **6.5.2.3 Likelihood function definition**

1620 A binned likelihood is used in this analysis. Consider the m_{jj} histogram of $\mathbf{n} =$
1621 (n_1, \dots, n_N) events, the likelihood function without uncertainties is built as:

$$\mathcal{L}(\mu; b_{\text{tot}}, \mathbf{p}_s, \mathbf{p}_b) = \prod_{i=1}^N \frac{(\mu s_i + b_i)^{n_i}}{n_i!} e^{-(\mu s_i + b_i)}, \quad (6.11)$$

1622 where the parameter of interest (POI) μ is the signal strength parameter, b_i is the num-
1623 ber of background events in the i bin, s_i is the number of signal events in the i bin.
1624 Background-only hypothesis corresponding to $\mu = 0$, whereas nominal signal hypoth-
1625 esis corresponding to $\mu = 1$.

1626 The full likelihood function with uncertainties included is defined as:

$$\begin{aligned} \mathcal{L}(\mu; b_{\text{tot}}, \mathbf{p}_s, \mathbf{p}_b, \boldsymbol{\alpha}_s) &= \prod_{i=1}^N \frac{(\mu_i^T)^{n_i}}{n_i!} e^{-\mu_i^T} N_i(\alpha_L; \theta_L, \delta_L) N_i(\alpha_\epsilon; \theta_\epsilon, \delta \epsilon) \\ &\quad \cdot N_i(\alpha_t; \theta_t, \delta E_t) N_i(\alpha_{E_{\text{JER}}}; \theta_{E_{\text{JER}}}, \delta E_{\text{JER}}) \end{aligned} \quad (6.12)$$

$$\cdot \quad N_i(\alpha_{E_{\text{JES}}}; \theta_{E_{\text{JES}}}, \delta E_{\text{JES}}) N_i(\alpha_s; \theta_s, \delta_s), \quad (6.13)$$

1627 where μ_i^T is the total number of expected event in the i bin, which is given by:

$$\mu_i^T = \mu s_i \eta_i^L(\alpha_L) \eta_i^\epsilon(\alpha_\epsilon) \eta_i^t(\alpha_t) \eta_i^{E_{\text{JER}}}(\alpha_{E_{\text{JER}}}) \eta_i^{E_{\text{JES}}}(\alpha_{E_{\text{JES}}}) + b_i. \quad (6.14)$$

1628 The parameter $\eta^s(\alpha_s)$ are response functions for uncertainty s , and the subsidiary mea-
1629 surements are constrained by the $N(\alpha; \theta, \delta)$ functions.

1630 In this analysis, constraint functions are built from standard Gaussians, together
1631 with uncertainties that mapped in the response functions. Luminosity uncertainty is
1632 fitted by a log-normal response function, the JER and JES uncertainties are given by
1633 Gaussian and asymmetric response functions, respectively. For each bin, a vertical inter-
1634 polation strategy called piece-wise linear method is used independently. In the case of
1635 the asymmetric error, the polynomial interpolation and exponential extrapolation method
1636 is used.

1637 The parameters $(\mu, N_b, p_s, p_b, \alpha_L)$ are fixed from the fit to data (pseudo-data) and
1638 are common for all bins, whereas parameters $(\alpha_\epsilon, \alpha_t, \alpha_{E_{\text{JER}}}, \alpha_{E_{\text{JES}}}, \alpha_s)$ are different from
1639 bin to bin.

1640 For simplicity in notation, the 18 nuisance parameters are written as the vector α ,
1641 where six of them have corresponding uncertainties. The simplified likelihood function
1642 is written as:

$$\mathcal{L}(\mu; \alpha) = \prod_{i=1}^N \frac{[\mu_i^T(\mu, \alpha)]^{n_i}}{n_i!} e^{-\mu_i^T(\mu, \alpha)} \prod_{s=1}^6 G_{i,s}(\alpha_s). \quad (6.15)$$

1643 6.5.2.4 Statistical Method

1644 A hypothesis test is used for estimating the compatibility between data and a theo-
1645 retical hypothesis, where the pseudo datasets are generated according to a given hypoth-
1646 esis, and compared to the tested dataset in terms of a test statistic.

1647 The procedure is demonstrated as follows: first, the agreement between the col-
1648 lected data and the null hypothesis is evaluated through a hypothesis test. The null hy-
1649 pothesis ($\mu = 0$) posits that only the SM background is present. If the data does not
1650 exhibit any substantial excess under this hypothesis test, the subsequent step involves es-
1651 tablishing an exclusion limit for the targeted signal model on the resonance cross section
1652 for m_{jj} . In this scenario, the hypothesis transforms into a signal + background assump-

1653 tion, leading to the construction of a test statistic based on the signal + background PDF
 1654 of the discriminating variable.

1655 The statistical measurement's p-value serves as a quantification of the degree of
 1656 agreement or discrepancy between a hypothesis and the observed data. Mathematically,
 1657 it represents the integral of the distribution of the test statistic from the value obtained
 1658 for the dataset in question to infinity. This value characterizes the probability of achiev-
 1659 ing the observed outcomes assuming the null hypothesis. A lower p-value indicates a
 1660 higher degree of statistical significance for the observed incompatibility. For instance,
 1661 if the p-value of the data is below 0.05, it signifies that the likelihood of the observed
 1662 data aligning with the hypothesis is less than 5%. This prompts the assertion that the
 1663 hypothesis can be excluded at the 95% confidence level (CL).

1664 **6.5.2.5 Test statistic and p-value definitions**

1665 A binned maximum likelihood (ML) fitting method is used to extract the signal,
 1666 together with profile likelihood ratio test statistic. The test statistics used for claiming a
 1667 positive signal is defined as:

$$q_0 = \begin{cases} -2 \ln \frac{\mathcal{L}(0, \hat{\alpha}(0))}{\mathcal{L}(\hat{\mu}, \hat{\alpha})} & \hat{\mu} \geq 0, \\ 0 & \hat{\mu} < 0. \end{cases} \quad (6.16)$$

1668 and the test statistic used for evaluating the upper limits is given as:

$$\tilde{q}_\mu = \begin{cases} -2 \ln \frac{\mathcal{L}(\mu, \hat{\alpha}(\mu))}{\mathcal{L}(0, \hat{\alpha}(0))} & \hat{\mu} < \mu, \\ -2 \ln \frac{\mathcal{L}(\mu, \hat{\alpha}(\mu))}{\mathcal{L}(\hat{\mu}, \hat{\alpha})} & 0 \leq \hat{\mu} \leq \mu, \\ 0 & \hat{\mu} > \mu. \end{cases} \quad (6.17)$$

1669 where the parameter μ represents the signal strength associated with the hypothesis being
 1670 tested. The maximum likelihood (ML) estimators that optimize the likelihood function
 1671 \mathcal{L} without constraints are referred to as $\hat{\mu}$ for the signal strength and $\hat{\alpha}$ for the other pa-
 1672 rameters. The parameter $\hat{\alpha}$ represents the conditional ML estimator of α that maximizes
 1673 \mathcal{L} while considering a specific value of μ .

1674 The p-value corresponding to the background-only hypothesis is expressed as:

$$p_0 = \int_{q_{0,\text{obs}}}^{\infty} f(q_0|0) dq_0. \quad (6.18)$$

1675 The values of \tilde{q}_μ are calculated for different values of μ by fitting a dataset where

1676 the pseudo data is represented by μ' . This calculation of \tilde{q}_μ is conducted for each pseudo
 1677 dataset at various selected signal mass points, resulting in a distribution of \tilde{q}_μ denoted as
 1678 $f(\tilde{q}_\mu | \mu = \mu')$. As a result, a p-value for the tested dataset is determined based on this
 1679 distribution:

$$p_{\mu'} = \int_{\tilde{q}'_{\mu,\text{obs}}}^{\infty} f(\tilde{q}_\mu | \mu = \mu') dq_\mu, \quad (6.19)$$

1680 the term $\tilde{q}'_{\mu,\text{obs}}$ represents the computed value of the test statistic based on the dataset
 1681 being tested. These p-values are also referred to as p_{s+b} , which signifies that they are
 1682 associated with the signal plus background hypothesis.

1683 6.5.2.6 Generation of pseudo-data

1684 The PDF of a certain model is used for generating the pseudo datasets. Signal +
 1685 background pseudo datasets are utilized to estimate the observed confidence level (CL) of
 1686 a signal + background hypothesis, while background-only pseudo datasets are employed
 1687 for expected CL estimations.

1688 During the generation of pseudo datasets, all parameters in the PDF are set to their
 1689 nominal values. The expected event counts in each bin follow a Poisson distribution.
 1690 Nuisance parameters (NPs), which represent systematic uncertainties, are treated ac-
 1691 cording to the "unconditional ensemble" approach: for each pseudo dataset, the values
 1692 of α_i (associated with the NPs) are drawn from their respective constraint terms, and
 1693 these values are used in both the likelihood \mathcal{L} and the computation of \tilde{q}_μ .

1694 6.5.2.7 Definition of exclusion limit

1695 The data is interpreted by the modified frequentest method (CL_s method), where
 1696 p-value is modified to take into account downward background fluctuations and quoted
 1697 as CL_s . The definition of CL_s is:

$$CL_s = \frac{p_{s+b}}{1 - p_b}, \quad (6.20)$$

1698 where $p_{b(s+b)}$ is the integrated value of the background-only (signal + background) dis-
 1699 tribution from zero to $\tilde{q}_\mu^{\text{obs}}$. Thus $1 - p_b$ is also referred to as the confidence level of the
 1700 background-only hypothesis (CL_b). The CL_s limit claims exclusion at 95% CL when
 1701 $CL_s = 0.05$.

1702 **6.5.2.8 Implementation**

1703 The statistical approach employed in this analysis differs slightly from previous
 1704 dijet analyses and aligns with the current trigger-level analysis. In previous approaches,
 1705 a background model devoid of NPs was fitted to the data, and the resulting background
 1706 fit parameters were employed (and held constant) in subsequent likelihood fits involving
 1707 nuisance parameters. However, in this analysis, the background fit parameters are treated
 1708 as unconstrained NPs within the complete likelihood framework used in all fits.

1709 To create the RooFit workspaces, the XML Analytic Workspace Builder is utilized.
 1710 The xRooFit tool processes these workspaces and performs operations like setting limits,
 1711 among others, using classes from the RooFit and RooStats libraries.

1712 **6.5.3 Background Estimation**

1713 In the resonant search the SM background of the m_{jj} spectrum is established
 1714 through a functional fitting procedure applied to the data. Refs. [101, 102, 103, 104,
 1715 105, 106]) have found that a parametric function of the form

$$f(x) = p_1(1-x)^{p_2}x^{p_3+p_4 \ln x + p_5 (\ln x)^2}, \quad (6.21)$$

1716 where $x \equiv m_{jj} / \sqrt{s}$, accurately describes dijet mass distribution predicted by leading and
 1717 next-to-leading-order QCD Monte Carlo. In the ATLAS Run 2 analysis with 139.0 fb^{-1}
 1718 of data [107, 96], the four parameter version of the function ($p_5 = 0$) was found to
 1719 sufficiently described the data. The introduction of gluon tagging may require more
 1720 parameters to properly describe the full invariant mass spectrum.

1721 To avoid introducing any potential bias due to the selection of a specific background
 1722 function, an alternative functional form is employed. This alternative form is inspired by
 1723 the one used by the UA2 experiment [108, 109] when observing the decay of W and Z
 1724 bosons into two jets, followed by a subsequent search.

$$f(x) = p_1 x^{p_2} \exp(p_3 x + p_4 x^2). \quad (6.22)$$

1725 **6.5.4 Analysis Strategy**

1726 The analysis begins with the utilization of skimmed ntuples, which are the result
 1727 of applying the event selection criteria outlined in Section 6.4.3. These ntuples serve as

1728 the basis for generating pseudo-data using the background-only model. Subsequently,
 1729 a 4-parameter ($p_5 = 0$) fit function described by Equation 6.21 is employed to fit this
 1730 pseudo-data. The fit to the data is deemed satisfactory if it meets the following criterion:

- 1731 • Global χ^2 p -value > 0.05

1732 If the conditions mentioned above are satisfied, the background is chosen for the
 1733 purpose of upper limit estimations. Conversely, if the criteria are not met, the 5-parameter
 1734 version of Equation 6.21 is employed for background fitting and is subjected to the same
 1735 selection criterion. If the fit using the 5-parameter function also fails to meet the cri-
 1736 teria, the analysis reduces the range of the window and repeats the fitting process with
 1737 the 5-parameter function to see if a satisfactory fit can be achieved. If this attempt still
 1738 does not meet the criteria, the analysis switches to an alternative option for generating
 1739 pseudo-data. Once a fit satisfying the criteria is obtained, the fit function undergoes var-
 1740 ious validation tests to ensure the appropriateness of the fit strategy. The flowchart of
 1741 Figure 6.72 shows the analysis strategy.

1742 **6.5.5 Spurious Signal Tests**

1743 The spurious signal test is designed to estimate the difference between the signal
 1744 yields from the fit and the expected signal yields that given by fitting a known template
 1745 signal model on a smooth background distribution. Such difference is considered as fit
 1746 bias and defined as S_{spur} :

$$S_{\text{spur}} = S_{\text{fit}} - S_{\text{template}} \quad (6.23)$$

1747 It is crucial to verify the stability of the fit when applied to a background-only
 1748 distribution. In this context, no signal is intentionally introduced into the yields, ensuring
 1749 that the extracted number of signal events remains zero. In the spurious signal test, S_{spur}
 1750 is determined by fitting a model comprising both signal and background components
 1751 onto a background-only template. The corresponding uncertainty from the fit is denoted
 1752 as σ_{fit} . Both the spurious signal S_{spur} and its associated uncertainty σ_{fit} are expected to be
 1753 consistent with zero.

1754 The estimation of the spurious signal is consequently conducted through these pseudo-
 1755 experiments. The mean value across all experiments is calculated, and a total of 100
 1756 pseudo-experiments have been employed. For each individual signal hypothesis, the

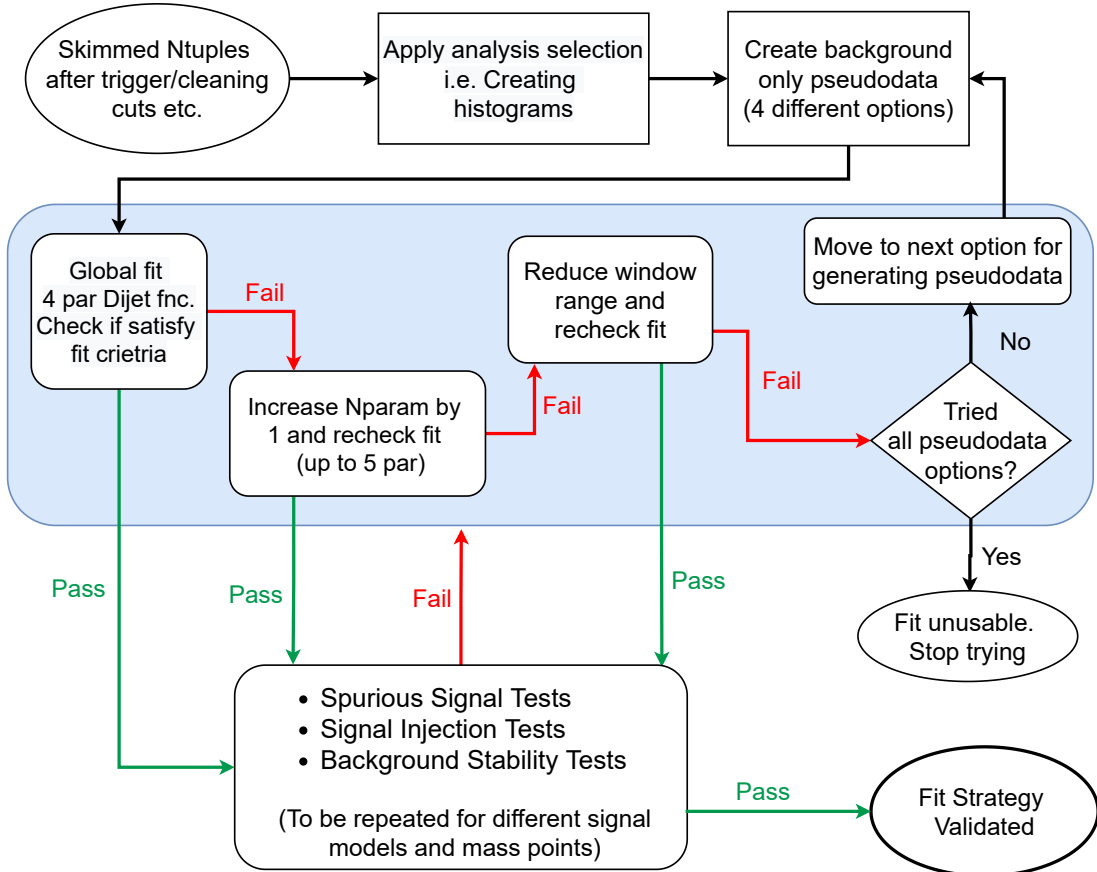


Figure 6.72 Analysis top-level flowchart.

1757 assessment of spurious signals is conducted at various mass points. This is done in
 1758 individually for each signal hypothesis and at each mass point. The outcomes of the
 1759 model-independent tests for Gaussian signals, considering different masses and widths,
 1760 are consolidated in Table 6.33 for the 1 gluon-tagged category and in Table 6.34 for the
 1761 2 gluon-tagged category.

1762 Following the recommendations of the Statistical PUB Note [110], the spurious
 1763 signal is required to be

$$S_{\text{spur}} < (20\% - 50\%) \sigma_{\text{fit}} \quad (6.24)$$

1764 The idea criteria is when the spurious signal satisfy: $S_{\text{spur}} < 30\% \sigma_{\text{fit}}$, but can be
 1765 loosen up to 50% σ_{fit} . Most of the tested mass points and widths satisfy the spurious
 1766 signal criteria.

Mass TeV	Width percentage [%]	Median ± Rms S_{spurious} ± Uncertainty	Ratio $S_{\text{spurious}}/\text{Uncertainty}$
2	5	0.19 2 ± 802.85 2	2.36E-042
2	10	3.35 2 ± 1313.792	2.55E-032
2	15	154.92 2 ± 1666.6 2	0.093 2
3	5	1.76 2 ± 249.13 2	7.06E-032
3	10	82.55 2 ± 520.85 2	0.158 2
3	15	344.74 2 ± 803.85 2	0.429 2
4	5	48.42 2 ± 112.34 2	0.431 2
4	10	115.89 2 ± 200.83 2	0.577 2
4	15	2.02 2 ± 242.15 2	8.34E-032
5	5	0.021 2 ± 31.77 2	6.61E-042
5	10	0.012 2 ± 31.96 2	3.75E-042
5	15	0.006 2 ± 18.98 2	3.16E-042
6	5	7.82E-042 ± 5.54 2	1.41E-042
6	10	2.84E-042 ± 5.93 2	4.79E-052
6	15	3.62E-042 ± 5.79 2	6.25E-052
7	5	8.65E-042 ± 2.66 2	3.25E-042
7	10	1.6E-04 2 ± 2.59 2	6.18E-052
7	15	8.34E-052 ± 2.71 2	3.08E-052

Table 6.33 Spurious Signal tests using Gaussian signals for 1 gluon tagged category.

Mass TeV	Width percentage [%]	Median ± Rms $S_{\text{spurious}} \pm \text{Uncertainty}$	Ratio $S_{\text{spurious}}/\text{Uncertainty}$
2	5	179.84 2 ± 635.08 2	0.283 2
2	10	757.07 2 ± 1265.99 2	0.598 2
2	15	1666.24 2 ± 2126.08 2	0.784 2
3	5	1.83E-032 ± 85.31 2	2.14E-05 2
3	10	0.27 2 ± 125.63 2	2.15E-03 2
3	15	0.021 2 ± 113.74 2	1.85E-04 2
4	5	1.91E-032 ± 25.6 2	7.46E-05 2
4	10	3.55E-032 ± 38.68 2	9.18E-05 2
4	15	1.50E-032 ± 27.01 2	5.55E-05 2
5	5	2.72E-042 ± 7.13 2	3.81E-05 2
5	10	9.99E-052 ± 5.57 2	1.79E-05 2
5	15	2.1E-042 ± 4.72 2	4.45E-05 2
6	5	1.37E-042 ± 1.92 2	7.14E-05 2
6	10	1.47E-042 ± 3.25 2	4.52E-05 2
6	15	6.49E-052 ± 2.59 2	2.51E-05 2
7	5	1.88E-042 ± 1.19 2	1.58E-04 2
7	10	1.17E-042 ± 1.17 2	1.0E-04 2
7	15	7.83E-052 ± 1.20 2	6.53E-05 2

Table 6.34 Spurious Signal tests using Gaussian signals for 2 gluon tagged category.

6.5.6 Fit Stability Tests

The fit stability tests are employed to assess the behaviour of the background fit function under different scenarios: when applied to the background-only template and the signal + background template. A comparison is made between the fit results obtained from these two templates. Ideally, the background fit function should yield consistent outcomes in both cases. The results of these fit stability tests are presented in Table 6.35 through Table 6.36, encompassing various signal strengths and mass points.

Notably, the background estimation derived from the signal + background fit (B_1) aligns with the background estimation obtained from the background-only fit (B_2), indicating good agreement between the two approaches.

Mass (TeV)	Width (percentage)	Signal Strength	B_1 from S+B fit	B_2 from B-only fit
			Mean \pm Rms	Mean \pm Rms
2	5	1	20062716.452 \pm 4370.572	20064025.612 \pm 4003.072
2	5	3	20063730.272 \pm 4882.092	20067248.182 \pm 4003.142
2	5	5	20062961.532 \pm 4521.622	20070470.902 \pm 4003.362
5	5	1	20062414.492 \pm 4005.802	20062458.642 \pm 4003.052
5	5	3	20062420.852 \pm 4002.942	20062547.112 \pm 4003.092
5	5	5	20062420.962 \pm 4002.822	20062635.822 \pm 4003.252
5	10	1	20062435.182 \pm 4010.372	20062483.502 \pm 4002.872
5	10	3	20062448.752 \pm 4007.222	20062622.262 \pm 4002.952
5	10	5	20061413.122 \pm 3682.052	20062761.082 \pm 4003.122
7	5	1	20062420.382 \pm 4002.682	20062420.292 \pm 4002.982
7	5	3	20062422.562 \pm 4002.862	20062432.082 \pm 4003.082
7	5	5	20062422.862 \pm 4002.982	20062444.092 \pm 4003.202

Table 6.35 Fit Stability tests using Gaussian signals for 1 gluon tagged category.

Mass (TeV)	Width (percentage)	Signal Strength	B_1 from S+B fit		B_2 from B-only fit	
			Mean ± Rms	Mean ± Rms	Mean ± Rms	Mean ± Rms
2	5	1	3901512.922 ± 2163.272	3902240.712 ±	2048.042	
2	5	3	3901530.762 ± 2166.982	3903253.552 ±	2047.372	
2	5	5	3901621.902 ± 2291.012	3905032.952 ±	2050.682	
5	5	1	3901529.752 ± 2049.312	3901559.922 ±	2046.182	
5	5	3	3901528.522 ± 2049.152	3901589.412 ±	2044.932	
5	5	5	3901533.992 ± 2047.482	3901621.882 ± 3901586.682		
5	10	1	3901536.862 ± 2047.402	3901566.442 ±	2048.232	
5	10	3	3901535.712 ± 2054.622	3901616.492 ±	2050.262	
5	10	5	3901538.472 ± 2049.542	3901670.562 ±	2047.942	
7	5	1	3901531.272 ± 2047.302	3901538.452 ±	2049.162	
7	5	3	3901540.722 ± 2068.732	3901542.752 ±	2048.462	
7	5	5	3901533.132 ± 2052.642	3901540.092 ±	2048.942	

Table 6.36 Fit Stability tests using Gaussian signals for 2 gluon tagged category.

1777 **6.6 Systematic uncertainties**

1778 **6.6.1 String resonance systematic uncertainties**

1779 As described in Section 4.2, JES and JER systematic uncertainties are considered
1780 for the String resonances. In this study, three NPs from the JES and 7 NPs from the JER
1781 are studied on the normalised template shapes.

1782 The impact from JES on the signal template is evaluated by comparing the nominal
1783 distribution to the distribution from each JES NP. The impact from JER on the signal
1784 template is estimated by examining the shift in the RMS (or standard deviation) of the
1785 distribution from each JER NP. Such signal shifts are parameterised by fitting a Gaus-
1786 sian function to the most significant bins surrounding the maximum mean value of the
1787 distribution.

1788 Figure 6.73 shows an example for the $M_s = 8$ TeV signal sample. This histogram
1789 exemplifies one of the systematic variations employed in the subsequent limit calcula-
1790 tion. Among the various systematic sources, GroupedNP_3 emerges as having the most
1791 substantial impact, leading to a significant shift in the signal mean. Across signal samples
1792 of diverse masses and widths, the reconstructed peak of the signal demonstrates a shift
1793 towards lower values in comparison to the generated peak, amounting to approximately
1794 $0.92 \times M_s$. It is important to note that this shift is present even before accounting for the
1795 JES or JER systematic uncertainties.

1796 In Figure 6.74, the proportional shift in the mean of the m_{jj} distribution attributed
1797 to the JES uncertainty and the relative change in RMS of the m_{jj} distribution due to the
1798 JER uncertainty are depicted. While all the NPs are independently incorporated in the
1799 limit computations, this illustration presents a combined display of the three JES mean
1800 shifts in quadrature and the seven JER resolution differences in quadrature.

1801 The alterations in signal acceptance from the inclusion of JES and JER uncertainties
1802 are combined in quadrature and determined to be less than 0.06%. Such small uncertainty
1803 can be ignored for the signal acceptance.

1804 The shifts in the mean of the signal distributions, resulting from the inclusion of
1805 JES uncertainty, are primarily driven by GroupedNP_3 and amount to less than 4%.
1806 Conversely, the alterations in the RMS of the signal distributions following the incor-
1807 poration of JER uncertainty remain below 1.2%. Among the seven values combined in
1808 quadrature, none exhibit a dominant influence. Notably, the JER uncertainty emerges as

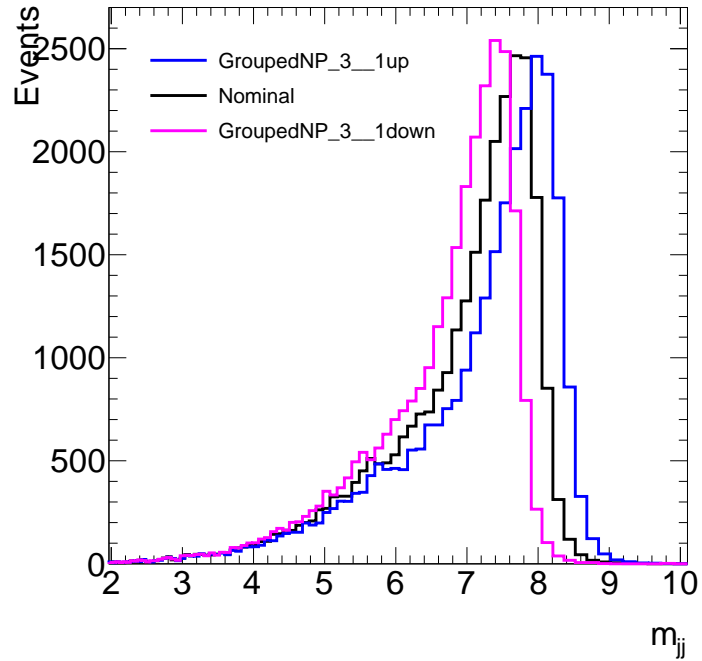


Figure 6.73 m_{jj} distribution for the $M_s = 8$ TeV string sample (nominal). Also shown are the distributions using the jet energy scale GroupedNP_3 one standard deviation up and down systematic uncertainties.

¹⁸⁰⁹ the most substantial source of uncertainty for the lowest M_s signal sample.

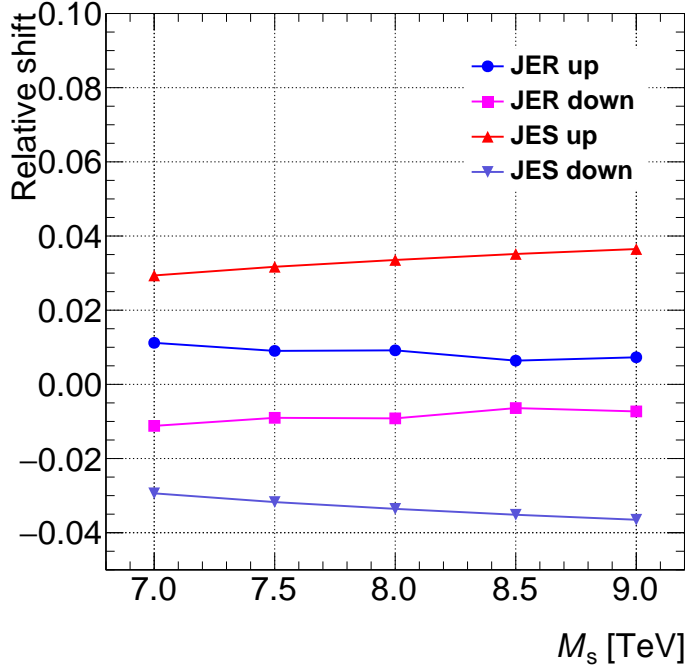


Figure 6.74 Relative shift in the mean of the m_{jj} distributions for each string sample due to jet energy scale uncertainty, and relative change in the RMS of the m_{jj} distributions for each string sample due to the jet energy resolution uncertainty. The changes due to each nuisance parameter group are added in quadrature.

1810 6.6.2 q/g tagging Systematics

1811 6.6.2.1 Pure MC Systematics

1812 Indeed, obtaining uncertainties for a q/g tagger built upon track multiplicity poses
 1813 challenges, particularly in the higher p_T range. This difficulty is partly attributed to the
 1814 limited statistics available beyond 1 TeV, where fewer gluon-jets are present due to their
 1815 tendency to be produced at lower masses compared to quark-jets. Consequently, an issue
 1816 arises in equations that necessitate the average number of tracks in quark- or gluon-jets to
 1817 facilitate calculations. The scarcity of data points at higher p_T values hampers the robust
 1818 estimation of these averages, contributing to the uncertainty challenge in this context.

1819 The determination of the fraction of jets classified as quark- or gluon-initiated jets
 1820 is accomplished through the ratio f_q^f/f_g^c , where the superscript f (c) designates the jet
 1821 with the higher (lower) η value in simulated dijet events. These fractions are derived by
 1822 convolving parton distribution functions with matrix element calculations. The number
 1823 of charged tracks events in the jet with higher η can be described by the following system

1824 of equations [47]:

$$\langle n_{\text{charged}}^f \rangle = f_q^f \langle n_{\text{charged}}^q \rangle + f_g^f \langle n_{\text{charged}}^g \rangle \quad \langle n_{\text{charged}}^c \rangle = f_q^c \langle n_{\text{charged}}^q \rangle + f_g^c \langle n_{\text{charged}}^g \rangle. \quad (6.25)$$

1825 These equations require two samples with different fractions of quark- and gluon-
1826 jets. While theoretically valid even at high p_T values, their applicability diminishes in the
1827 high p_T regime due to the exceedingly small fractions of gluon jets. Notably, the main
1828 sources of uncertainty stem from discrepancies in the MC modelling and the challenges
1829 associated with reconstructing charged tracks within jets. This is especially relevant as
1830 the separation between tracks is comparable to the resolution of the detector. Conse-
1831 quently, the efficiency of the tagger relies on the accurate resolution of tracks for precise
1832 N_{trk} determination, which in turn is constrained by available statistics.

1833 Their systematic uncertainty can be estimated by using pure MC simulations and
1834 is expected to be substantial, yet smaller than that obtained from data at the edges of
1835 the mass range. This technique is particularly effective where statistics are not limited,
1836 such as in the central region of the p_T distribution. Such an approach has proven to be
1837 the optimal choice. To extend the uncertainties into the higher p_T regime, particle-level
1838 effects and MC reconstruction effects are incorporated. These uncertainties pertain to
1839 "in-situ" considerations, making it reasonable to employ them during an extrapolation
1840 procedure.

1841 The procedure is performed at constant p_T ranges, as N_{trk} depends only on p_T and
1842 the parton type that initiating jets, uncertainties can be computed by comparing the dis-
1843 tribution of N_{trk} in bins of jet p_T , which generated from different simulation models.
1844 Thus different type of MC generators could introduce underlying uncertainties to the re-
1845 sults. Details on different types of uncertainties and the samples used to estimate them
1846 are described in Section 5.7. Six working points (10%, 25%, 40%, 50%, 60% and 75%)
1847 are provided for fixed efficiency curves.

1848 **6.7 Results**

1849 The untagged $y^* < 0.8$, 1-g tagged $y^* < 0.6$ and 2-g tagged $y^* < 0.8$ model-independent
1850 Gaussian limits are shown in fig [6.75](#), [6.76](#) and [6.77](#) respectively, for Gaussians with
1851 width equal to 0, 3, 5, 7, 10 and 15% of their peak position, without systematics in-
1852 cluded.

Search for new phenomena in dijet events

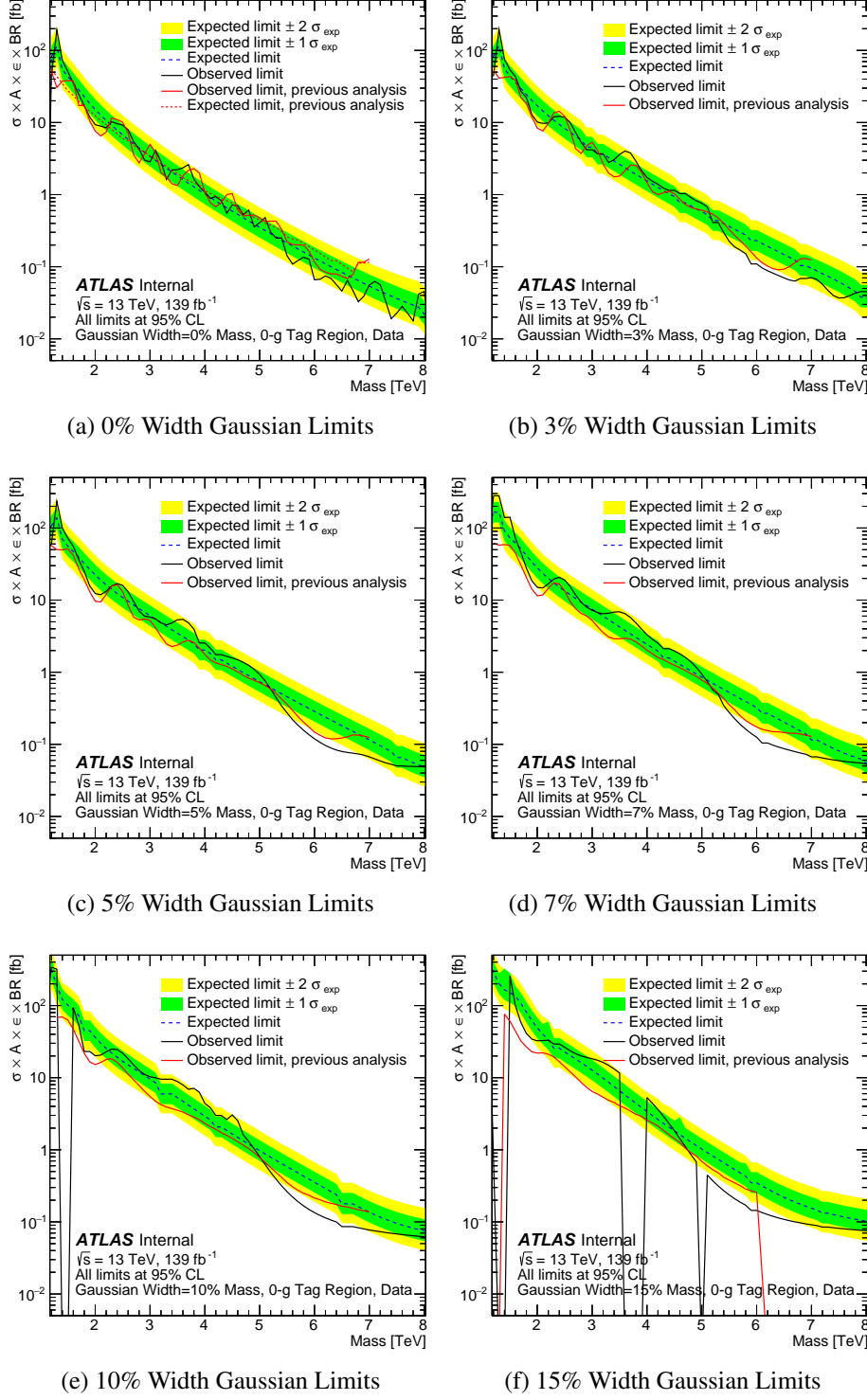


Figure 6.75 Model-independent limits set in the untagged $y^* < 0.8$ Signal Region using Gaussian resonances of varying widths from 0% to 15% of their peak position without systematics included using the full 139fb^{-1} Run-2 dataset.

Search for new phenomena in dijet events

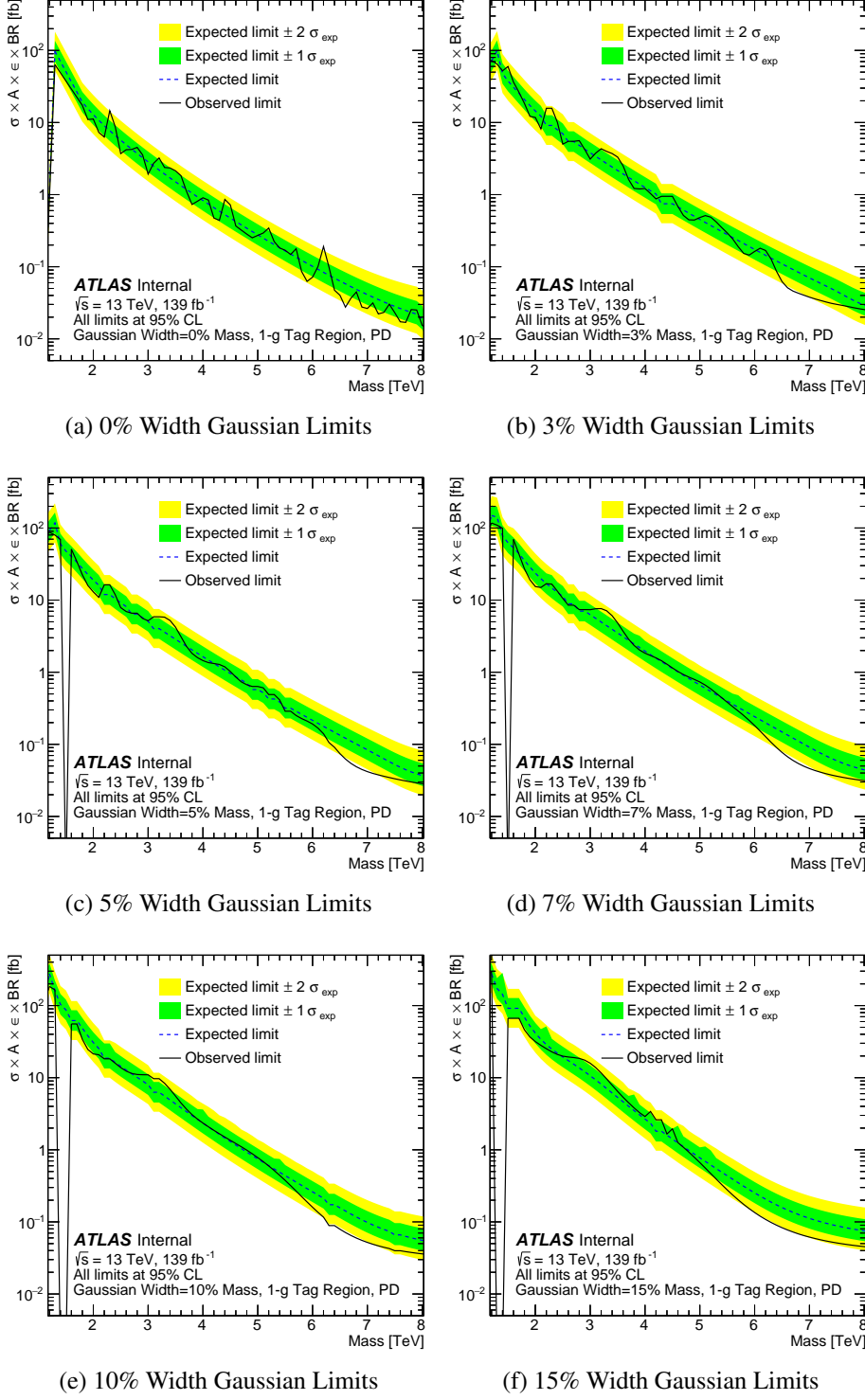


Figure 6.76 Model-independent limits set in the 1-g tagged $y^* < 0.6$ Signal Region using Gaussian resonances of varying widths from 0% to 15% of their peak position without systematics included using the full 139fb^{-1} Run-2 dataset.

Search for new phenomena in dijet events

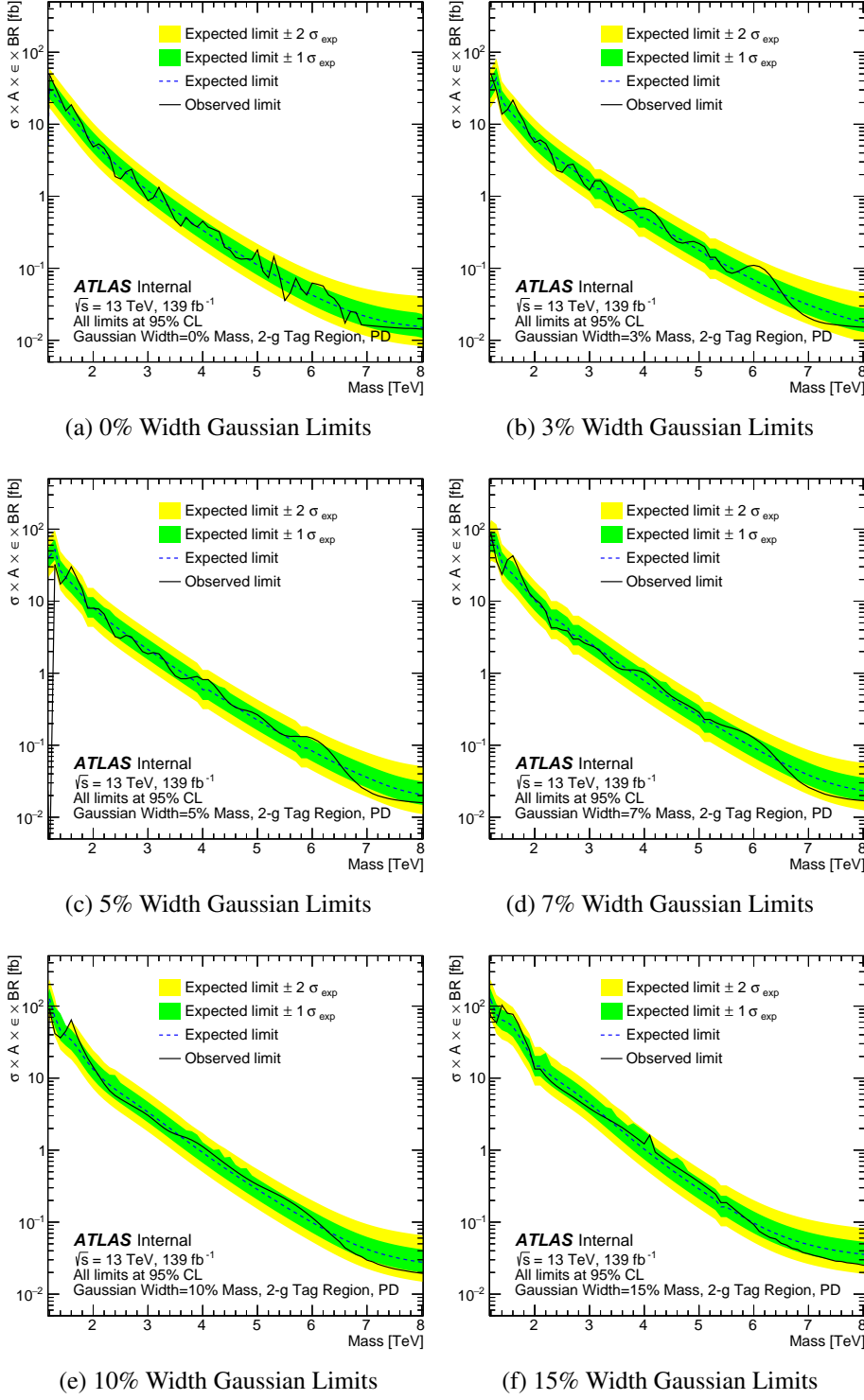


Figure 6.77 Model-independent limits set in the 2-g tagged $y^* < 0.8$ Signal Region using Gaussian resonances of varying widths from 0% to 15% of their peak position without systematics included using the full 139fb^{-1} Run-2 dataset.

1853

7 Conclusions

1854 From 2015 to 2018, the proton-proton collision at the LHC have achieved an unprece-
1855 dented centre-of-mass energy of $\sqrt{s} = 13$ TeV, with a total integrated luminosity of 140
1856 fb^{-1} that have been recorded by the ATLAS experiment. Such huge amount of collision
1857 data allow scientists test models beyond the SM in a more efficient way, leading a deeper
1858 understanding of physics beyond the SM.

1859 This thesis presents the search for new resonances that potentially decay into a pair
1860 of jets using the data collected by the ATLAS detector during 2015-2018. Resonances
1861 predicted by the BSM can decay into quarks and/or gluons, by introducing jet taggers,
1862 the sensitivity of the search could be significantly increased. This study leverages the
1863 extensive dataset recorded between 2015 and 2018 to extend the taggers' applicability
1864 to high-energy jets. Two distinct jet tagging methods are explored: a tagger centred on
1865 the charged-particle jet constituent multiplicity (N_{trk}), and a BDT-based tagger, which
1866 integrates various individual jet substructure observables.

1867 The matrix method is adopted to estimate the distribution shapes of the tagging
1868 variables for quark- and gluon-jets. This entails combining information from samples
1869 enriched with quark- and gluon-jets, acquired from a selection of dijet events charac-
1870 terized by jet p_{T} ranging from 500 GeV to 2 TeV. The considered variables exhibit a
1871 satisfactory agreement with the MC simulations, with discrepancies relative to data mea-
1872 surements being less than 25% across various defined regions.

1873 The BDT-tagger demonstrates superior performance over the N_{trk} -only tagger in
1874 distinguishing quark-jets from gluon-jets within the jet p_{T} range of 500 GeV to 1200
1875 GeV. Above this range, the performance of the two taggers becomes comparable. The
1876 evaluation of tagger performance differences between data and MC samples is facilitated
1877 through the data-to-MC SFs. Four working points of 50%, 60%, 70%, 80% together with
1878 all systematics are provided so that analyses can use it based on their own interest. These
1879 factors are measured across varying jet- p_{T} intervals, exhibiting a range from 0.92 to 1.02,
1880 with a cumulative uncertainty of approximately 20%. The primary contributor to this
1881 uncertainty stems from divergent modelling choices within MC simulations, constituting
1882 approximately 18% for both taggers. To account for variations between different MC
1883 generators, MC-to-MC SFs are also presented, ranging from 0.9 to 1.1 for the majority
1884 of MC samples.

Conclusions

1885 The q/g taggers developed in this study and the associated measurement of their SFs
1886 hold relevance for various analyses. These applications encompass SM measurements
1887 that rely on accurate jet origin identification, as well as BSM physics searches that can
1888 capitalize on heightened sensitivity to the presence of new particles. This thesis performs
1889 the searches on m_{jj} spectrum. Benchmark models String, graviton and QBH are tested,
1890 as well as model-independent Gaussians. Because no significant excess in data are found,
1891 a upper limit is set to each model.

1892

REFERENCES

- 1893 [1] ATLAS Collaboration. “Search for the Standard Model Higgs boson produced
1894 by vector-boson fusion and decaying to bottom quarks in $\sqrt{s} = 8$ TeV pp colli-
1895 sions with the ATLAS detector”. In: *JHEP* 11 (2016), p. 112. DOI: [10.1007/JHEP11\(2016\)112](https://doi.org/10.1007/JHEP11(2016)112). arXiv: [1606.02181 \[hep-ex\]](https://arxiv.org/abs/1606.02181).
- 1897 [2] CMS Collaboration. “Electroweak production of two jets in association with a Z
1898 boson in proton-proton collisions at $\sqrt{s}= 13$ TeV”. In: *Eur. Phys. J. C* 78 (2018),
1899 p. 589. DOI: [10.1140/epjc/s10052-018-6049-9](https://doi.org/10.1140/epjc/s10052-018-6049-9). arXiv: [1712.09814 \[hep-ex\]](https://arxiv.org/abs/1712.09814).
- 1901 [3] ATLAS Collaboration. “Search for diboson resonances with boson-tagged jets
1902 in pp collisions at $\sqrt{s}= 13$ TeV with the ATLAS detector”. In: *Phys. Lett. B*
1903 777 (2018), p. 91. DOI: [10.1016/j.physletb.2017.12.011](https://doi.org/10.1016/j.physletb.2017.12.011). arXiv:
1904 [1708.04445 \[hep-ex\]](https://arxiv.org/abs/1708.04445).
- 1905 [4] Lyndon Evans and Philip Bryant. “LHC Machine”. In: *JINST* 3 (2008), S08001.
1906 DOI: [10.1088/1748-0221/3/08/S08001](https://doi.org/10.1088/1748-0221/3/08/S08001).
- 1907 [5] CMS Collaboration. “Study of quark and gluon jet substructure in Z+jet and
1908 dijet events from pp collisions”. In: *JHEP* 01 (2022), p. 188. DOI: [10.1007/JHEP01\(2022\)188](https://doi.org/10.1007/JHEP01(2022)188). arXiv: [2109.03340 \[hep-ex\]](https://arxiv.org/abs/2109.03340).
- 1910 [6] CMS Collaboration. *Performance of quark/gluon discrimination using pp colli-*
1911 *sion data at $\sqrt{s} = 8$ TeV.* CMS-PAS-JME-13-002. 2013. URL: <https://cds.cern.ch/record/1599732>.
- 1913 [7] CMS Collaboration. “Measurements of jet charge with dijet events in pp colli-
1914 *sions at $\sqrt{s}= 8$ TeV”.* In: *JHEP* 10 (2017), p. 131. DOI: [10.1007/JHEP10\(2017\)131](https://doi.org/10.1007/JHEP10(2017)131). arXiv: [1706.05868 \[hep-ex\]](https://arxiv.org/abs/1706.05868).
- 1916 [8] CMS Collaboration. “Studies of jet mass in dijet and W/Z + jet events”. In: *JHEP*
1917 05 (2013), p. 090. DOI: [10.1007/JHEP05\(2013\)090](https://doi.org/10.1007/JHEP05(2013)090). arXiv: [1303.4811 \[hep-ex\]](https://arxiv.org/abs/1303.4811).

REFERENCES

- 1919 [9] CMS Collaboration. “Measurement of the jet mass in highly boosted $t\bar{t}$ events
1920 from pp collisions at $\sqrt{s} = 8$ TeV”. In: *Eur. Phys. J. C* 77.7 (2017), p. 467.
1921 DOI: [10.1140/epjc/s10052-017-5030-3](https://doi.org/10.1140/epjc/s10052-017-5030-3). arXiv: [1703.06330](https://arxiv.org/abs/1703.06330)
1922 [[hep-ex](#)].
- 1923 [10] CMS Collaboration. “Measurement of jet substructure observables in $t\bar{t}$ events
1924 from proton-proton collisions at $\sqrt{s} = 13$ TeV”. In: *Phys. Rev. D* 98 (2018),
1925 p. 092014. DOI: [10.1103/PhysRevD.98.092014](https://doi.org/10.1103/PhysRevD.98.092014). arXiv: [1808.07340](https://arxiv.org/abs/1808.07340)
1926 [[hep-ex](#)].
- 1927 [11] CMS Collaboration. “Measurements of the differential jet cross section as a func-
1928 tion of the jet mass in dijet events from proton-proton collisions at $\sqrt{s} = 13$ TeV”.
1929 In: *JHEP* 11 (2018), p. 113. DOI: [10.1007/JHEP11\(2018\)113](https://doi.org/10.1007/JHEP11(2018)113). arXiv:
1930 [1807.05974](https://arxiv.org/abs/1807.05974) [[hep-ex](#)].
- 1931 [12] A. Altheimer et al. “Jet substructure at the Tevatron and LHC: new results, new
1932 tools, new benchmarks”. In: *J. Phys. G* 39 (2012), p. 063001. DOI: [10.1088/0954-3899/39/6/063001](https://doi.org/10.1088/0954-3899/39/6/063001). arXiv: [1201.0008](https://arxiv.org/abs/1201.0008) [[hep-ph](#)].
- 1934 [13] J. R. Andersen et al. “Les Houches 2015: Physics at TeV Colliders Standard
1935 Model Working Group Report”. In: *9th Les Houches Workshop on Physics at*
1936 *TeV Colliders*. May 2016. arXiv: [1605.04692](https://arxiv.org/abs/1605.04692) [[hep-ph](#)].
- 1937 [14] Andrew J. Larkoski, Jesse Thaler, and Wouter J. Waalewijn. “Gaining (mutual)
1938 information about quark/gluon discrimination”. In: *JHEP* 11 (2014), p. 129. DOI:
1939 [10.1007/JHEP11\(2014\)129](https://doi.org/10.1007/JHEP11(2014)129). arXiv: [1408.3122](https://arxiv.org/abs/1408.3122) [[hep-ph](#)].
- 1940 [15] CDF Collaboration. “Study of jet shapes in inclusive jet production in $p\bar{p}$ col-
1941 lisions at $\sqrt{s} = 1.96$ TeV”. In: *Phys. Rev. D* 71 (2005), p. 112002. DOI: [10.1103/PhysRevD.71.112002](https://doi.org/10.1103/PhysRevD.71.112002). arXiv: [hep-ex/0505013](https://arxiv.org/abs/hep-ex/0505013).
- 1943 [16] OPAL Collaboration. “Experimental properties of gluon and quark jets from a
1944 point source”. In: *Eur. Phys. J. C* 11 (1999), pp. 217–238. DOI: [10.1007/s100520050628](https://doi.org/10.1007/s100520050628). arXiv: [hep-ex/9903027](https://arxiv.org/abs/hep-ex/9903027).
- 1946 [17] CLEO Collaboration. “Comparison of particle production in quark and gluon
1947 fragmentation at $\sqrt{s} \sim 10$ GeV”. In: *Phys. Rev. D* 76 (2007), p. 012005. DOI:
1948 [10.1103/PhysRevD.76.012005](https://doi.org/10.1103/PhysRevD.76.012005). arXiv: [0704.2766](https://arxiv.org/abs/0704.2766) [[hep-ex](#)].

REFERENCES

- 1949 [18] DELPHI Collaboration. “The scale dependence of the hadron multiplicity in
1950 quark and gluon jets and a precise determination of C_A/C_F ”. In: *Phys. Lett. B*
1951 449 (1999), pp. 383–400. DOI: [10.1016/S0370-2693\(99\)00112-4](https://doi.org/10.1016/S0370-2693(99)00112-4).
1952 arXiv: [hep-ex/9903073](https://arxiv.org/abs/hep-ex/9903073).
- 1953 [19] ZEUS Collaboration. “Substructure dependence of jet cross sections at HERA
1954 and determination of alpha(s)”. In: *Nucl. Phys. B* 700 (2004), pp. 3–50. DOI:
1955 [10.1016/j.nuclphysb.2004.08.049](https://doi.org/10.1016/j.nuclphysb.2004.08.049). arXiv: [hep-ex/0405065](https://arxiv.org/abs/hep-ex/0405065).
- 1956 [20] ATLAS Collaboration. *Quark versus Gluon Jet Tagging Using Jet Images with*
1957 *the ATLAS Detector*. ATL-PHYS-PUB-2017-017. 2017. URL: <https://cds.cern.ch/record/2275641>.
- 1958
- 1959 [21] Patrick T. Komiske, Eric M. Metodiev, and Matthew D. Schwartz. “Deep learn-
1960 ing in color: towards automated quark/gluon jet discrimination”. In: *JHEP* 01
1961 (2017), p. 110. DOI: [10.1007/JHEP01\(2017\)110](https://doi.org/10.1007/JHEP01(2017)110). arXiv: [1612.01551](https://arxiv.org/abs/1612.01551)
1962 [[hep-ph](#)].
- 1963 [22] C. Frye, A. J. Larkoski, J. Thaler and K. Zhou. “Casimir meets Poisson: improved
1964 quark/gluon discrimination with counting observables”. In: *JHEP* 09 (2017),
1965 p. 083. DOI: [10.1007/JHEP09\(2017\)083](https://doi.org/10.1007/JHEP09(2017)083). arXiv: [1704.06266](https://arxiv.org/abs/1704.06266) [[hep-ph](#)].
- 1966 [23] J. Gallicchio and M. D. Schwartz. “Quark and Gluon Tagging at the LHC”. In:
1967 *Phys. Rev. Lett.* 107 (2011), p. 172001. DOI: [10.1103/PhysRevLett.107.172001](https://doi.org/10.1103/PhysRevLett.107.172001). arXiv: [1106.3076](https://arxiv.org/abs/1106.3076) [[hep-ph](#)].
- 1969 [24] J. Gallicchio and M. D. Schwartz. “Quark and gluon jet substructure”. In: *JHEP*
1970 04 (2013), p. 090. DOI: [10.1007/JHEP04\(2013\)090](https://doi.org/10.1007/JHEP04(2013)090). arXiv: [1211.7038](https://arxiv.org/abs/1211.7038)
1971 [[hep-ph](#)].
- 1972 [25] Philippe Gras et al. “Systematics of quark/gluon tagging”. In: *JHEP* 07 (2017),
1973 p. 091. DOI: [10.1007/JHEP07\(2017\)091](https://doi.org/10.1007/JHEP07(2017)091). arXiv: [1704.03878](https://arxiv.org/abs/1704.03878) [[hep-ph](#)].
- 1974 [26] Patrick T. Komiske, Eric M. Metodiev, and Jesse Thaler. “An operational defi-
1975 nition of quark and gluon jets”. In: *JHEP* 11 (2018), p. 059. DOI: [10.1007/JHEP11\(2018\)059](https://doi.org/10.1007/JHEP11(2018)059). arXiv: [1809.01140](https://arxiv.org/abs/1809.01140) [[hep-ph](#)].
- 1977 [27] Ignatios Antoniadis, E. Kiritsis, and T.N. Tomaras. “A D-brane alternative to uni-
1978 fication”. In: *Phys. Lett. B* 486 (2000), pp. 186–193. DOI: [10.1016/S0370-2693\(00\)00733-4](https://doi.org/10.1016/S0370-2693(00)00733-4). arXiv: [hep-ph/0004214](https://arxiv.org/abs/hep-ph/0004214).
- 1979

REFERENCES

- 1980 [28] D. Cremades, L.E. Ibanez, and F. Marchesano. “More about the standard model
1981 at intersecting branes”. In: *10th International Conference on Supersymmetry and*
1982 *Unification of Fundamental Interactions (SUSY02)*. Dec. 2002. arXiv: [hep-ph/0212048](#).
- 1984 [29] I. Antoniadis et al. “D-branes and the standard model”. In: *Nucl. Phys. B* 660
1985 (2003), pp. 81–115. DOI: [10.1016/S0550-3213\(03\)00256-6](#). arXiv:
1986 [hep-th/0210263](#).
- 1987 [30] M.B. Green, J.H. Schwarz, E. Witten. *Superstring theory*. Cambridge University
1988 Press, 1987.
- 1989 [31] Schuyler Cullen, Maxim Perelstein, and Michael E. Peskin. “TeV strings and
1990 collider probes of large extra dimensions”. In: *Phys. Rev. D* 62 (2000), p. 055012.
1991 DOI: [10.1103/PhysRevD.62.055012](#). arXiv: [hep-ph/0001166](#).
- 1992 [32] Dieter Lust, Stephan Stieberger, and Tomasz R. Taylor. “The LHC String Hunter’s
1993 Companion”. In: *Nucl. Phys. B* 808 (2009), pp. 1–52. DOI: [10.1016/j.nuclphysb.2008.09.012](#). arXiv: [0807.3333 \[hep-th\]](#).
- 1995 [33] Oskar Klein. “Quantum Theory and Five-Dimensional Theory of Relativity. (In
1996 German and English)”. In: *Z. Phys.* 37 (1926). Ed. by J. C. Taylor, pp. 895–906.
1997 DOI: [10.1007/BF01397481](#).
- 1998 [34] Lisa Randall and Raman Sundrum. “A Large mass hierarchy from a small extra
1999 dimension”. In: *Phys. Rev. Lett.* 83 (1999), pp. 3370–3373. DOI: [10.1103/PhysRevLett.83.3370](#). arXiv: [hep-ph/9905221](#).
- 2001 [35] Stephen Hawking. “Gravitationally Collapsed Objects of Very Low Mass”. In:
2002 *Monthly Notices of the Royal Astronomical Society* 152.1 (Apr. 1971), pp. 75–
2003 78. DOI: [10.1093/mnras/152.1.75](#).
- 2004 [36] S. W. Hawking. “Particle Creation by Black Holes”. In: *Commun. Math. Phys.*
2005 43 (1975). Ed. by G. W. Gibbons and S. W. Hawking, pp. 199–220. DOI: [10.1007/BF02345020](#).
- 2007 [37] ATLAS Collaboration. “The ATLAS Experiment at the CERN Large Hadron
2008 Collider”. In: *JINST* 3 (2008), S08003. DOI: [10.1088/1748-0221/3/08/S08003](#).

REFERENCES

- 2010 [38] B. Abbott et al. “Production and integration of the ATLAS Insertable B-Layer”.
2011 In: *JINST* 13 (2018), T05008. DOI: [10.1088/1748-0221/13/05/T05008](https://doi.org/10.1088/1748-0221/13/05/T05008). arXiv: [1803.00844 \[physics.ins-det\]](https://arxiv.org/abs/1803.00844).
- 2013 [39] ATLAS Collaboration. “Performance of the ATLAS trigger system in 2015”. In:
2014 *Eur. Phys. J. C* 77 (2017), p. 317. DOI: [10.1140/epjc/s10052-017-4852-3](https://doi.org/10.1140/epjc/s10052-017-4852-3). arXiv: [1611.09661 \[hep-ex\]](https://arxiv.org/abs/1611.09661).
- 2016 [40] ATLAS Collaboration. *The ATLAS Collaboration Software and Firmware*. ATL-
2017 SOFT-PUB-2021-001. 2021. URL: <https://cds.cern.ch/record/2767187>.
- 2019 [41] ATLAS Collaboration. “Jet reconstruction and performance using particle flow
2020 with the ATLAS Detector”. In: *Eur. Phys. J. C* 77 (2017), p. 466. DOI: [10.1140/epjc/s10052-017-5031-2](https://doi.org/10.1140/epjc/s10052-017-5031-2). arXiv: [1703.10485 \[hep-ex\]](https://arxiv.org/abs/1703.10485).
- 2022 [42] Matteo Cacciari, Gavin P. Salam, and Gregory Soyez. “The anti- (k_t) jet clustering algorithm”.
2023 In: *JHEP* 04 (2008), p. 063. DOI: [10.1088/1126-6708/2008/04/063](https://doi.org/10.1088/1126-6708/2008/04/063).
2024 arXiv: [0802.1189 \[hep-ph\]](https://arxiv.org/abs/0802.1189).
- 2025 [43] ATLAS Collaboration. “Jet energy scale and resolution measured in proton–proton
2026 collisions at $\sqrt{s} = 13$ TeV with the ATLAS detector”. In: *Eur. Phys. J. C*
2027 81.8 (2021), p. 689. DOI: [10.1140/epjc/s10052-021-09402-3](https://doi.org/10.1140/epjc/s10052-021-09402-3). arXiv:
2028 [2007.02645 \[hep-ex\]](https://arxiv.org/abs/2007.02645).
- 2029 [44] ATLAS Collaboration. “Jet energy scale measurements and their systematic un-
2030 certainties in proton-proton collisions at $\sqrt{s} = 13$ TeV with the ATLAS detec-
2031 tor”. In: *Phys. Rev. D* 96 (Oct. 2017), p. 072002. DOI: [10.1103/PhysRevD.96.072002](https://doi.org/10.1103/PhysRevD.96.072002). arXiv: [1703.09665 \[hep-ex\]](https://arxiv.org/abs/1703.09665).
- 2033 [45] G. Altarelli and G. Parisi. “Asymptotic freedom in parton language”. In: *Nucl.
2034 Phys. B* 126.2 (1977), pp. 298–318. DOI: [https://doi.org/10.1016/0550-3213\(77\)90384-4](https://doi.org/10.1016/0550-3213(77)90384-4).
- 2036 [46] ATLAS Collaboration. “Light-quark and gluon jet discrimination in pp col-
2037 lisions at $\sqrt{s} = 7$ TeV with the ATLAS detector”. In: *Eur. Phys. J. C* 74 (2014),
2038 p. 3023. DOI: [10.1140/epjc/s10052-014-3023-z](https://doi.org/10.1140/epjc/s10052-014-3023-z). arXiv: [1405.6583 \[hep-ex\]](https://arxiv.org/abs/1405.6583).

REFERENCES

- 2040 [47] ATLAS Collaboration. *Quark versus Gluon Jet Tagging Using Charged-Particle*
2041 *Constituent Multiplicity with the ATLAS Detector*. ATL-PHYS-PUB-2017-009.
2042 Geneva, 2017. URL: <https://cds.cern.ch/record/2263679>.
- 2043 [48] ATLAS Collaboration. “Luminosity determination in pp collisions at $\sqrt{s} = 13$
2044 TeV using the ATLAS detector at the LHC”. In: (Dec. 2022). arXiv: [2212.09379 \[hep-ex\]](#).
- 2046 [49] ATLAS Collaboration. “ATLAS data quality operations and performance for 2015–
2047 2018 data-taking”. In: *JINST* 15.04 (2020), P04003. DOI: [10.1088/1748-0221/15/04/P04003](#). arXiv: [1911.04632 \[physics.ins-det\]](#).
- 2049 [50] Torbjörn Sjöstrand et al. “An introduction to PYTHIA 8.2”. In: *Comput. Phys.*
2050 *Commun.* 191 (2015), p. 159. DOI: [10.1016/j.cpc.2015.01.024](#). arXiv: [1410.3012 \[hep-ph\]](#).
- 2052 [51] NNPDF Collaboration, Richard D. Ball, et al. “Parton distributions with LHC
2053 data”. In: *Nucl. Phys. B* 867 (2013), p. 244. DOI: [10.1016/j.nuclphysb.2012.10.003](#). arXiv: [1207.1303 \[hep-ph\]](#).
- 2055 [52] ATLAS Collaboration. *ATLAS Pythia 8 tunes to (7 TeV) data*. ATL-PHYS-PUB-
2056 2014-021. 2014. URL: <https://cds.cern.ch/record/1966419>.
- 2057 [53] Enrico Bothmann et al. “Event generation with Sherpa 2.2”. In: *SciPost Phys.*
2058 7.3 (2019), p. 034. DOI: [10.21468/SciPostPhys.7.3.034](#). arXiv: [1905.09127 \[hep-ph\]](#).
- 2060 [54] Steffen Schumann and Frank Krauss. “A parton shower algorithm based on Catani–
2061 Seymour dipole factorisation”. In: *JHEP* 03 (2008), p. 038. DOI: [10.1088/1126-6708/2008/03/038](#). arXiv: [0709.1027 \[hep-ph\]](#).
- 2063 [55] Jan-Christopher Winter, Frank Krauss, and Gerhard Soff. “A modified cluster–
2064 hadronization model”. In: *Eur. Phys. J. C* 36 (2004), pp. 381–395. DOI: [10.1140/epjc/s2004-01960-8](#). arXiv: [hep-ph/0311085](#).
- 2066 [56] Sayipjamal Dulat et al. “New parton distribution functions from a global analysis
2067 of quantum chromodynamics”. In: *Phys. Rev. D* 93.3 (2016), p. 033006. DOI:
2068 [10.1103/PhysRevD.93.033006](#). arXiv: [1506.07443 \[hep-ph\]](#).

REFERENCES

- 2069 [57] Torbjorn Sjöstrand, Stephen Mrenna, and Peter Z. Skands. “PYTHIA 6.4 physics
2070 and manual”. In: *JHEP* 05 (2006), p. 026. DOI: [10.1088/1126-6708/2006/05/026](https://doi.org/10.1088/1126-6708/2006/05/026). arXiv: [hep-ph/0603175](https://arxiv.org/abs/hep-ph/0603175).
- 2072 [58] Johannes Bellm et al. “Herwig 7.0/Herwig++ 3.0 release note”. In: *Eur. Phys. J. C* 76.4 (2016), p. 196. DOI: [10.1140/epjc/s10052-016-4018-8](https://doi.org/10.1140/epjc/s10052-016-4018-8). arXiv: [1512.01178 \[hep-ph\]](https://arxiv.org/abs/1512.01178).
- 2075 [59] L. A. Harland-Lang et al. “Parton distributions in the LHC era: MMHT 2014
2076 PDFs”. In: *Eur. Phys. J. C* 75.5 (2015), p. 204. DOI: [10.1140/epjc/s10052-015-3397-6](https://doi.org/10.1140/epjc/s10052-015-3397-6). arXiv: [1412.3989 \[hep-ph\]](https://arxiv.org/abs/1412.3989).
- 2078 [60] Paolo Nason. “A new method for combining NLO QCD with shower Monte
2079 Carlo algorithms”. In: *JHEP* 11 (2004), p. 040. DOI: [10.1088/1126-6708/2004/11/040](https://doi.org/10.1088/1126-6708/2004/11/040). arXiv: [hep-ph/0409146](https://arxiv.org/abs/hep-ph/0409146).
- 2081 [61] Stefano Frixione, Paolo Nason, and Carlo Oleari. “Matching NLO QCD com-
2082 putations with parton shower simulations: the POWHEG method”. In: *JHEP*
2083 11 (2007), p. 070. DOI: [10.1088/1126-6708/2007/11/070](https://doi.org/10.1088/1126-6708/2007/11/070). arXiv: [0709.2092 \[hep-ph\]](https://arxiv.org/abs/0709.2092).
- 2085 [62] Simone Alioli et al. “A general framework for implementing NLO calculations
2086 in shower Monte Carlo programs: the POWHEG BOX”. In: *JHEP* 06 (2010),
2087 p. 043. DOI: [10.1007/JHEP06\(2010\)043](https://doi.org/10.1007/JHEP06(2010)043). arXiv: [1002.2581 \[hep-ph\]](https://arxiv.org/abs/1002.2581).
- 2088 [63] The NNPDF Collaboration, Richard D. Ball, et al. “Parton distributions for the
2089 LHC run II”. In: *JHEP* 04 (2015), p. 040. DOI: [10.1007/JHEP04\(2015\)040](https://doi.org/10.1007/JHEP04(2015)040). arXiv: [1410.8849 \[hep-ph\]](https://arxiv.org/abs/1410.8849).
- 2091 [64] ATLAS Collaboration. “Performance of the ATLAS track reconstruction algo-
2092 rithms in dense environments in LHC Run 2”. In: *Eur. Phys. J. C* 77.10 (2017),
2093 p. 673. DOI: [10.1140/epjc/s10052-017-5225-7](https://doi.org/10.1140/epjc/s10052-017-5225-7). arXiv: [1704.07983 \[hep-ex\]](https://arxiv.org/abs/1704.07983).
- 2095 [65] Matteo Cacciari and Gavin P. Salam. “Pileup subtraction using jet areas”. In:
2096 *Phys. Lett. B* 659.1 (2008), pp. 119–126. DOI: <https://doi.org/10.1016/j.physletb.2007.09.077>. arXiv: [0707.1378 \[hep-ph\]](https://arxiv.org/abs/0707.1378).

REFERENCES

- 2098 [66] CDF Collaboration. “Measurement of b -jet shapes in inclusive jet production in
2099 $p\bar{p}$ collisions at $\sqrt{s} = 1.96$ TeV”. In: *Phys. Rev. D* 78 (2008), p. 072005. DOI:
2100 [10.1103/PhysRevD.78.072005](https://doi.org/10.1103/PhysRevD.78.072005). arXiv: [0806.1699](https://arxiv.org/abs/0806.1699) [hep-ex].
- 2101 [67] ATLAS Collaboration. “Measurement of jet shapes in top-quark pair events at \sqrt{s}
2102 = 7 TeV using the ATLAS detector”. In: *Eur. Phys. J. C* 73.12 (2013), p. 2676.
2103 DOI: [10.1140/epjc/s10052-013-2676-3](https://doi.org/10.1140/epjc/s10052-013-2676-3). arXiv: [1307.5749](https://arxiv.org/abs/1307.5749)
2104 [hep-ex].
- 2105 [68] ATLAS Collaboration. “Measurement of the flavour composition of dijet events
2106 in pp collisions at $\sqrt{s} = 7$ TeV with the ATLAS detector”. In: *Eur. Phys. J. C*
2107 73.2 (2013), p. 2301. DOI: [10.1140/epjc/s10052-013-2301-5](https://doi.org/10.1140/epjc/s10052-013-2301-5). arXiv:
2108 [1210.0441](https://arxiv.org/abs/1210.0441) [hep-ex].
- 2109 [69] ATLAS Collaboration. “Measurement of jet charge in dijet events from $\sqrt{s}=8$
2110 TeV pp collisions with the ATLAS detector”. In: *Phys. Rev. D* 93.5 (2016),
2111 p. 052003. DOI: [10.1103/PhysRevD.93.052003](https://doi.org/10.1103/PhysRevD.93.052003). arXiv: [1509.05190](https://arxiv.org/abs/1509.05190)
2112 [hep-ex].
- 2113 [70] David Krohn et al. “Jet Charge at the LHC”. In: *Phys. Rev. Lett.* 110 (May 2013),
2114 p. 212001. DOI: [10.1103/PhysRevLett.110.212001](https://doi.org/10.1103/PhysRevLett.110.212001). arXiv: [1209.2421](https://arxiv.org/abs/1209.2421) [hep-ph].
- 2116 [71] Ian Moult, Lina Necib, and Jesse Thaler. “New angles on energy correlation func-
2117 tions”. In: *JHEP* 12 (2016), p. 153. DOI: [10.1007/JHEP12\(2016\)153](https://doi.org/10.1007/JHEP12(2016)153).
2118 arXiv: [1609.07483](https://arxiv.org/abs/1609.07483) [hep-ph].
- 2119 [72] Andrew J. Larkoski, Gavin P. Salam, and Jesse Thaler. “Energy correlation func-
2120 tions for jet substructure”. In: *JHEP* 06 (2013), p. 108. DOI: [10.1007/JHEP06\(2013\)108](https://doi.org/10.1007/JHEP06(2013)108). arXiv: [1305.0007](https://arxiv.org/abs/1305.0007) [hep-ph].
- 2122 [73] Guolin Ke et al. “LightGBM: A Highly Efficient Gradient Boosting Decision
2123 Tree”. In: *Advances in Neural Information Processing Systems 30 (NIPS 2017)*.
2124 Curran Associates, Inc. URL: https://proceedings.neurips.cc/paper_files/paper/2017/file/6449f44a102fde848669bdd9eb6b76fa-Paper.pdf.
- 2127 [74] Takuya Akiba et al. *Optuna: A Next-generation Hyperparameter Optimization
2128 Framework*. 2019. arXiv: [1907.10902](https://arxiv.org/abs/1907.10902) [cs.LG].

REFERENCES

- 2129 [75] A. Buckley et al. “LHAPDF6: parton density access in the LHC precision era”.
2130 In: *Eur. Phys. J. C* 75 (2015), p. 132. DOI: <https://doi.org/10.1140/epjc/s10052-015-3318-8>. arXiv: [1412.7420](https://arxiv.org/abs/1412.7420) [hep-ph].
- 2132 [76] S. Mrenna and P. Skands. “Automated parton-shower variations in PYTHIA 8”.
2133 In: *Phys. Rev. D* 94.7 (2016), p. 074005. DOI: [10.1103/PhysRevD.94.074005](https://doi.org/10.1103/PhysRevD.94.074005). arXiv: [1605.08352](https://arxiv.org/abs/1605.08352) [hep-ph].
- 2135 [77] DerivationProductionTeam. *Exotics derivation twiki page*. URL: <https://twiki.cern.ch/twiki/bin/view/AtlasProtected/DerivationframeworkEx>
- 2137 [78] Zach Marshall. *Re-re-defining the standard QCD di-jet samples: beginning to like event weights*. ATL-COM-PHYS-2015-417. 2015. URL: <https://cds.cern.ch/record/2016630>.
- 2140 [79] Luis A. Anchordoqui, Haim Goldberg, and Tomasz R. Taylor. “Decay widths of
2141 lowest massive Regge excitations of open strings”. In: *Phys. Lett. B* 668 (2008),
2142 pp. 373–377. DOI: [10.1016/j.physletb.2008.09.003](https://doi.org/10.1016/j.physletb.2008.09.003). arXiv: [0806.3420](https://arxiv.org/abs/0806.3420) [hep-ph].
- 2144 [80] Georges Aad et al. “ATLAS search for new phenomena in dijet mass and angular
2145 distributions using pp collisions at $\sqrt{s} = 7$ TeV”. In: *JHEP* 01 (2013), p. 029.
2146 DOI: [10.1007/JHEP01\(2013\)029](https://doi.org/10.1007/JHEP01(2013)029). arXiv: [1210.1718](https://arxiv.org/abs/1210.1718) [hep-ex].
- 2147 [81] Serguei Chatrchyan et al. “Search for Resonances in the Dijet Mass Spectrum
2148 from 7 TeV pp Collisions at CMS”. In: *Phys. Lett. B* 704 (2011), pp. 123–
2149 142. DOI: [10.1016/j.physletb.2011.09.015](https://doi.org/10.1016/j.physletb.2011.09.015). arXiv: [1107.4771](https://arxiv.org/abs/1107.4771)
2150 [hep-ex].
- 2151 [82] Serguei Chatrchyan et al. “Search for Narrow Resonances and Quantum Black
2152 Holes in Inclusive and b -Tagged Dijet Mass Spectra from pp Collisions at $\sqrt{s} = 7$
2153 TeV”. In: *JHEP* 01 (2013), p. 013. DOI: [10.1007/JHEP01\(2013\)013](https://doi.org/10.1007/JHEP01(2013)013).
2154 arXiv: [1210.2387](https://arxiv.org/abs/1210.2387) [hep-ex].
- 2155 [83] Vardan Khachatryan et al. “Search for resonances and quantum black holes using
2156 dijet mass spectra in proton-proton collisions at $\sqrt{s} = 8$ TeV”. In: *Phys. Rev.*
2157 D91.5 (2015), p. 052009. DOI: [10.1103/PhysRevD.91.052009](https://doi.org/10.1103/PhysRevD.91.052009). arXiv:
2158 [1501.04198](https://arxiv.org/abs/1501.04198) [hep-ex].

REFERENCES

- 2159 [84] Vardan Khachatryan et al. “Search for narrow resonances decaying to dijets in
2160 proton-proton collisions at $\sqrt{s} = 13$ TeV”. In: *Phys. Rev. Lett.* 116.7 (2016),
2161 p. 071801. DOI: [10.1103/PhysRevLett.116.071801](https://doi.org/10.1103/PhysRevLett.116.071801). arXiv: [1512.01224](https://arxiv.org/abs/1512.01224) [hep-ex].
2162
- 2163 [85] Albert M Sirunyan et al. “Search for narrow and broad dijet resonances in proton-
2164 proton collisions at $\sqrt{s} = 13$ TeV and constraints on dark matter mediators and
2165 other new particles”. In: *JHEP* 08 (2018), p. 130. DOI: [10.1007/JHEP08\(2018\)130](https://doi.org/10.1007/JHEP08(2018)130). arXiv: [1806.00843](https://arxiv.org/abs/1806.00843) [hep-ex].
2166
- 2167 [86] Pourya Vakilipourtakalou and Douglas M. Gingrich. “Monte Carlo event genera-
2168 tor for the production and decay of string resonances in proton-proton collisions”.
2169 In: (Nov. 2018). arXiv: [1811.07458](https://arxiv.org/abs/1811.07458) [hep-ph].
2170
- 2171 [87] J. Pumplin et al. “New Generation of Parton Distributions with Uncertainties
2172 from Global QCD Analysis”. In: *JHEP* 07 (2002), p. 012. DOI: [10.1088/1126-6708/2002/07/012](https://doi.org/10.1088/1126-6708/2002/07/012). arXiv: [hep-ph/0201195](https://arxiv.org/abs/hep-ph/0201195).
2173
- 2174 [88] D. J. Lange. “The EvtGen particle decay simulation package”. In: *Nucl. Instrum.*
2175 *Meth. A* 462 (2001), p. 152. DOI: [10.1016/S0168-9002\(01\)00089-4](https://doi.org/10.1016/S0168-9002(01)00089-4).
2176
- 2177 [89] ATLAS Collaboration. *The Pythia 8 A3 tune description of ATLAS minimum bias*
2178 *and inelastic measurements incorporating the Donnachie–Landshoff diffractive*
model. ATL-PHYS-PUB-2016-017. 2016. URL: <https://cds.cern.ch/record/2206965>.
- 2179 [90] P. Meade and L. Randall. “Black holes and quantum gravity at the LHC”. In:
2180 *JHEP05* 2008 (2008), p. 003. DOI: [10.1088/1126-6708/2008/05/003](https://doi.org/10.1088/1126-6708/2008/05/003).
2181 arXiv: [0708.3017](https://arxiv.org/abs/0708.3017) [hep-ph].
- 2182 [91] Luis A. Anchordoqui et al. “Inelastic black hole production and large extra di-
2183 mensions”. In: *Phys. Lett.* B594 (2004), pp. 363–367. DOI: [10.1016/j.physletb.2004.05.051](https://doi.org/10.1016/j.physletb.2004.05.051). arXiv: [hep-ph/0311365](https://arxiv.org/abs/hep-ph/0311365) [hep-ph].
2184
- 2185 [92] De-Chang Dai et al. “BlackMax: a black-hole event generator with rotation, re-
2186 coil, split branes, and brane tension”. In: *Phys. Rev.* D77 (2008), p. 076007. DOI:
2187 [10.1103/PhysRevD.77.076007](https://doi.org/10.1103/PhysRevD.77.076007). arXiv: [0711.3012](https://arxiv.org/abs/0711.3012) [hep-ph].
2188
- 2189 [93] Eugene Lukacs. “A characterization of the normal distribution”. In: *The Annals*
of *Mathematical Statistics* 13.1 (1942), pp. 91–93.

REFERENCES

- 2190 [94] Robert M. Harris and Konstantinos Kousouris. “Searches for dijet resonances
2191 at hadron colliders”. In: *Int. J. Mod. Phys.* A26 (2011), pp. 5005–5055. DOI:
2192 [10.1142/S0217751X11054905](https://doi.org/10.1142/S0217751X11054905). arXiv: [1110.5302](https://arxiv.org/abs/1110.5302) [hep-ex].
- 2193 [95] Matteo Cacciari, Gavin P. Salam, and Gregory Soyez. “FastJet User Manual”. In:
2194 *Eur. Phys. J.* C72 (2012), p. 1896. DOI: [10.1140/epjc/s10052-012-1896-2](https://doi.org/10.1140/epjc/s10052-012-1896-2). arXiv: [1111.6097](https://arxiv.org/abs/1111.6097) [hep-ph].
- 2196 [96] Nishu Nishu et al. *Search for New Phenomena in Dijet Events using the complete
2197 Run-2 dataset collected with the ATLAS Detector at $\sqrt{s} = 13$ TeV*. Tech. rep.
2198 ATL-COM-PHYS-2018-1538. Geneva: CERN, Nov. 2018. URL: <https://cds.cern.ch/record/2646455>.
- 2200 [97] Hongtao Yang. *XML Analytic Workspace Builder*. 2021. URL: <https://twiki.cern.ch/twiki/bin/viewauth/AtlasProtected/XmlAnaWSBuilder>
2201 (visited on 06/22/2021).
- 2203 [98] Wouter Verkerke and David Kirkby. *The RooFit toolkit for data modeling*. 2003.
2204 arXiv: [physics/0306116](https://arxiv.org/abs/physics/0306116) [physics.data-an].
- 2205 [99] Will Buttinger. *xRooFit*. 2023. URL: <https://gitlab.cern.ch/will/xroofit> (visited on 07/24/2023).
- 2207 [100] V. V. Gligorov et al. *Avoiding biases in binned fits*. 2021. arXiv: [2104.13879](https://arxiv.org/abs/2104.13879)
2208 [physics.data-an].
- 2209 [101] P. Bagnaia et al. “Measurement of Jet Production Properties at the CERN anti-p
2210 p Collider”. In: *Phys. Lett.* 144B (1984), pp. 283–290. DOI: [10.1016/0370-2693\(84\)91822-7](https://doi.org/10.1016/0370-2693(84)91822-7).
- 2212 [102] CDF Collaboration, T. Aaltonen et al. “Search for new particles decaying into
2213 dijets in proton-antiproton collisions at $\sqrt{s} = 1.96$ ”. In: *Phys. Rev. D* 79 (Aug.
2214 2009), p. 112002. DOI: [10.1103/PhysRevD.79.112002](https://doi.org/10.1103/PhysRevD.79.112002). arXiv: [0812.4036](https://arxiv.org/abs/0812.4036) [hep-ex].
- 2216 [103] ATLAS Collaboration. “Search for New Particles in Two-Jet Final States in (7 TeV) *Proton–
2217 Proton* Collisions with the ATLAS Detector at the LHC”. In: *Phys. Rev. Lett.* 105
2218 (2010), p. 161801. DOI: [10.1103/PhysRevLett.105.161801](https://doi.org/10.1103/PhysRevLett.105.161801). arXiv:
2219 [1008.2461](https://arxiv.org/abs/1008.2461) [hep-ex].

REFERENCES

- 2220 [104] CMS Collaboration. “Search for Dijet Resonances in (7 TeV) (pp) *Collisions at CMS*”.
2221 In: *Phys. Rev. Lett.* 105 (2010), p. 211801. DOI: [10.1103/PhysRevLett.105.211801](https://doi.org/10.1103/PhysRevLett.105.211801). arXiv: [1010.0203 \[hep-ex\]](https://arxiv.org/abs/1010.0203).
- 2223 [105] ATLAS Collaboration. “A search for new physics in dijet mass and angular distri-
2224 butions in (pp) *collisions at ($\sqrt{s} = 7$ TeV) measured with the ATLAS detector*”. In:
2225 *New J. Phys.* 13 (2011), p. 053044. DOI: [10.1088/1367-2630/13/5/053044](https://doi.org/10.1088/1367-2630/13/5/053044). arXiv: [1103.3864 \[hep-ex\]](https://arxiv.org/abs/1103.3864).
- 2227 [106] ATLAS Collaboration. “Search for new phenomena in the dijet mass distribution
2228 using (pp) *collision data at ($\sqrt{s} = 8$ TeV) with the ATLAS detector*”. In: *Phys. Rev.*
2229 *D* 91 (2015), p. 052007. DOI: [10.1103/PhysRevD.91.052007](https://doi.org/10.1103/PhysRevD.91.052007). arXiv:
2230 [1407.1376 \[hep-ex\]](https://arxiv.org/abs/1407.1376).
- 2231 [107] ATLAS Collaboration. “Search for new resonances in mass distributions of jet
2232 pairs using (139 fb^{-1}) of (pp) *collisions at ($\sqrt{s} = 13$ TeV) with the ATLAS detector*”.
2233 In: *JHEP* 03 (2020), p. 145. DOI: [10.1007/JHEP03\(2020\)145](https://doi.org/10.1007/JHEP03(2020)145). arXiv:
2234 [1910.08447 \[hep-ex\]](https://arxiv.org/abs/1910.08447).
- 2235 [108] J. Alitti et al. “A Measurement of two jet decays of the W and Z bosons at the
2236 CERN $\bar{p}p$ collider”. In: *Z. Phys. C* 49 (1991), pp. 17–28. DOI: [10.1007/BF01570793](https://doi.org/10.1007/BF01570793).
- 2238 [109] J. Alitti et al. “A Search for new intermediate vector mesons and excited quarks
2239 decaying to two jets at the CERN $\bar{p}p$ collider”. In: *Nucl. Phys. B* 400 (1993),
2240 pp. 3–24. DOI: [10.1016/0550-3213\(93\)90395-6](https://doi.org/10.1016/0550-3213(93)90395-6).
- 2241 [110] ATLAS Collaboration. *Recommendations for the Modeling of Smooth Backgrounds*.
2242 ATL-PHYS-PUB-2020-028. 2020. URL: <https://cds.cern.ch/record/2743717>.

2244

8 Acknowledgements

2245 First of all, I would like to extend my heartfelt gratitude to my parents for their unwa-
2246 vering love, encouragement, and unconditional support throughout my time in pursuing
2247 this PhD. Without them, I wouldn't have been able to come this far.

2248 I am also thankful to my supervisors, Prof. Shu Li from the Tsung-Dao Lee Insti-
2249 tute & Shanghai Jiao Tong University and Prof. Shih-Chieh Hsu from the University of
2250 Washington, Seattle, for their invaluable guidance, expertise, and mentorship. Their in-
2251 sightful feedback and patient guidance have been instrumental in shaping the direction of
2252 my research and future career. Moreover, this thesis would not have been possible with-
2253 out the collective contributions of my collaborators: Iain Bertram; Ke Li; Ben Nachman;
2254 Haoran Zhao; Nishu Nishu; Rongqian Qian; Jack Lindon; Jyoti Prakash Biswal; Davide
2255 Melini; Lorenzo Rossini; Reina Coromoto Camacho Toro; Matt LeBlanc.

2256 Thanks to individuals who have ever helped me and expressed their belief in me,
2257 and to those who inspired me - M. B. B. C; M. S; V. S; K. C; V. C; M. C, etc.